

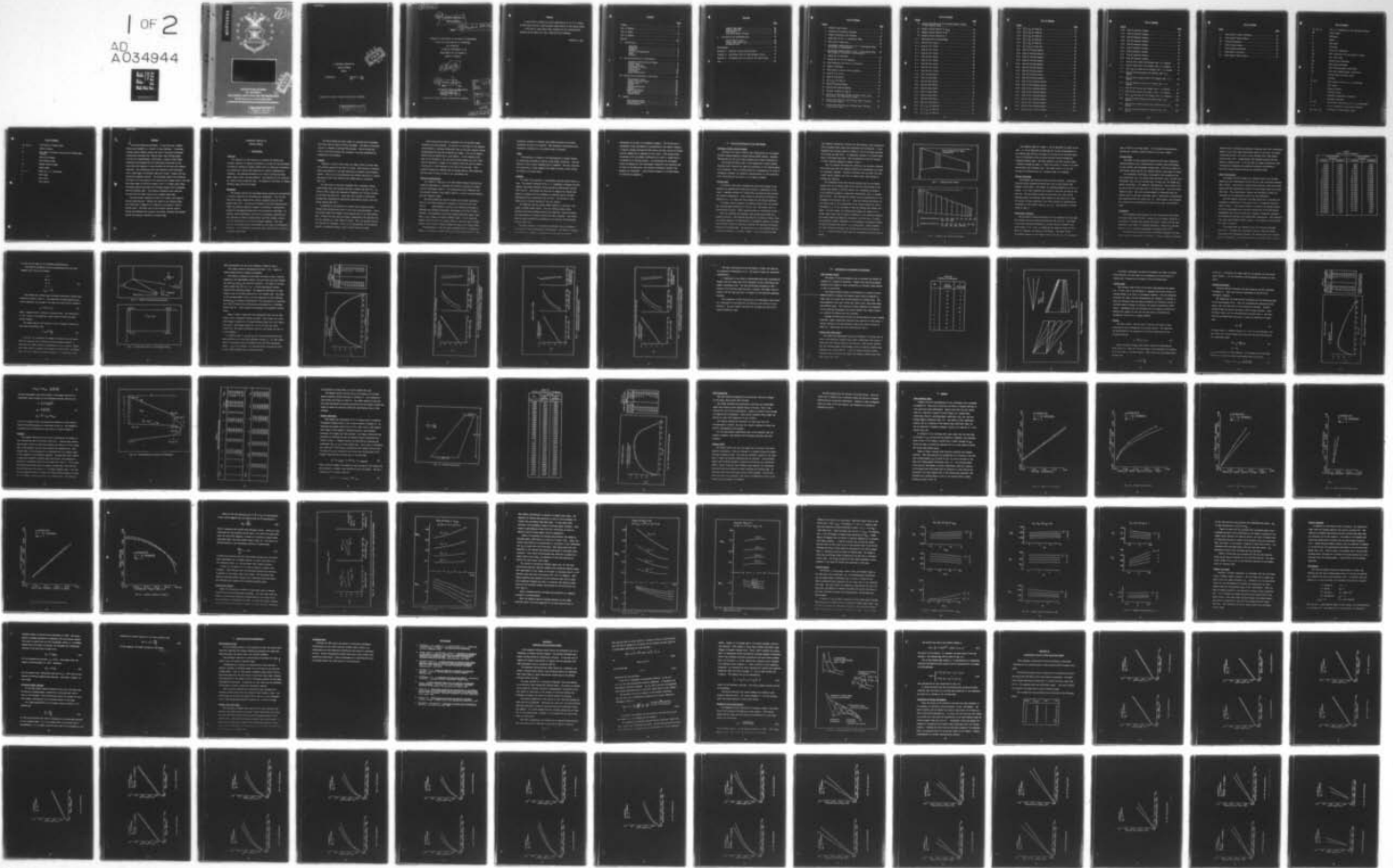
AD-A034 944

AIR FORCE INST OF TECH WRIGHT-PATTERSON AFB OHIO SCH--ETC F/6 1/3  
A PARAMETRIC ANALYSIS OF WINGLET EFFECTS.(U)  
DEC 76 M D CARY  
6A/MC/76D-5

UNCLASSIFIED

NL

1 OF 2  
AD  
A034944



ADA034944

*CR*



*DDC*  
*PERM*  
JAN 20 1977  
*RESERVE*

UNITED STATES AIR FORCE  
AIR UNIVERSITY  
AIR FORCE INSTITUTE OF TECHNOLOGY  
Wright-Patterson Air Force Base, Ohio

**DISTRIBUTION STATEMENT A**

Approved for public release;  
Distribution Unlimited

D D C  
RECEIVED  
JAN 28 1977

A PARAMETRIC ANALYSIS OF  
WINGLET EFFECTS  
THESIS

GA/MC/76D-5

Mitchell D. Cary  
Capt USAF

Approved for public release; distribution unlimited.

DISTRIBUTION STATEMENT A  
Approved for public release;  
Distribution Unlimited

6 A PARAMETRIC ANALYSIS OF WINGLET EFFECTS

9 Master's thesis  
THESIS

Presented to the Faculty of the School of Engineering  
of the Air Force Institute of Technology  
Air University  
in Partial Fulfillment of the  
Requirements for the Degree of  
Master of Science

12 119p.

by

10 Mitchell D. Cary B.S.  
Capt USAF

Graduate Astronautical Engineering

11 December 1976

Approved for public release; distribution unlimited.

ACCESSION for	
NTIS	White Section <input checked="" type="checkbox"/>
DSC	Full Section <input type="checkbox"/>
UNANNOUNCED JUSTIFICATION	<input type="checkbox"/>
BY	
DISTRIBUTION/AVAILABILITY CODES	
Dist.	APPL. DIV. OR SPECIAL
A	

1473  
012225  
4

Preface

I would like to express my sincere appreciation to Dr. D. W. Breuer, my AFIT thesis advisor, whose guidance aided greatly in this thesis study.

I also wish to thank Major Roger Crawford for his assistance and guidance and my family for their cooperation and tolerance.

Mitchell D. Cary

Contents

	<u>Page</u>
Preface . . . . .	ii
List of Figures . . . . .	v
List of Tables . . . . .	ix
List of Symbols . . . . .	x
Abstract . . . . .	xii
I. Introduction . . . . .	1
Objective . . . . .	1
Background . . . . .	1
Winglets . . . . .	2
Previous Investigations . . . . .	3
Scope . . . . .	4
Approach . . . . .	4
II. Use and Verification of NPLS Method . . . . .	6
Nonplanar Lifting Systems Program . . . . .	6
Program Input . . . . .	6
Winglet Definition . . . . .	9
Wing-Winglet Junction . . . . .	9
Program Output . . . . .	10
Convergence . . . . .	10
Method Verification . . . . .	11
III. Calculation of Aerodynamic Coefficients . . . . .	20
Wing Parameter Study . . . . .	20
Winglet Cant Angle Study . . . . .	20
Program Input . . . . .	23
Airfoil . . . . .	23
Planform Definition . . . . .	24
Winglets . . . . .	26
Winglet Definition . . . . .	29
NPLS Program Use . . . . .	33
Program Output . . . . .	33
IV. Results . . . . .	35
Wing Parameter Study . . . . .	35
Longitudinal Effects . . . . .	42
Lateral Effects . . . . .	48

Contents

	<u>Page</u>
Winglet Cant Angle . . . . .	52
Winglet Penalties . . . . .	53
Trim Effects . . . . .	53
Structural Weight Increase . . . . .	54
V. Conclusions and Recommendations . . . . .	56
Wing Parameter Study . . . . .	56
Winglet Cant Angle Study . . . . .	56
Recommendations . . . . .	57
Bibliography . . . . .	58
Appendix A: Nonplanar Lifting Systems Theory . . . . .	59
Appendix B: Aerodynamic Data for Wing Parameter Study . . . . .	64
Appendix C: Aerodynamic Data for Winglet Cant Angle Study . . . . .	95
Vita . . . . .	102

List of Figures

<u>Figure</u>		<u>Page</u>
1	Planform Input Points . . . . .	8
2	Spanwise and Chordwise Divisions . . . . .	8
3	Winglet Translation and Rotation . . . . .	14
4	Right Half of AR = 4, Rectangular Wing . . . . .	14
5	NACA 64 <sub>1</sub> A412 Camberline . . . . .	16
6	Aerodynamic Characteristics of AR = 4 Rectangular Wing (Calculated vs Experimental) . . . . .	17
7	Aerodynamic Characteristics of AR = 4 Rectangular Wing With Endplate (Calculated vs Experimental) . . . . .	18
8	Comparison of Planforms . . . . .	22
9	Boeing BAC 311 Airfoil Meanline . . . . .	25
10	Wing Parameters and Points of Definition . . . . .	27
11	Winglet Parameters . . . . .	30
12	NASA General Aviation Airfoil Meanline . . . . .	32
13	Wing #1 Lift Curves . . . . .	36
14	Wing #1 Drag Polars . . . . .	37
15	$C_L^2$ vs $C_{Di}$ for Wing #1 . . . . .	38
16	Wing #1 Pitching Moments . . . . .	39
17	Wing #1 Root Bending Moments . . . . .	40
18	Spanwise Loading for Wing #1 . . . . .	41
19	Increase in Efficiency Factor vs Aspect Ratio, Wing Sweep Angle, and Wing Dihedral Angle . . . . .	43
20	Induced Drag Reduction and Pitching Moment Increase vs Wing Sweep Angle . . . . .	44
21	Induced Drag Reduction and Pitching Moment Increase vs Wing Aspect Ratio . . . . .	46

List of Figures

<u>Figure</u>		<u>Page</u>
22	Induced Drag Reduction and Pitching Moment Increase vs Wing Dihedral Angle . . . . .	47
23	Winglet Lateral Effects vs $\Lambda_{1/4c}$ . . . . .	49
24	Winglet Lateral Effects vs AR . . . . .	50
25	Winglet Lateral Effects vs $\Gamma$ . . . . .	51
A- 1	Representation of Wing Loading . . . . .	62
B- 1	Wing #2 Lift Curves . . . . .	65
B- 2	Wing #3 Lift Curves . . . . .	65
B- 3	Wing #4 Lift Curves . . . . .	66
B- 4	Wing #5 Lift Curves . . . . .	66
B- 5	Wing #6 Lift Curves . . . . .	67
B- 6	Wing #7 Lift Curves . . . . .	67
B- 7	Wing #8 Lift Curves . . . . .	68
B- 8	Wing #9 Lift Curves . . . . .	69
B- 9	Wing #10 Lift Curves . . . . .	69
B-10	Wing #2 Drag Polars . . . . .	70
B-11	Wing #3 Drag Polars . . . . .	70
B-12	Wing #4 Drag Polars . . . . .	71
B-13	Wing #5 Drag Polars . . . . .	71
B-14	Wing #6 Drag Polars . . . . .	72
B-15	Wing #7 Drag Polars . . . . .	72
B-16	Wing #8 Drag Polars . . . . .	73
B-17	Wing #9 Drag Polars . . . . .	74
B-18	Wing #10 Drag Polars . . . . .	74
B-19	$C_L^2$ vs $C_{Di}$ for Wing #2 . . . . .	75
B-20	$C_L^2$ vs $C_{Di}$ for Wing #3 . . . . .	75
B-21	$C_L^2$ vs $C_{Di}$ for Wing #4 . . . . .	76

List of Figures

<u>Figure</u>		<u>Page</u>
B-22	$C_L^2$ vs $C_{Di}$ for Wing #5 . . . . .	76
B-23	$C_L^2$ vs $C_{Di}$ for Wing #6 . . . . .	77
B-24	$C_L^2$ vs $C_{Di}$ for Wing #7 . . . . .	77
B-25	$C_L^2$ vs $C_{Di}$ for Wing #8 . . . . .	78
B-26	$C_L^2$ vs $C_{Di}$ for Wing #9 . . . . .	79
B-27	$C_L^2$ vs $C_{Di}$ for Wing #10 . . . . .	79
B-28	Wing #2 Pitching Moments . . . . .	80
B-29	Wing #3 Pitching Moments . . . . .	80
B-30	Wing #4 Pitching Moments . . . . .	81
B-31	Wing #5 Pitching Moments . . . . .	81
B-32	Wing #6 Pitching Moments . . . . .	82
B-33	Wing #7 Pitching Moments . . . . .	82
B-34	Wing #8 Pitching Moments . . . . .	83
B-35	Wing #9 Pitching Moments . . . . .	84
B-36	Wing #10 Pitching Moments . . . . .	84
B-37	Wing #2 Root Bending Moments . . . . .	85
B-38	Wing #3 Root Bending Moments . . . . .	85
B-39	Wing #4 Root Bending Moments . . . . .	86
B-40	Wing #5 Root Bending Moments . . . . .	86
B-41	Wing #6 Root Bending Moments . . . . .	87
B-42	Wing #7 Root Bending Moments . . . . .	87
B-43	Wing #8 Root Bending Moments . . . . .	88
B-44	Wing #9 Root Bending Moments . . . . .	89
B-45	Wing #10 Root Bending Moments . . . . .	89

List of Figures

<u>Figure</u>		<u>Page</u>
B-46	Wing #2 Spanwise Loading . . . . .	90
B-47	Wing #3 Spanwise Loading . . . . .	90
B-48	Wing #4 Spanwise Loading . . . . .	91
B-49	Wing #5 Spanwise Loading . . . . .	91
B-50	Wing #6 Spanwise Loading . . . . .	92
B-51	Wing #7 Spanwise Loading . . . . .	92
B-52	Wing #8 Spanwise Loading . . . . .	93
B-53	Wing #9 Spanwise Loading . . . . .	94
B-54	Wing #10 Spanwise Loading . . . . .	94
C- 1	Wing #1 Lift Curves with Winglet Cant = $\pm 3$ Degrees . .	96
C- 2	Wing #1 Drag Polars with Winglet Cant = $\pm 3$ Degrees . .	96
C- 3	$C_L^2$ vs $C_{Di}$ for Wing #1 with Winglet Cant = $\pm 3$ Degrees .	97
C- 4	Wing #1 Pitching Moments with Winglet Cant = $\pm 3$ Degrees . . . . .	97
C- 5	Wing #1 Root Bending Moments with Winglet Cant = $\pm 3$ Degrees . . . . .	98
C- 6	Wing #1 Spanwise Loading with Winglet Cant = $\pm 3$ Degrees . . . . .	98
C- 7	Wing #3 Lift Curves with Winglet Cant = $\pm 3$ Degrees . .	99
C- 8	Wing #3 Drag Polars with Winglet Cant = $\pm 3$ Degrees . .	99
C- 9	$C_L^2$ vs $C_{Di}$ for Wing #3 with Winglet Cant = $\pm 3$ Degrees .	100
C-10	Wing #3 Pitching Moments with Winglet Cant = $\pm 3$ Degrees . . . . .	100
C-11	Wing #3 Root Bending Moments with Winglet Cant = $\pm 3$ Degrees . . . . .	101
C-12	Wing #3 Spanwise Loading with Winglet Cant = $\pm 3$ Degrees . . . . .	101

List of Tables

<u>Table</u>		<u>Page</u>
I	NACA 64 <sub>1</sub> A412 Airfoil Ordinates . . . . .	12
II	NACA 64 <sub>1</sub> A412 Camber Angles . . . . .	16
III	Planform Parameters . . . . .	21
IV	BAC311 Camber Angles . . . . .	25
V	Wing Planform Parameters . . . . .	28
VI	NASA Winglet Ordinates . . . . .	31
VII	NASA Winglet Camber Angles . . . . .	32

### List of Symbols

$A_u, A_v, A_w$	(x, y, z) components of the influence function
AR	Aspect Ratio
b	Wing Span
c	Chord
$c_r$	Root Chord
$c_t$	Tip Chord
$C_L$	Total lift coefficient
$C_{L0}$	Lift coefficient for zero angle of attack
$C_L$	Lift curve slope
$C_{Di}$	Induced drag coefficient
$C_D$	Total drag coefficient
$C_M$	Total pitching moment coefficient
$C_R$	Total root bending moment coefficient
e	Induced drag efficiency factor
h	Altitude
$\bar{i}, \bar{j}, \bar{k}$	Unit vectors in the (x, y, z) directions
M	Mach number
q	Dynamic pressure
$\bar{q}$	Velocity vector
s	Streamwise tangential coordinate
S	Reference wing area
$\bar{u}, \bar{v}, \bar{w}$	Perturbation velocities in (x, y, z) directions
U, W	x and z components of freestream velocity
$x_{mc}, y_{mc}, z_{mc}$	Coordinates of wing moment center

List of Symbols

$x_0, y_0, z_0$	Coordinates of winglet apex
$\alpha$	Angle of attack
$\alpha_c$	Cant angle of winglet (positive with leading edge inboard)
$\gamma$	Vorticity strength
$\Gamma$	Wing dihedral angle
$\Gamma_w$	Winglet dihedral angle
$\epsilon$	Camber angle
$\zeta, \eta, \xi$	Dummy (x, y, z) coordinates
$\Lambda$	Sweep angle
$\lambda$	Taper ratio
$\rho$	Fluid density

Abstract

A two part study was undertaken. In the first part, winglet effects were examined on a variety of wing planforms. A nonplanar lifting surface computer program was used to calculate aerodynamic coefficients including lift, induced drag, wing pitching moment, and wing root bending moment coefficients. Typical cruise flight conditions were examined and the coefficients calculated for the wing alone were compared to those obtained for the wing with winglets installed. The calculations were then repeated as the wing aspect ratio, sweep angle, and dihedral angle were varied. Winglet size and orientation remained constant. The percentage induced drag reduction was found to be the greatest on the wing with the highest aspect ratio and wing sweep angle (27.5% for an aspect ratio 7, 45 degree swept wing). Percentage induced drag reduction increased slightly with increasing positive dihedral angle. The greatest incremental drag reduction occurred with the lowest aspect ratio, highest swept wing.

The second study examined the effects of winglet cant angle on induced drag reduction. Winglet cant angle on two separate wings was varied from -3 degrees to +3 degrees in an attempt to find an optimum value. The model used in this analysis ignored viscous effects and indicated that positive cant angles (leading edge inboard) yielded the greatest reductions in induced drag.

A PARAMETRIC ANALYSIS OF  
WINGLET EFFECTS

I. Introduction

Objective

The objective of this thesis is to evaluate the effects and potential benefits of winglets installed on a variety of wing planforms. A parametric analysis of winglet effects will be conducted to determine the possible net induced drag reduction for several representative planforms. The planform parameters to be varied include wing sweep angle, aspect ratio, and wing dihedral. The analysis will be conducted for typical cruise conditions only. An analysis of the effect of winglet incidence angle will also be made.

Background

The present concern over decreasing energy supplies has necessitated a critical evaluation of increasing fuel consumption. Over the past twenty-five years, United States energy consumption has more than doubled (Ref 1:19). The National Aeronautics and Space Administration (NASA) was recently tasked by Congress to establish a comprehensive program for developing aeronautical fuel-conservation technology. In response, NASA established a task force of government scientists and NASA engineers to obtain recommendations from NASA research centers, aircraft manufacturers, and other government agencies. This task force has considered numerous improvements in all areas of aeronautical technology. One aerodynamic improvement under investigation is the use of winglets (Ref 1:20).

The United States Air Force (USAF) is concerned with increasing fuel costs and the threat of future increases. The USAF is evaluating the use of winglets on current USAF aircraft. The KC-135 and the C-141, which are two heavy fuel consumers, are prime candidates for modification with winglets.

### Winglets

Winglets, as used in this study, are small, nearly vertical wing-like surfaces mounted at the tips of a wing. These devices are mounted nearly perpendicular to the main wing and are normally canted slightly outward. They act as vortex diffusers and provide reductions in induced drag greater than those achieved with simple wing tip extensions (Ref 2:1).

For many years it has been recognized that a nonplanar lifting system should have less induced drag than a planar wing (Ref 3:1). As early as 1897 a patent was obtained by Lanchester for vertical surfaces at the wing tips (Ref 3:1). Since that time a number of theoretical analyses have indicated the significant improvements possible with nonplanar systems (Ref 3:2).

In addition to the reduction in induced drag, winglets produce several other effects which relate to the total drag improvement. First, the profile drag of the winglet itself negates some of the drag improvement. Second, for most wing and winglet combinations, the required lift will be produced at a lower angle of attack. Thus, the parasite drag of the wing will be decreased. Third, at the intersection of the wing and winglet, interference effects cause a slight increase in drag.

Other effects which must be considered are the possible weight increases and trim penalties. In addition to the weight of the winglets and attachments, increased aerodynamic loads on the main wing may require strengthening the wing and increasing its weight. Part of the winglet benefits may be negated due to trim effects. As the loading at the wing tip is increased, a net nose down pitching moment may occur. This must be balanced by a moment in the opposite direction and may require a down-load, or lift reduction on the tail of the aircraft. Thus, potential benefits of winglets must be weighed against their penalties, and care must be taken to look at net improvement only.

#### Previous Investigations

Dr. Richard R. Whitcomb of the NASA Langley Research Facility has conducted experiments to determine the effects of winglets on overall aircraft performance (Ref 3). His studies have dealt primarily with the potential benefits from winglet addition to first and second generation jet transport wings.

The Boeing Commercial Aircraft Company has recently completed a study of the effects produced by winglets on the KC-135 and C-141 (Ref 4). A winglet parameter study was also conducted by Boeing to determine the potential aerodynamic improvement of the KC-135 (Ref 4: 108-169). The parameters varied were leading edge sweep angle, taper ratio, area, length, and winglet dihedral angle. In all cases the winglets were located on the upper surface of the main wing. An aerodynamic vortex lattice computer program was used in the Boeing study.

Investigations to date have dealt primarily with the addition of winglets to transport aircraft such as the C-141 and the KC-135. The

parametric analysis of winglets with planform parameters described previously has yet to be reported. This parametric investigation was, therefore, considered to be a fruitful area of research.

### Scope

This analysis is limited to the investigation of winglet effects on trapezoidal planforms at typical cruise flight conditions. Only the effects of upper surface winglets will be examined. The size, location, and orientation of these winglets will remain constant, except during the winglet cant angle study.

### Approach

To conduct this analysis, a new nonplanar lifting surface theory is used. This method, developed by Mr. M. I. Goldhammer of Douglas Aircraft Company, represents nonplanar lifting systems by distributed vorticity (Ref 5 and 6). This method has been used to compute the induced drag benefit of winglets and the agreement of computed results with NASA experimental data is excellent (Ref 5:51-61). The validity of this method will be further examined in the next chapter.

The Nonplanar Lifting Systems (NPLS) method is a nonlinear, non-planar, lifting surface theory. The term lifting surface theory indicates that wing thickness effects are neglected. Wing-like bodies are represented by a cambered surface with zero thickness. This theory makes no small perturbation assumptions as do previous lifting surface theories (Ref 5:5).

The basic problem is to determine aerodynamic forces and moments on an arbitrary three dimensional lifting system. The system is assumed to be placed in a uniform, inviscid, and irrotational flow and is

represented by an array of rectangular elements. The calculation of aerodynamic forces and moments is accomplished by the digital computer. A computer program utilizing the NPLS theory has been written by Douglas Aircraft Company and is employed in this thesis. This program gives aerodynamic force and moment coefficients for either a single wing or a combination of lifting surfaces. By calculating the aerodynamic forces and moments for the wing-winglet combination and comparing them to those of the wing alone, the inviscid incremental effects of the winglets are determined. A more detailed summary of the NPLS method is contained in Appendix A.

## II. Use and Verification of the NPLS Method

### Nonplanar Lifting Systems Program

The basic tool used to conduct this investigation was the Douglas Aircraft Company Nonplanar Lifting Systems (NPLS) Program. Detailed instructions for the use of this program may be found in Reference 5.

The analytical method used in this program was a finite element technique which required the numerical definition of the lifting system to be evaluated. Since a lifting system was represented by an array of rectangular elements, the geometric characteristics of this array were first calculated and then input to the computer program.

### Program Input

To analyze a particular configuration using this program it was necessary to geometrically define each surface or combination of surfaces. Component surfaces of a system were separated and each surface was treated independently. Each surface was initially orientated in a defining (x, y, z) system and then rotated into the desired position.

To define a given planform, the program required that the leading and trailing edge coordinates at the tip, root, and either side of a discontinuity be given. These required points are illustrated in Fig. 1.

Once the planforms were defined, each surface was divided into spanwise sections. This division was based on two factors. First, since the planform geometry was represented by rectangular elements, the spanwise divisions needed to adequately represent the resulting "stairstep" leading and trailing edges. The second factor to be considered was the anticipated gradients in spanwise loading. Since this method assumed

that spanwise loading was constant over each section, close spacing was used in regions where large load variations were anticipated. It was suggested that section widths be limited to 2-5% of the wing semi-span at the wing tip (Ref 5:67). To adequately represent a 45 degree swept wing, 14 divisions were used. This representation with the location of these spanwise divisions is shown in Fig. 2.

Once the spanwise divisions were selected, the chordwise divisions were chosen such that the complete planform was represented by an array of rectangular elements. Chordwise divisions were also made such that closely spaced elements were used in regions where rapid changes in loading were expected.

The Elementary Vortex Distribution approach used in this method assumes that the functional form of the vorticity distribution on the leading edge element is  $F(1/\sqrt{s})$ , where  $s$  is a streamwise coordinate. On the remaining elements a trapezoidal distribution,  $F(s)$ , is assumed (Ref 5:18-23). This distribution results from the superposition of two triangular distributions (Fig. A-1). Since the loading distribution on the leading edge is well represented by the inverse square root vortex distribution, it is not necessary to make the leading edge element very small. For this reason, the leading edge element was allowed to be rather large (5 per cent of chord) in relation to the remaining elements. The second element was chosen to be smaller (2-1/2 per cent of chord), which allowed a smooth transition to the triangular distribution. Twelve chordwise divisions were used in this investigation. These divisions and their chordwise locations, are illustrated on the root section in Fig. 2. A representation of this type was recommended by Douglas (Ref 5: 64-68).

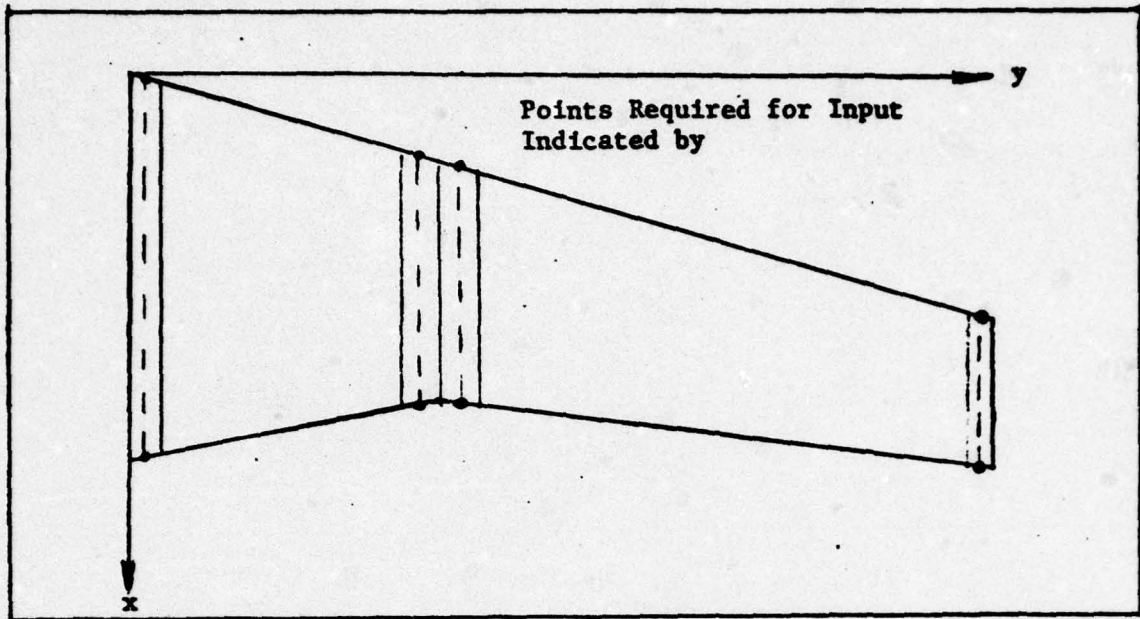


Fig. 1. Planform Input Points

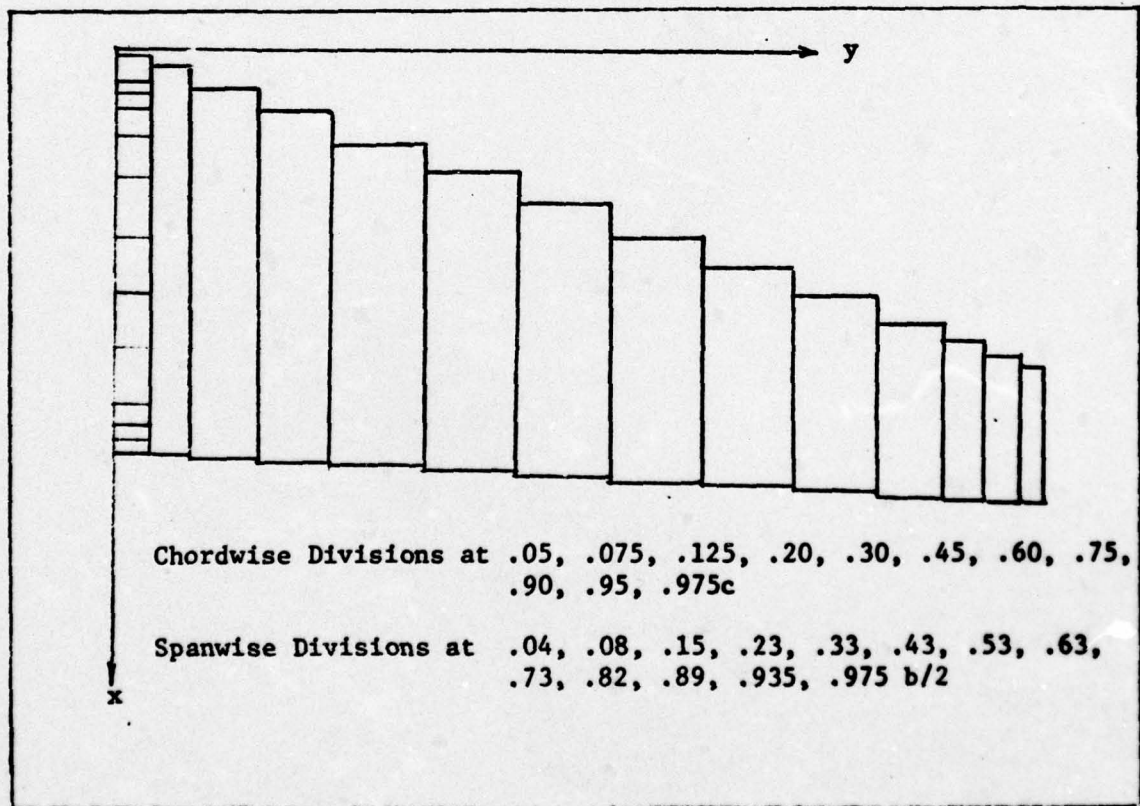


Fig. 2. Spanwise and Chordwise Divisions

The dihedral angle of a wing,  $\Gamma$ , can be specified in either of two ways. It can be specified by inputting the vertical displacements of the leading edge from the x-y plane or the wing can be initially specified to be entirely in the x-y plane and then rotated through the required dihedral angle. The first method is the most accurate since a rotation through an angle,  $\Gamma$ , reduces the span by a factor of  $(1-\cos\Gamma)$  and decreases the reference area. This would cause a 1.5 per cent decrease in reference area for a dihedral angle of 10 degrees.

#### Winglet Definition

The winglets were defined using the above procedure. Seven spanwise and twelve chordwise divisions were used to fully define each winglet in this study. The winglet is initially defined in an  $(x, y, z)$  system. It is then translated and rotated to join with the wing at the wing tip. The cant angle rotation is done about the y axis of the defining system; the dihedral angle rotation is done about the x axis. The surface is then translated to its final position by specifying the coordinates of the winglet apex  $(x_0, y_0, z_0)$ . This procedure is illustrated in Fig. 3.

#### Wing-Winglet Junction

The junction of wing and winglet had to be completed such that gaps were avoided and any overhang was minimized (Ref 5:69-72). The widths of the wing rectangular elements at the wing tip were selected to be large enough, (4 per cent) to accommodate the expected ranges of incidence,  $\pm 5$  degrees, and camber of the winglet. The width of the rectangular elements at the winglet root was 15 per cent of the winglet

span to allow for the wing camber. This prevented intersecting or passing near boundary condition points on the other surface.

#### Program Output

The output of this program includes the basic input parameters, detailed geometric data, distributions of pressure jump coefficients on each element, and aerodynamic loading data. This data is given for each system surface and for the complete system at each angle of attack.

The aerodynamic coefficients calculated by this program are the lift coefficient ( $C_L$ ), the induced drag coefficient ( $C_D$ ), the side force coefficient ( $C_Y$ ), and the pitching ( $C_M$ ), rolling ( $C_R$ ), and yawing ( $C_N$ ) moment coefficients. For symmetric configurations, total values of  $C_Y$ ,  $C_N$ , and  $C_R$  are for the right half of the system only. The actual total values are zero. The total pitching moment is referenced about the quarter chord of the mean aerodynamic chord. Yawing and rolling moments are referenced about the origin (Fig. 3). These surface total aerodynamic coefficients are normalized by surface area, span, and reference chord.

#### Convergence

The convergence characteristics of this solution have been shown to be quite good (Ref 5:32-36). Values of  $C_L$  are equally sensitive to the number of chordwise and spanwise divisions. Values of  $C_D$  are most sensitive to the number of chordwise divisions. Values of  $C_M$  are most sensitive to the chordwise arrangement of elements (Ref 5:33).

This program will accept as many as 500 finite elements; 252 were used to define a wing-winglet combination. Studies completed by Douglas

indicate that 10 spanwise and chordwise divisions yield lift coefficients within 1.5 per cent, drag coefficients within 4.0 per cent, and moment coefficients within 5 per cent of those obtained with a 400 element solution (Ref 5:34). Computational time increases greatly with the number of elements used. It is felt that the number selected for this investigation represents each planform accurately and achieves a desirable balance between accuracy and computation time.

#### Method Verification

The Douglas Aircraft Company has compared results from the NPLS method both with experimental results and with other theoretical methods. (Ref 5:32-62). Calculation of induced drag reduction, using this method agrees with NASA experimental results for the KC-135A within 11 per cent (Ref 5:59). Flow interference, viscous, and aeroelastic effects not considered in this method may account for this difference.

One test Douglas conducted of the NPLS method was to calculate the aerodynamic coefficients of the aspect ratio 4, rectangular wing discussed in Ref 7. The author attempted to duplicate the Douglas results to verify understanding and successful application of the NPLS method. Experimental data for this wing with a variety of endplates (winglets) was available as was data from Douglas NPLS computations. This configuration used a NACA 64<sub>1</sub>A412 airfoil section. The ordinates of this section are listed in Table I.

The program input was completed using the technique described previously. Although fewer rectangular elements could have easily represented this rectangular planform, 168 elements were used (14 spanwise X 12 chordwise). This representation was selected since it was to

Table I  
NACA 64<sub>1</sub>A412 Ordinates

Upper Surface % Chord		Lower Surface % Chord	
Station	Ordinate	Station	Ordinate
.32500	1.0500	.6800	.8375
.55000	1.3000	.9500	.9875
1.02500	1.6875	1.4750	1.2000
2.22500	2.4250	2.7625	1.5750
4.70000	3.4875	5.3000	2.0500
7.18500	4.3250	7.8125	2.3750
9.87500	5.0125	10.1250	2.6375
14.70000	6.1250	15.3000	3.0125
19.72500	6.9875	20.2750	3.6250
24.85125	7.6375	25.2375	3.4250
29.80000	8.1000	30.2000	3.5125
34.85000	8.4125	35.1500	3.5125
39.90000	8.5500	40.1000	3.4375
44.93750	8.4875	45.0625	3.2375
49.98750	8.2625	50.0125	2.9500
54.97500	7.9000	55.0250	2.5875
59.93750	7.4000	60.0625	2.2000
64.90000	6.8000	65.1000	1.7750
69.87500	6.0875	70.1250	1.3500
74.85000	5.2750	75.1500	.9500
79.82500	4.3625	80.1750	.6250
84.82500	3.3125	85.1750	.4250
89.87500	2.2375	90.1250	.2750
94.93750	1.1250	95.0625	.1500
100.00000	.0250		-.0250

be used for the wings in the remaining representations.

The planform parameters were non-dimensionalized by the wing semispan (b/2) and are as follows

$$\begin{aligned} b &= 2 \\ AR &= 4 \\ S &= 1 \\ \bar{c} &= .5 \\ x_{mc} &= .125 \end{aligned} \tag{1}$$

The leading and trailing edge coordinates necessary to define this planform are shown in Fig. 4. The camberline was approximated by the airfoil meanline, the average of the upper and lower airfoil ordinates

$$\eta_c = \frac{1}{2} (\eta_l + \eta_u) \tag{2}$$

where  $\eta$  represents the y ordinate in percent chord. The subscripts c, l, and u refer to the camberline, upper airfoil surface and lower airfoil surface.

The camber angle at the midpoint of each rectangular element was calculated analytically from

$$\epsilon = \tan^{-1} \frac{\Delta \eta_c}{\Delta x} \tag{3}$$

In Eq (3),  $\Delta \eta_c$  represents the change in camberline and  $\Delta x$  represents the change in the x ordinate of the rectangular element.  $\epsilon$  represents the camber angle at the midpoint of the rectangular element. This camber angle is positive in the angle of attack sense. Calculated values for this airfoil are listed in Table II. A comparison of the

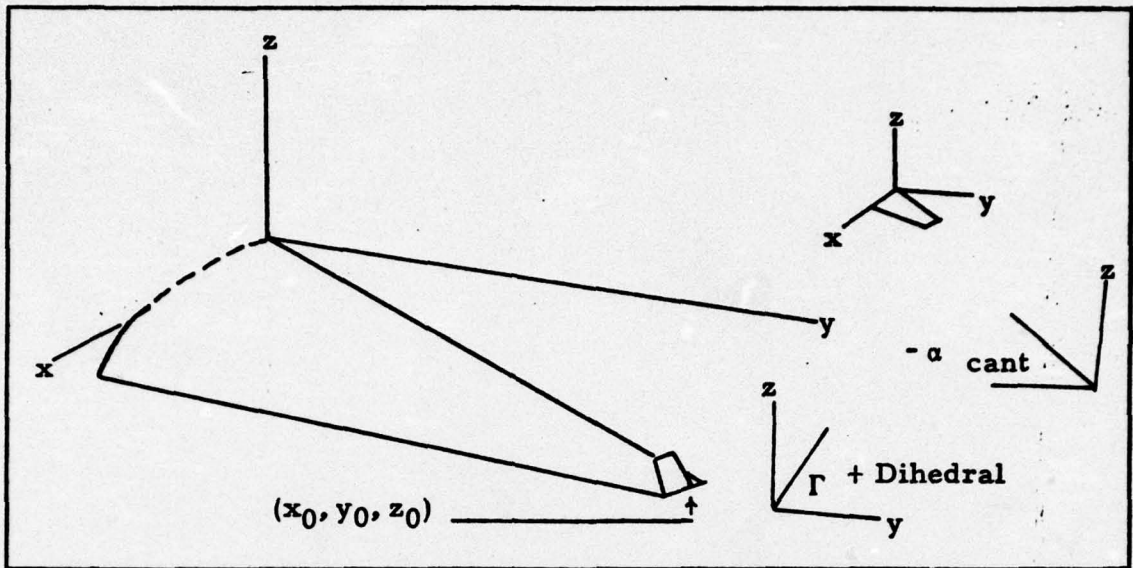


Fig. 3. Winglet Translation and Rotation

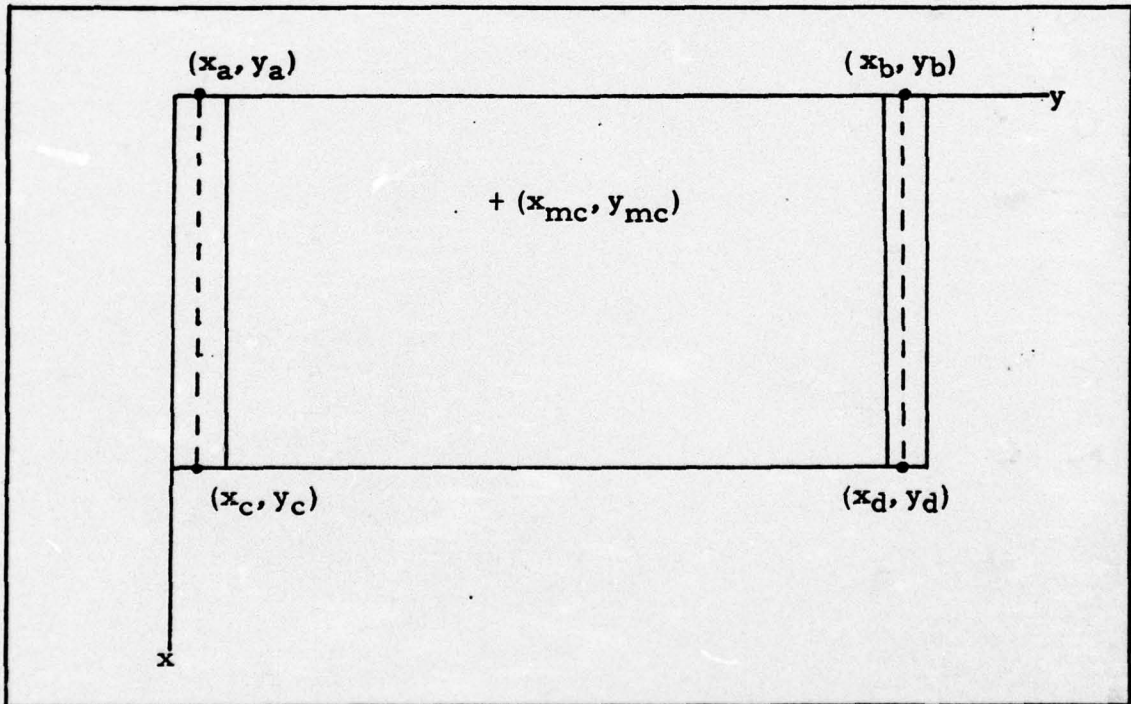


Fig. 4. Right Half of AR = 4, Rectangular Wing

NPLS approximation and the actual meanline is shown in Fig. 5.

The flight condition investigated was Mach = .211. Angles of attack ranged from zero through ten degrees.

The results calculated by the author are shown in Fig. 6 and are compared to the experimental results. As can be seen from this comparison, both  $C_{L0}$  and  $C_{L\alpha}$  are very well predicted. The shape of the drag polars agrees very well up to  $C_L \approx .8$  where experimental results indicate flow separation begins. The magnitude differences in these polars is due to the NPLS prediction of only induced drag. The slope of the pitching moment curve up to flow separation is well predicted although  $C_{M0}$  is slightly underpredicted. This discrepancy is consistent with other lifting surface theories and is probably due to thickness effects (Ref 5). These results are consistent with Douglas's calculations.

Figure 7 shows a comparison with experimental data for the same airfoil with a rectangular winglet attached. This winglet was a full chord winglet attached at a 90 degree dihedral angle and a zero degree cant angle. The winglet height was .765 of the main wing chord ( $.3825 b/2$ ). The camber distribution used for the winglet was that of a flat endplate.

As shown in Fig. 7,  $C_{L0}$  and  $C_{L\alpha}$  are very well predicted and the drag prediction is in very good agreement through  $C_L \approx .8$ . This method fails to accurately predict aerodynamic data after flow separation begins.  $C_{M0}$  is now slightly over predicted while the slope is still in very close agreement with experimental data.

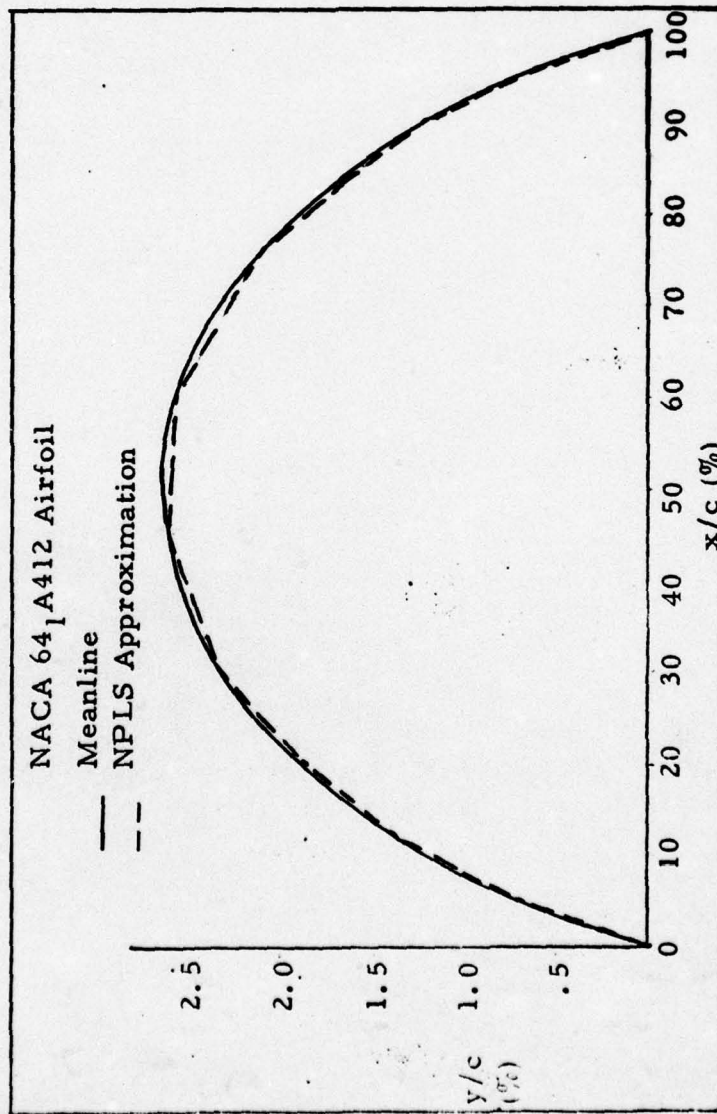


Fig. 5. NACA 64<sub>1</sub>A412 Camberline

Table II  
NACA 64<sub>1</sub>A412 Camber  
Angles

Centroid Location % Chord	Camber Angle (Degrees)
2.50	-8.53
6.25	-5.71
10.00	-4.25
16.25	-3.74
25.00	-2.47
37.50	-1.27
52.50	.40
67.50	1.67
82.50	4.50
92.50	5.64
96.25	5.57
98.75	5.57

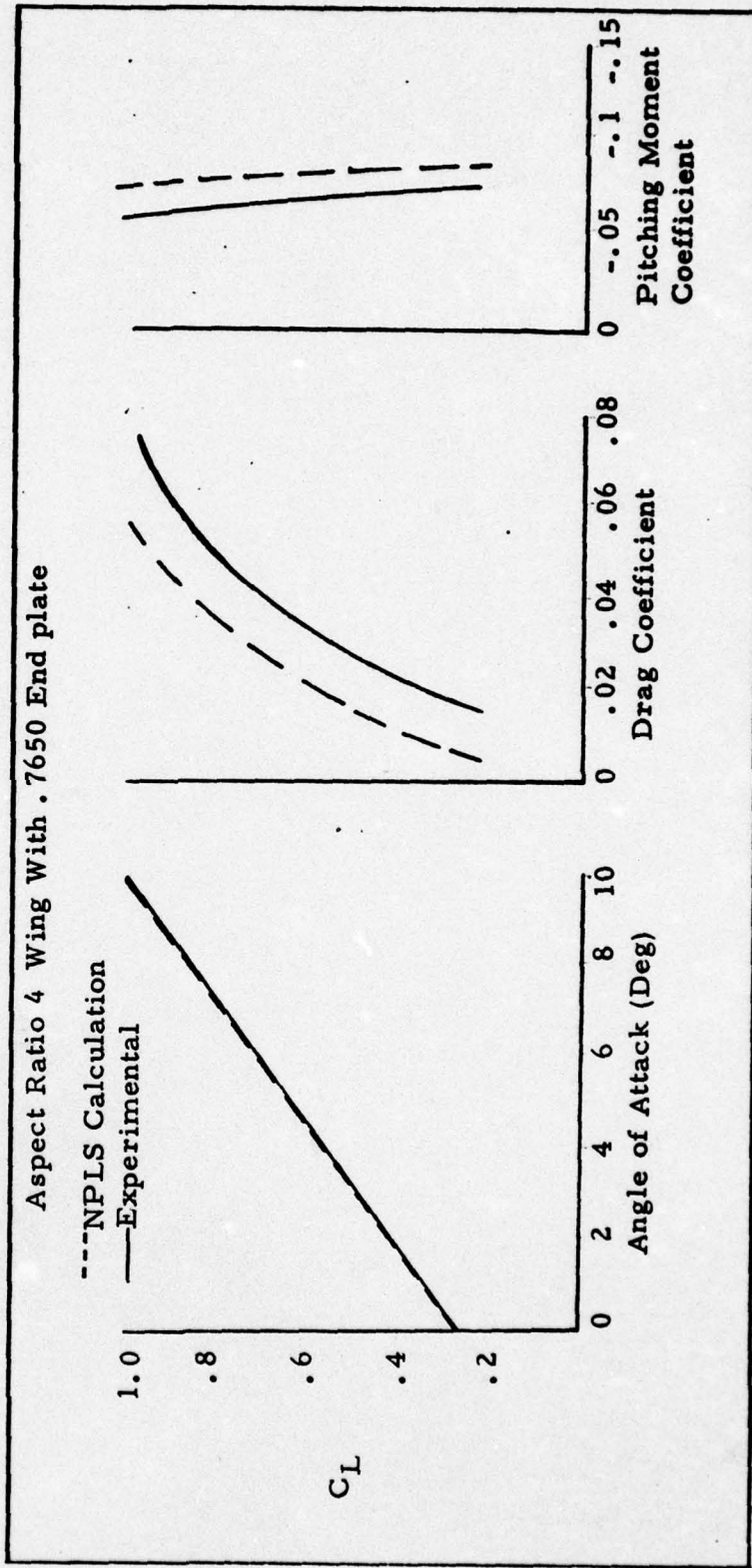


Fig. 7. Aerodynamic Characteristics of AR=4 Rectangular Wing With Endplate (Calculated vs Experimental)

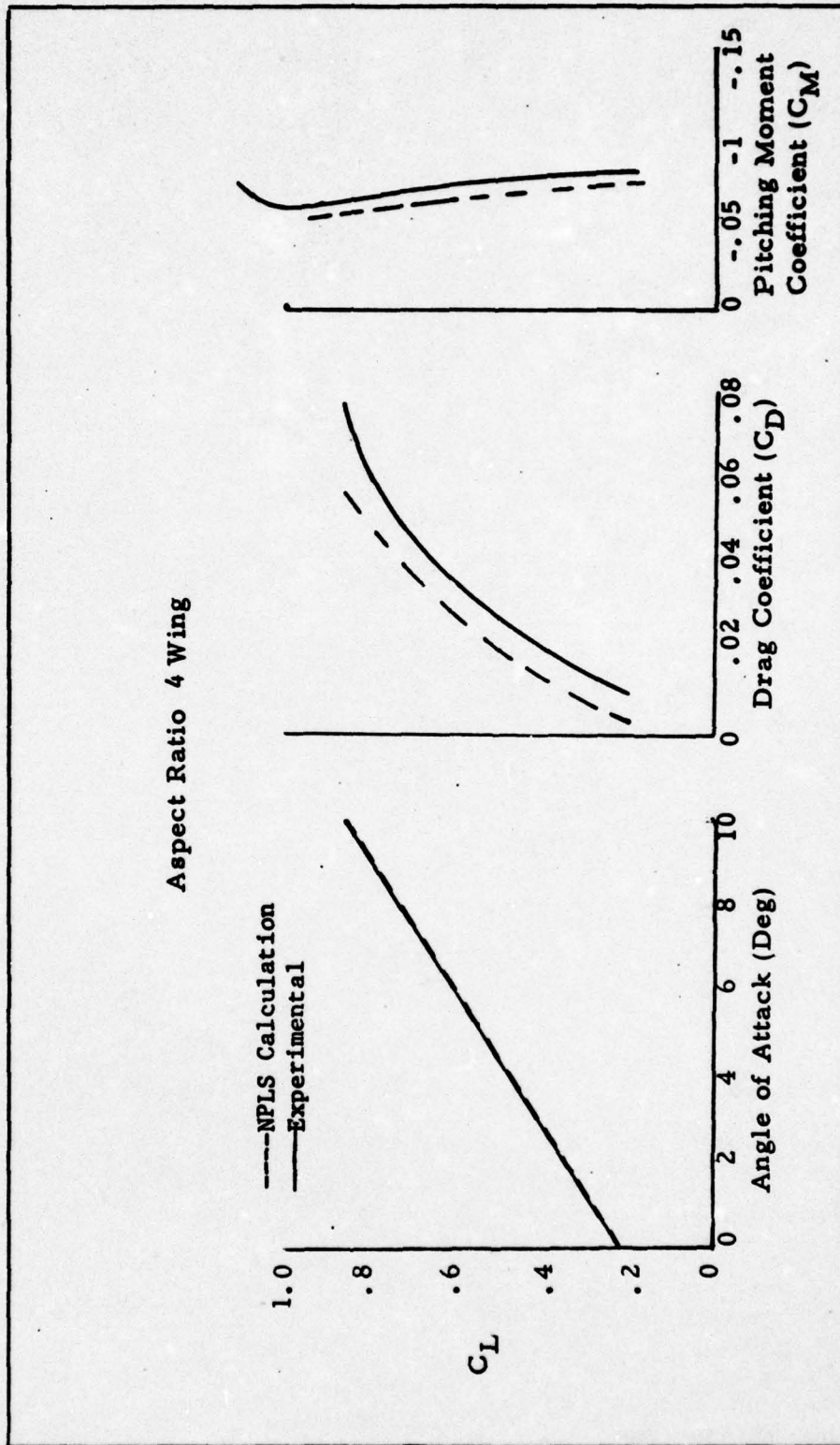


Fig. 6. Aerodynamic Characteristics of AR=4 Rectangular Wing (Calculated vs Experimental)

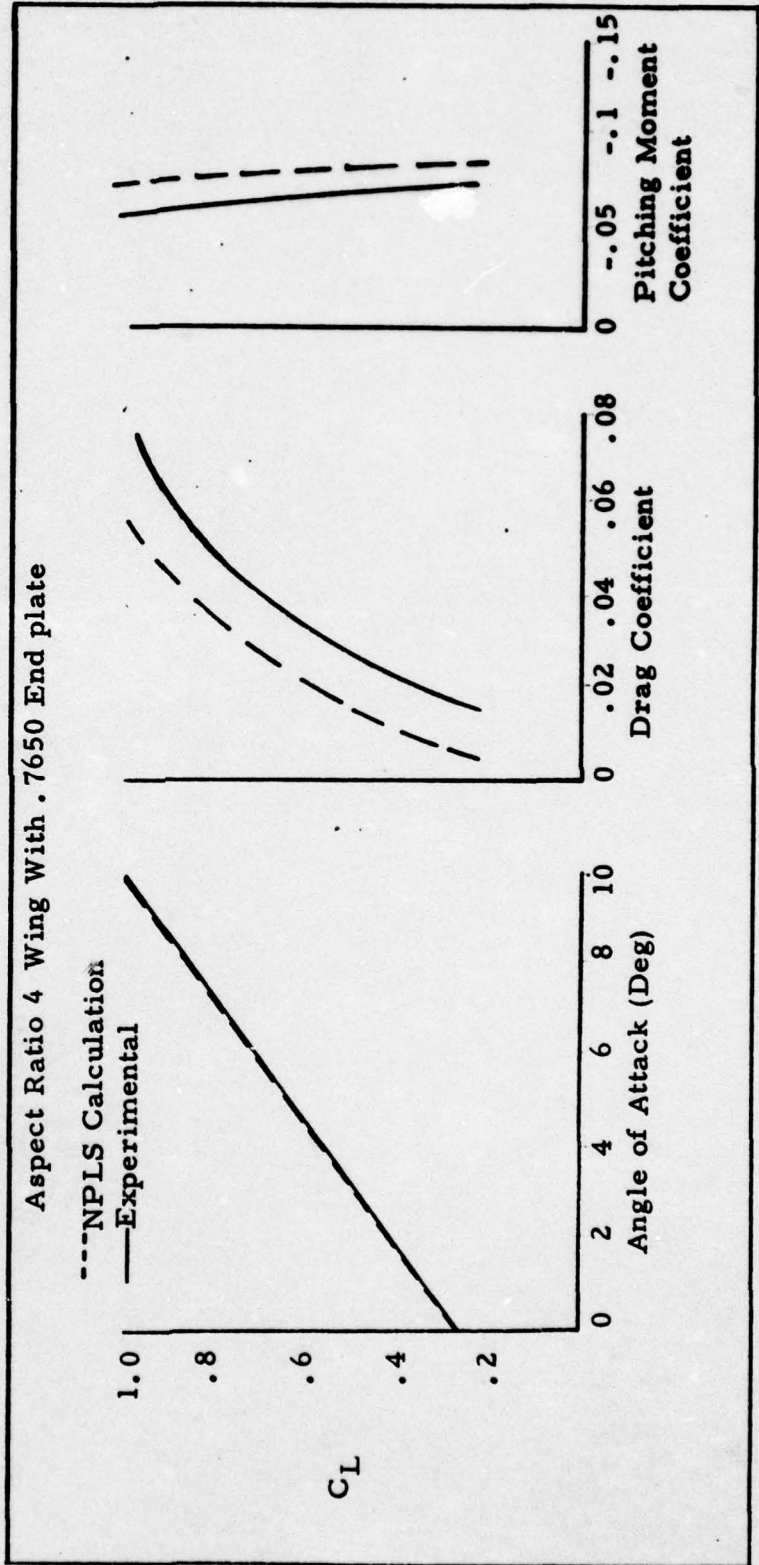


Fig. 7. Aerodynamic Characteristics of AR=4 Rectangular Wing With Endplate (Calculated vs Experimental)

The exact representation used by Douglas to model this wing was not presented in References 5 or 6. The author's model was constructed independently.

A comparison of the author's calculations with those calculated by Douglas (Ref 6:8) shows very little variation in lift coefficients and moment coefficients (2%). The drag coefficients presented in Ref 6 include a skin friction model and were a constant .010 higher than the author's for the wing alone and .012 higher for the wing with endplates attached.

This comparison of NPLS calculations with experimental data served as a validation for the model and the ability of the author to use it correctly. The next chapter describes how the model was used in the current parametric study.

### III. Calculation of Aerodynamic Coefficients

#### Wing Parameter Study

The object of this investigation was to determine the effects of winglets on a variety of planforms. Winglets have been investigated primarily with regard to their installation on transport wings similar to that of the KC-135.

This thesis examines winglet effectiveness on a variety of planforms in order to evaluate the benefits which could be expected on other types of aircraft and provide guidance for further study. The wing parameters which were varied were aspect ratio, wing sweep angle, and dihedral angle. The variation of these parameters and comparison of the resulting aerodynamic data offers insight into winglet effects on a variety of military and civil aircraft.

Although the NPLS method allows the representation of rather complex planforms, simple trapezoidal planforms were selected for this study. A tabular listing of the wing parameters which were varied is given in Table III. These wings are also illustrated in Fig. 8.

#### Winglet Cant Angle Study

The theory and experimental results of Reference 3 indicate that in order to be effective, winglets must produce significant side forces to reduce the lift induced inflow at the wing tip. NASA results indicate that the optimum winglet effectiveness occurs at negative (leading edge outboard) cant angles (Ref 3). A study by Douglas Aircraft Company indicates that at positive cant angles the greatest induced drag reduction occurs (Ref 5:45).

Table III  
Planform Parameters

AR	$\Lambda_{1/4c}$ (degrees)	$\Gamma$ (degrees)
7	15	0
7	25	0
7	35	0
7	45	0
7	15	10
7	15	-10
6	15	0
5	15	0
4	15	0
4	45	0

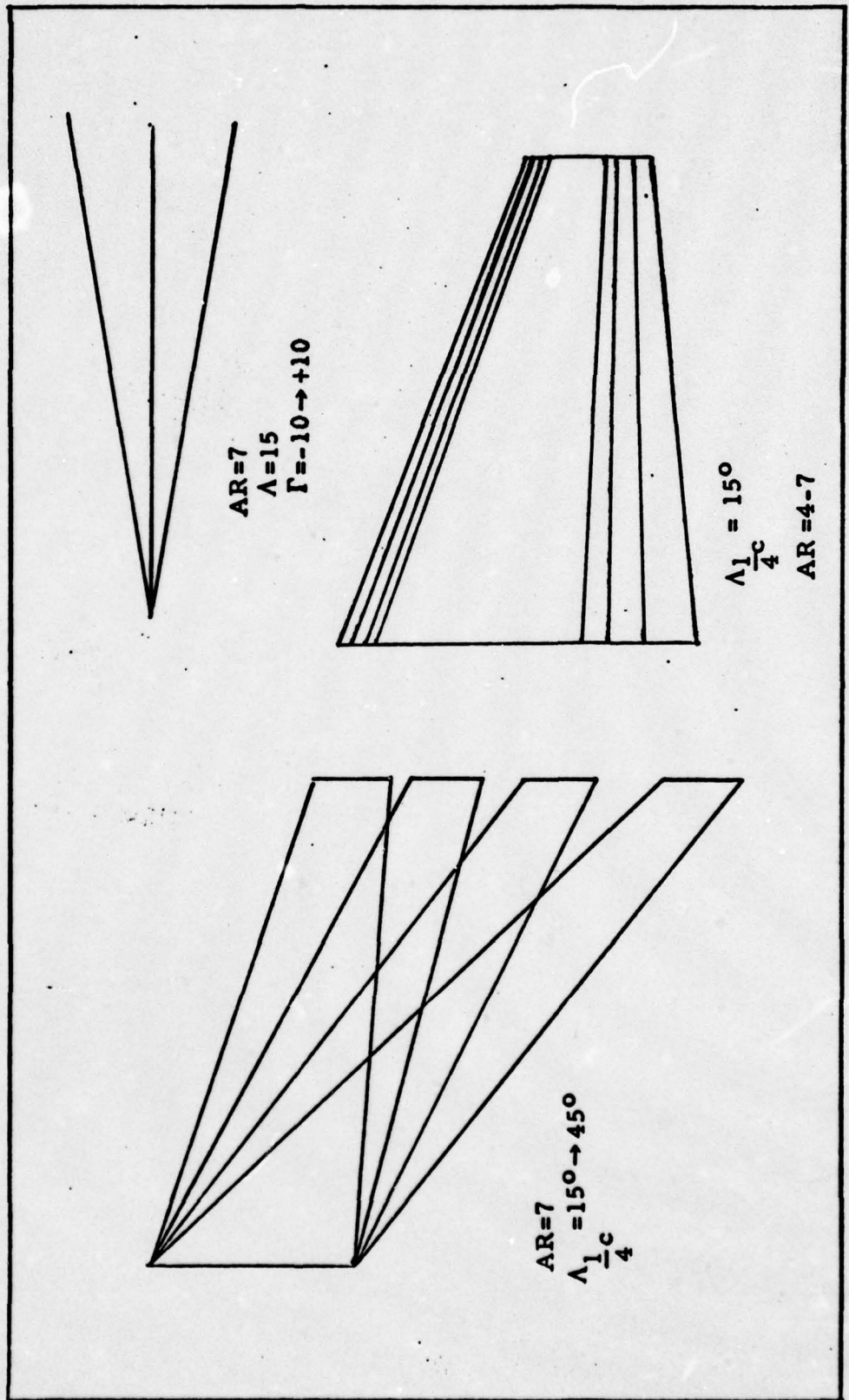


Fig. 8. Comparison of Planforms

To further investigate the effects of winglet cant angle on induced drag reduction, the cant angle on two planforms was varied between -3 degrees and +3 degrees in an attempt to find an optimum value.

#### Program Input

The procedure used in both of the above investigations was identical. In each case it was necessary to represent the lifting surface, or lifting system, as an array of rectangular elements. Once the necessary divisions were made, and the representation was complete, it remained to input the necessary wing and winglet parameters and definition points to the NPLS Computer Program to calculate the required aerodynamic coefficients. Aerodynamic data was calculated for five angles-of-attack with winglets and compared to that for the wing alone to determine the incremental effects due to winglet addition.

#### Airfoil

The basic airfoil section used to construct the wings in this investigation was the Boeing BAC 311 airfoil section. The camberline was approximated by the meanline of the airfoil ordinates with the following relation

$$\eta_c = \frac{1}{2} (\eta_l + \eta_u) \quad (2)$$

Twelve chordwise elements were used to obtain the approximation shown in Fig. 9. Table IV lists the slopes of the camberline (in degrees) which were input to the NPLS program. These values were determined analytically from

$$\epsilon = \tan^{-1} \frac{\Delta \eta_c}{\Delta x} \quad (3)$$

In Eq (3),  $\epsilon$  represents the camber angle at the midpoint of each rectangular element.  $x$  is the chordwise location measured in percent of total chord.

#### Planform Definition

Fourteen spanwise divisions were made using the criteria described in Chapter II. Thus, each wing was represented by 168 (12 X 14) rectangular elements.

For simplicity, all wing distance parameters were non-dimensionalized by the wing semispan ( $b/2$ ). Since all configurations analyzed were symmetric, only the right half of each planform was defined. The NPLS program formed the entire wing using a mirror image technique. Given the aspect ratio, AR, the non-dimensional reference area, S, was found from the non-dimensional wing span, b, using the definition of aspect ratio

$$AR = \frac{b^2}{S} \quad (4)$$

The taper ratio,  $\lambda$ , remained constant ( $\lambda = 1/3$ ) for each planform. The root chord and tip chord length were found from the following relation for trapezoidal wings.

$$AR = \frac{2b}{c_r (1 + \lambda)} \quad (5)$$

$$c_t = \lambda c_r$$

$\Lambda_{1/4c}$  was specified for each planform. The leading and trailing edge coordinates required to define each planform were found using

$$\tan \Lambda_{LE} = \tan \Lambda_{1/4c} + \frac{1}{AR} \frac{(1 - \lambda)}{(1 + \lambda)} \quad (6)$$

Table IV  
BAC 311 Camber Angles

Centroid Location X (% Chord)	Camber Angle $\epsilon$ (Degrees)
2.50	-8.794
6.25	-5.450
10.00	-2.634
16.25	+ .477
25.00	+ .371
37.50	+ .505
52.50	+ .819
67.50	+1.529
82.50	1.705
92.50	1.704
96.25	1.704
98.75	1.704

(Angles are positive in Angle of Attack sense)

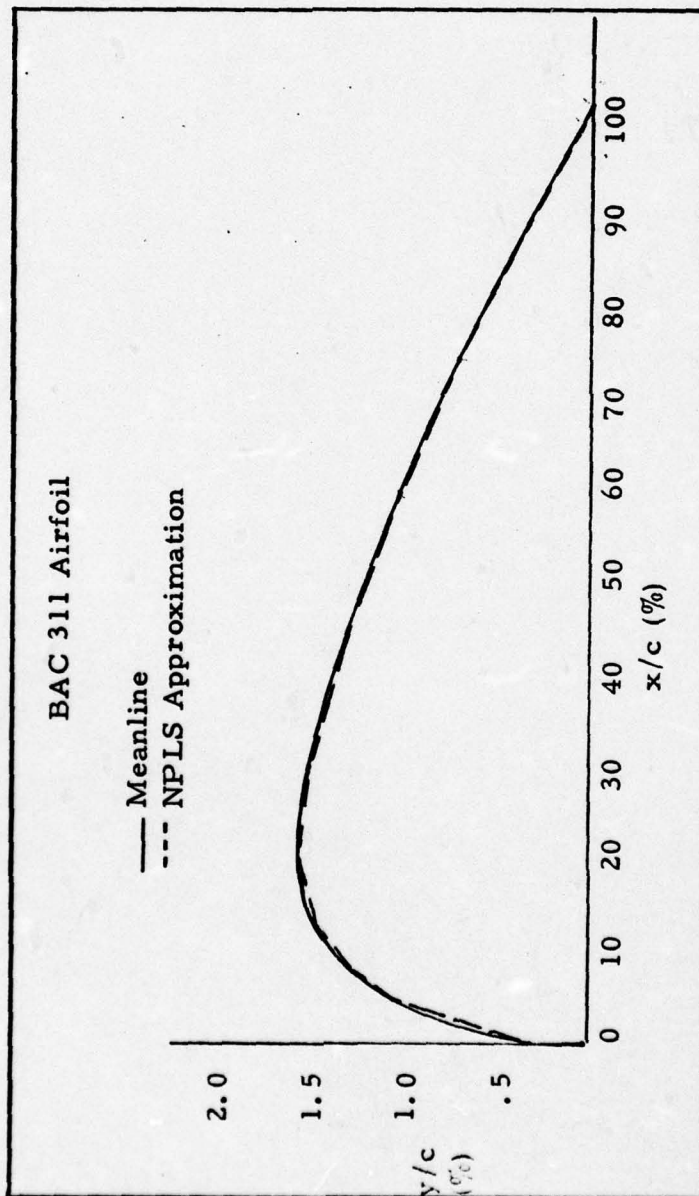


Fig. 9. Boeing BAC 311 Meanline

$$\tan\Lambda_{TE} = \tan\Lambda_{1/4c} - \frac{3}{AR} \frac{(1 - \lambda)}{(1 + \lambda)} \quad (6)$$

The mean aerodynamic chord and location of the moment center for a trapezoidal wing are given by the following relations (Ref 8:3, 17)

$$\bar{c} = \frac{2}{3} \left( \frac{1 + \lambda + \lambda^2}{1 + \lambda} \right)$$

$$y_{mc} = \frac{b}{6} \frac{(1 + 2\lambda)}{(1 + \lambda)} \quad (7)$$

$$x_{mc} = \frac{c_r}{4} + y_{mc} \tan\Lambda_{1/4c}$$

All of the required points and parameters necessary to fully define a wing for the NPLS program are illustrated in Fig. 10. The parameters calculated for the planforms in this study are listed in Table V.

### Winglets

The winglet selected for use in this investigation was similar to that selected for use on the KC-135 (Ref 4:12). Although some investigations (Ref 2 and 3) to date have examined the effects of both an upper and a lower winglet, only the upper winglet was examined here. This winglet (Fig. 11) was mounted on all planforms with an incidence angle of zero degrees for the planform analysis. Although NASA tests indicate a substantial negative incidence angle may be used, zero degrees was selected as a baseline value for this study (Ref 2 and 3). In all cases the winglet was mounted with the winglet trailing edge flush with the wing trailing edge and mounted at a 70 degree dihedral angle. The winglet was cambered inboard to produce the inward loads necessary to reduce the lift induced inflow and decrease the induced drag. This location

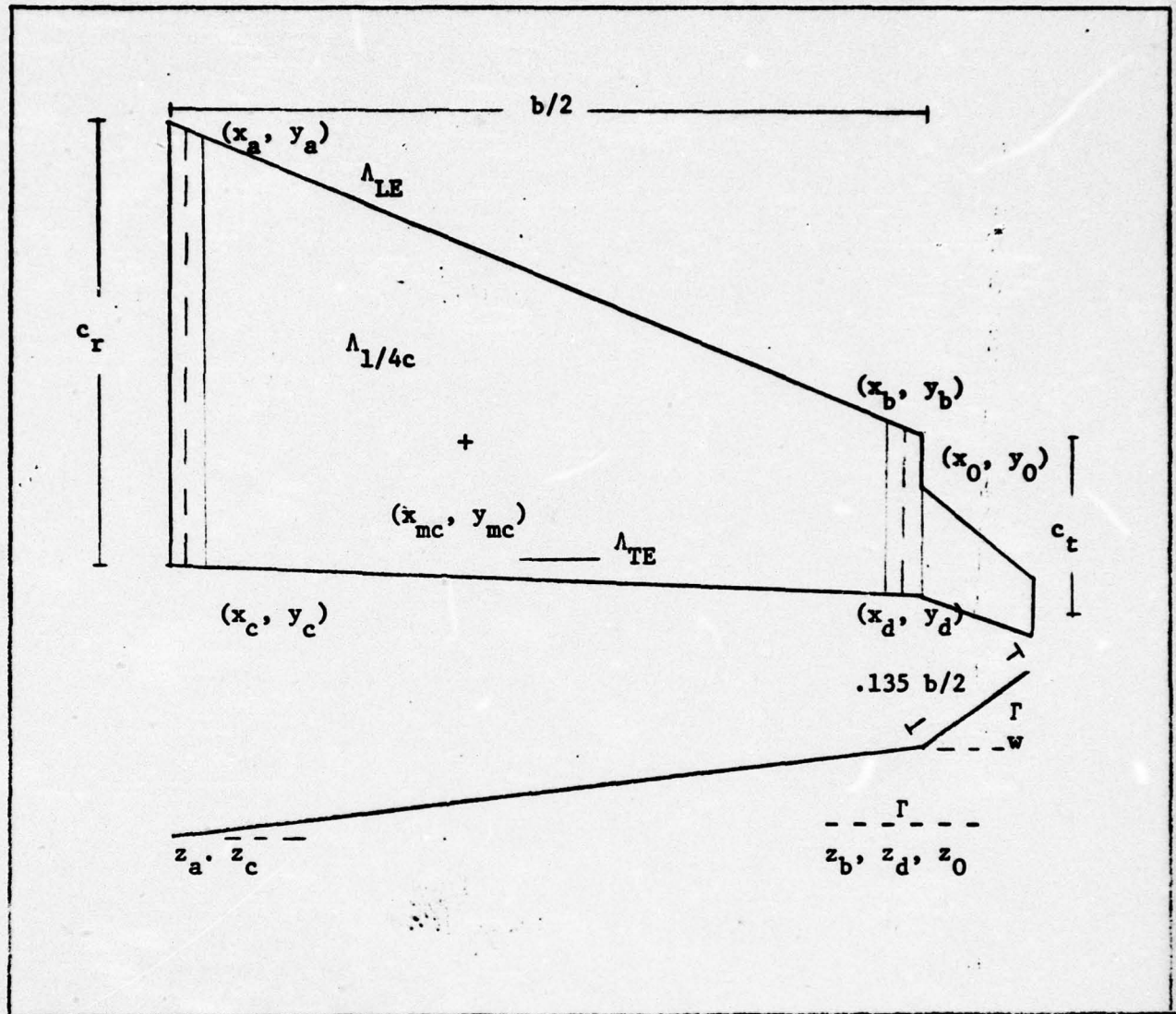


Fig. 10. Wing Parameters and Points of Definition

Table V  
NPLS Program Input Parameters

Wing #	AR	b	S	$\lambda$	$c_r$	$c_t$	$\frac{\Delta l}{4} c$	$\Delta LE$ (degrees)	$\Delta TE$
1	7	2	.5714	.333	.4286	.1429	15	18.746	3.072
2	7	2	.5714	.333	.4286	.1429	25	28.269	14.145
3	7	2	.5714	.333	.4286	.1429	35	37.655	25.916
4	7	2	.5714	.333	.4286	.1429	45	46.975	38.157
5	6	2	.6667	.333	.5000	.1667	15	19.355	1.028
6	5	2	.8000	.333	.6000	.2000	15	20.201	-1.836
7	4	2	1.0000	.333	.7500	.2500	15	21.452	-6.110
8	4	2	1.0000	.333	.7500	.2500	45	48.366	32.005

Wing #	$\bar{c}$	$x_{mc}$	$y_{mc}$	$x_a$	$x_b$	$x_c$	$x_d$
1	.3095	.2188	.4167	.00679	.33514	.42964	.48156
2	.3095	.3014	.4167	.01075	.53101	.43361	.67744
3	.3095	.3989	.4167	.01543	.76199	.43829	.90842
4	.3095	.5238	.4167	.03143	1.05803	.44429	1.20446
5	.3611	.2366	.4167	.00703	.34688	.50004	.51772
6	.4333	.2616	.4167	.00736	.36335	.59936	.56835
7	.5417	.2991	.4167	.00786	.38803	.74786	.64429
8	.5417	.4337	.4167	.02249	1.11902	.76250	1.36718

and placement has been shown to be near optimum (Ref 3:6).

The winglet airfoil section used in this analysis is the NASA general aviation airfoil described in Reference 3. The ordinates of this airfoil are listed in Table VI. The camber angles for this airfoil were calculated as described previously and are listed in Table VII. Figure 12 shows the resulting camberline approximation used in this analysis.

#### Winglet Definition

Each winglet was represented by 84 (7 spanwise and 12 chordwise) rectangular elements based on the criteria covered in Chapter II. By inputting the winglet aspect ratio (2.32), taper ratio (.338) quarter-chord sweep (32.918 degrees), spanwise divisions, and chordwise divisions, the winglet was fully defined. The winglet orientation was specified by inputting the cant and dihedral angles illustrated previously in Fig. 3. Winglet location was specified by inputting the coordinates  $(x_0, y_0, z_0)$  of the winglet apex. The  $y_0$  and  $z_0$  coordinates were identical to the wing tip coordinates when winglet cant was zero. The value of  $x_0$  was calculated which placed the trailing edge of the winglet flush with the trailing edge of the main wing

$$x_0 = c_r (\text{wing}) + y_0 \tan \Lambda_{TE} - c_r (\text{winglet}) \quad (8)$$

When a positive winglet cant angle was used, the apex of the winglet was moved inboard to prevent a gap between the wing and winglet. The new  $y$  coordinate of the winglet apex was

$$y_0 = l. - c_r (\text{winglet}) \sin \alpha_{\text{cant}} \quad (9)$$

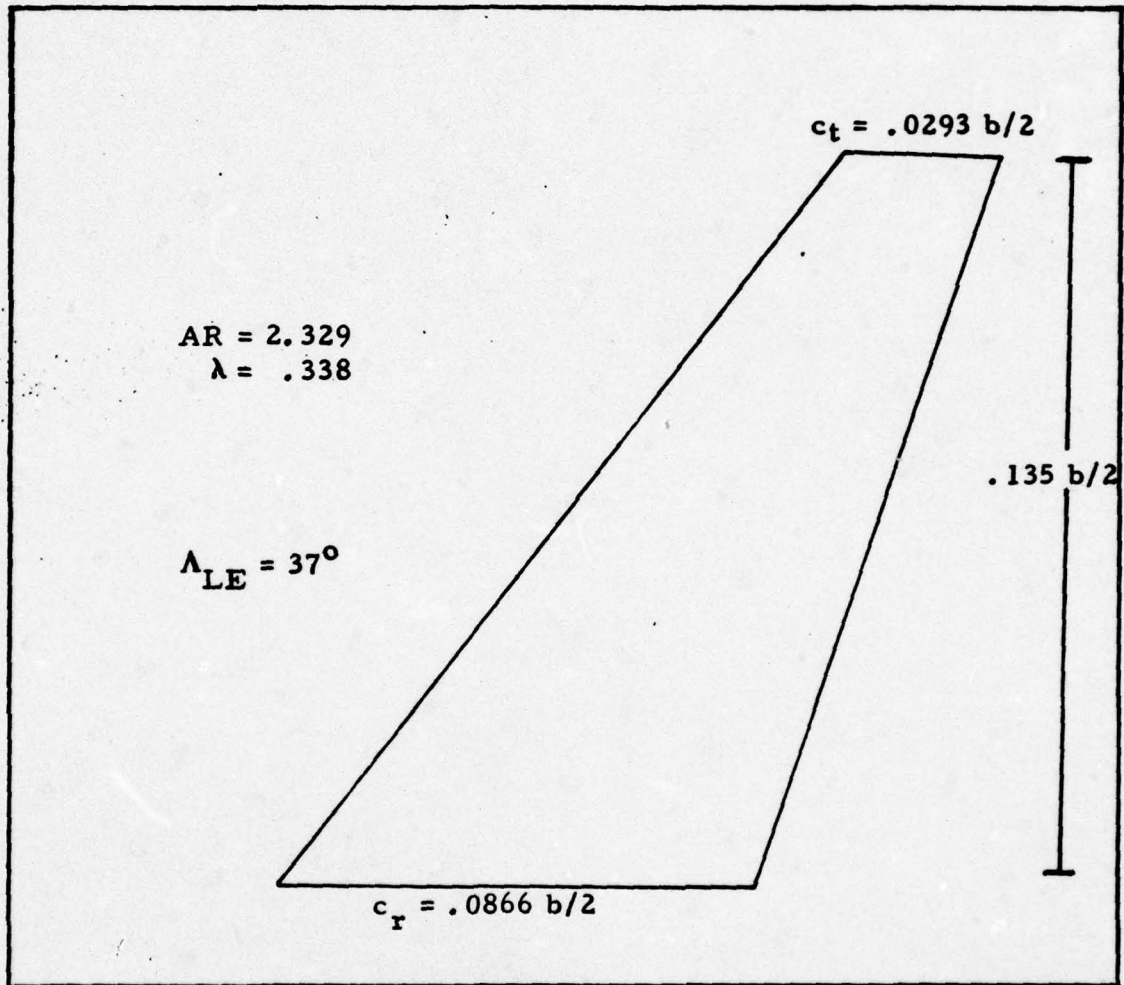


Fig. 11. Winglet Parameters

Table VI  
Airfoil Coordinates for Winglets

x/c	y/c for	
	Upper Surface	Lower Surface
0	0	0
.0020	.0077	-.0032
.0050	.0119	-.0041
.0125	.0179	-.0060
.0250	.0249	-.0077
.0375	.0296	-.0090
.0500	.0333	-.0100
.0750	.0389	-.0118
.1000	.0433	-.0132
.1250	.0469	-.0144
.1500	.0499	-.0154
.1750	.0525	-.0161
.2000	.0547	-.0167
.2500	.0581	-.0175
.3000	.0605	-.0176
.3500	.0621	-.0174
.4000	.0628	-.0168
.4500	.0627	-.0158
.5000	.0618	-.0144
.5500	.0599	-.0122
.5750	.0587	-.0106
.6000	.0572	-.0090
.6250	.0554	-.00771
.6500	.0533	-.0052
.6750	.0508	-.0033
.7000	.0481	-.0015
.7250	.0451	.0004
.7500	.0419	.0020
.7750	.0384	.0036
.8000	.0349	.0049
.8250	.0311	.0060
.8500	.0270	.0065
.8750	.0228	.0064
.9000	.0184	.0059
.9250	.0138	.0045
.9500	.0089	.0021
.9750	.0038	-.0013
1.0000	-.0020	-.0067

**Table VII**  
**NASA Winglet Camber Angles**

Centroid Location X (% Chord)	Camber Angle $\epsilon$ (Degrees)
2.50	-13.116
6.25	-4.346
10.00	-3.091
16.25	-2.100
25.00	-1.403
37.50	-.764
52.50	-.248
67.50	.821
82.50	3.738
92.50	7.576
96.25	9.648
98.75	12.626

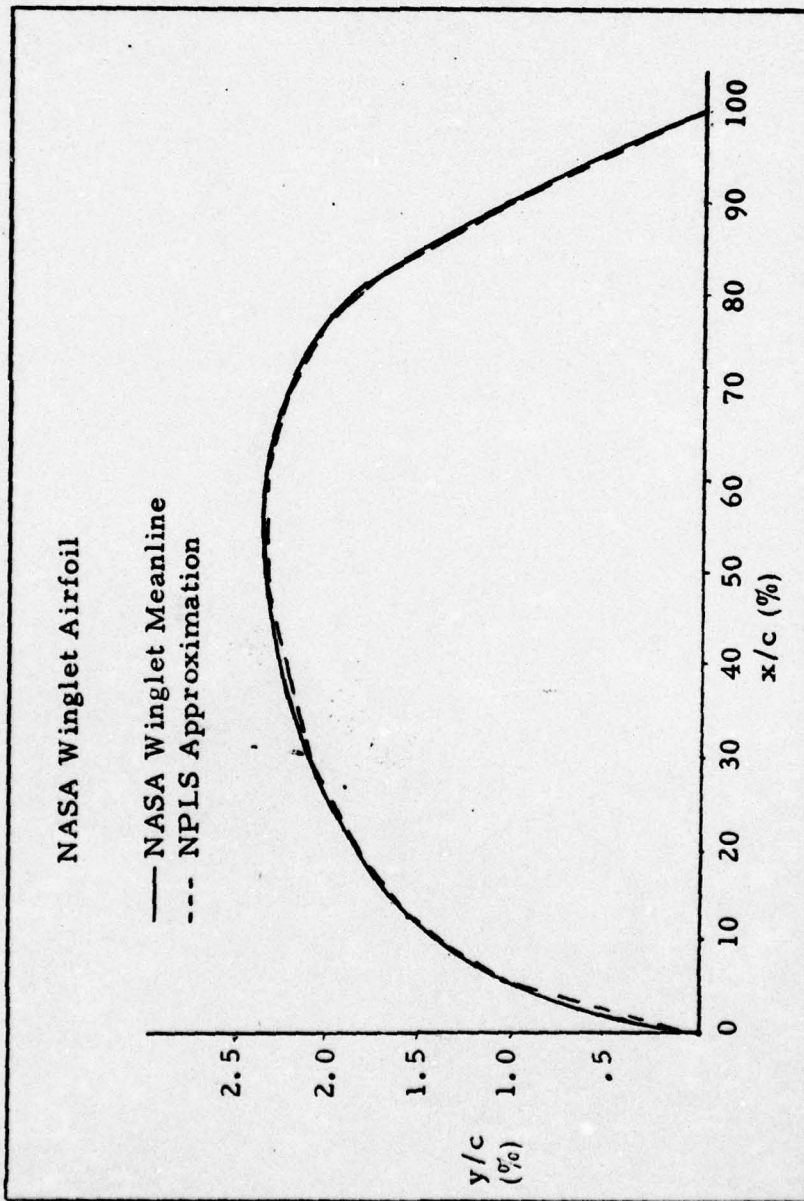


Fig. 12. NASA Winglet Airfoil Meanline

### NPLS Program Use

Once the required parameters were calculated, they were arranged in the proper input format (Ref 5:72-80).

The flight condition was specified by inputting the desired Mach number and as many as five separate angles of attack. Mach .7 was selected for use in this investigation. Angles of attack of zero through six degrees were investigated. These safely represent those flight conditions for which flow separation is not a factor.

The computer program has provisions to check input data for inconsistencies, however, the input was closely rechecked to insure the desired representation was obtained.

For the wing-winglet combinations used in this analysis (252 rectangular elements), approximately 130 CP seconds execution time were required.

### Program Output

The program output for each case began with a listing of the basic geometric parameters. This was followed by a detailed element-by-element listing of geometric data. This data was carefully compared to the input data to insure the desired representation was obtained. Local dihedral angles were carefully checked to insure the surface was not excessively warped. Had an excessive local dihedral angle existed, the representation would have been altered to better represent the desired wing. No automatic check for surface gaps exists in this program. Only by carefully analyzing the aerodynamic data could an irregularity such as a gap between wing and winglet be detected.

The NPLS program does not include a plotting routine. Since all output was in tabular form, a plotting routine was written to display graphically the calculated coefficients. Samples of these aerodynamic plots are found in the next chapter; the remainder are located in Appendices B and C.

#### IV. Results

##### Wing Parameter Study

Figures 13-18 are representative of the aerodynamic plots contained in Appendix B. These plots illustrate the effect of winglet addition to each particular wing investigated. These curves show the lift coefficient as a function of angle of attack (Figure 13), induced drag coefficient (Fig 14), pitching moment coefficient (Fig. 16), and root bending moment coefficient (Fig. 17). Also shown is lift coefficient squared,  $C_L^2$ , as a function of the induced drag coefficient (Fig. 15) and the variation in spanwise loading,  $c \cdot C_1 / \bar{c} \cdot C_L$  vs % span for  $\alpha = 4-1/2$  degrees (Fig. 18).

An analysis of the resulting lift curves shows that for each wing an increase in  $C_{L\alpha}$  results from the addition of winglets. This increase, shown in Fig. 13 for example, coupled with a slight increase in  $C_{L0}$ , allows the wing to develop the required lift at a lower angle of attack and reduce wing parasite drag.

Figure 14 shows a typical drag reduction resulting from winglet addition. This drag reduction is accompanied by an increase in the nose down pitching moment,  $C_M$ , as shown in Fig. 16, and an increase in the wing root bending moment coefficient (Fig. 17). The pitching moment curves show an improvement in static longitudinal stability, however, the increased nose down moment must be balanced by a down load on the horizontal tail which negates part of the induced drag reduction. The increased root bending moment is due to the outboard shift in wing loading as shown in Fig. 18.

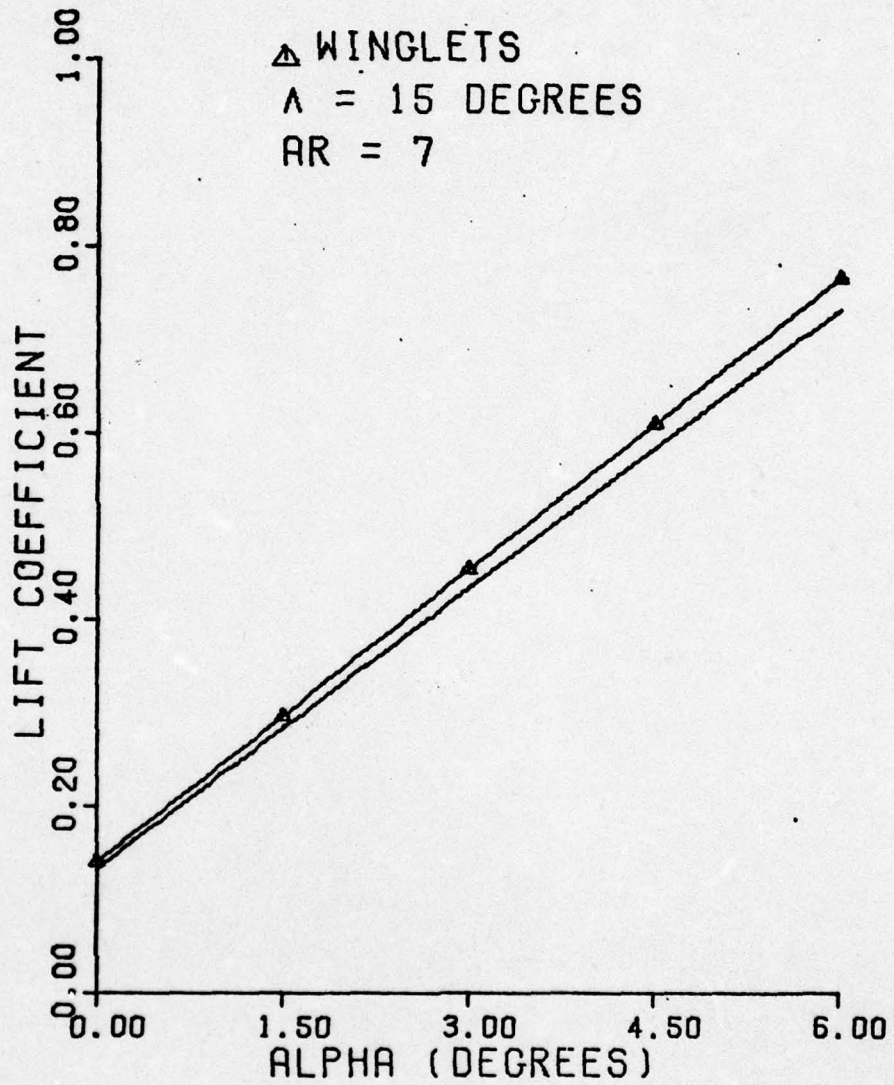


Fig. 13. Wing #1 Lift Curves

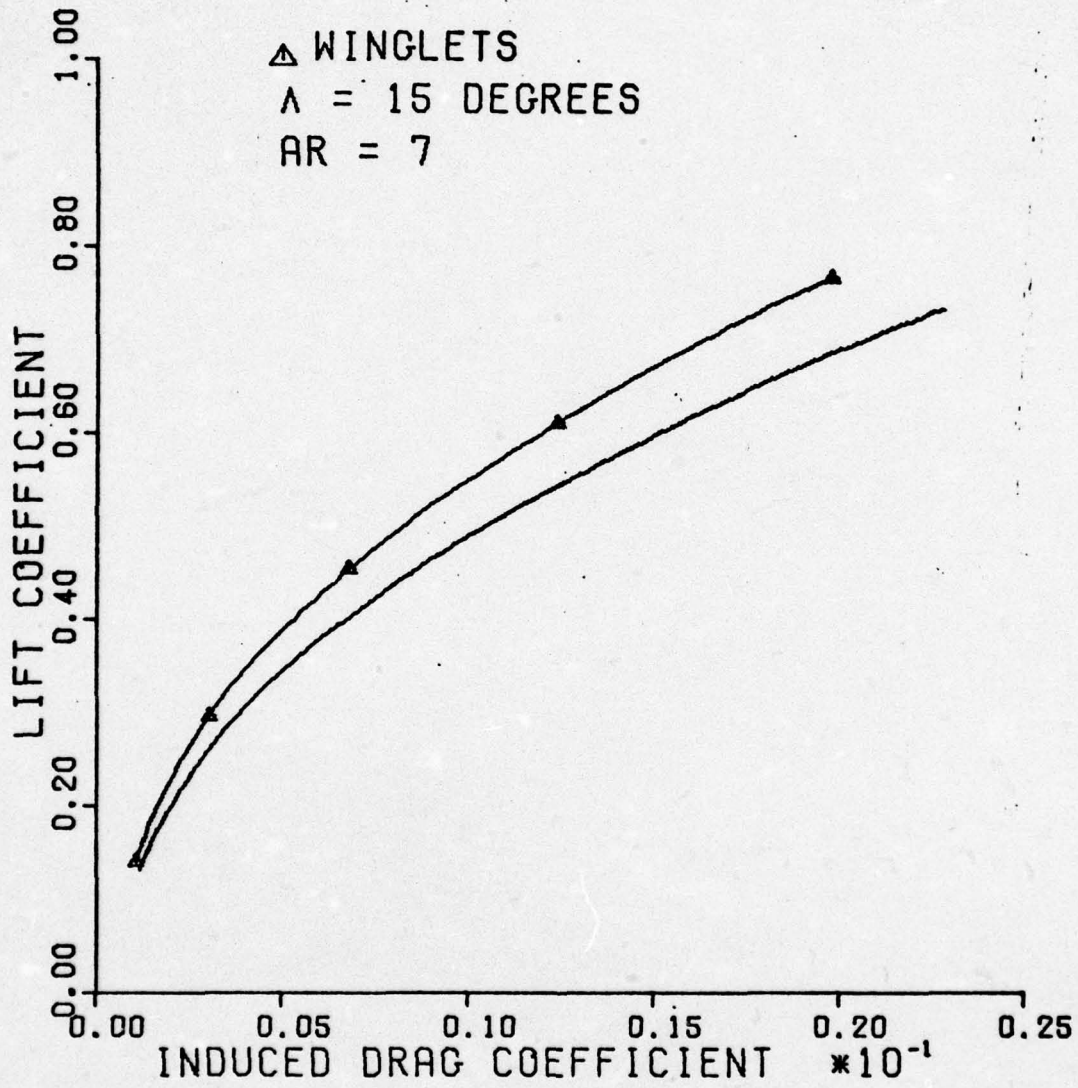


Fig. 14. Wing #1 Drag Polars

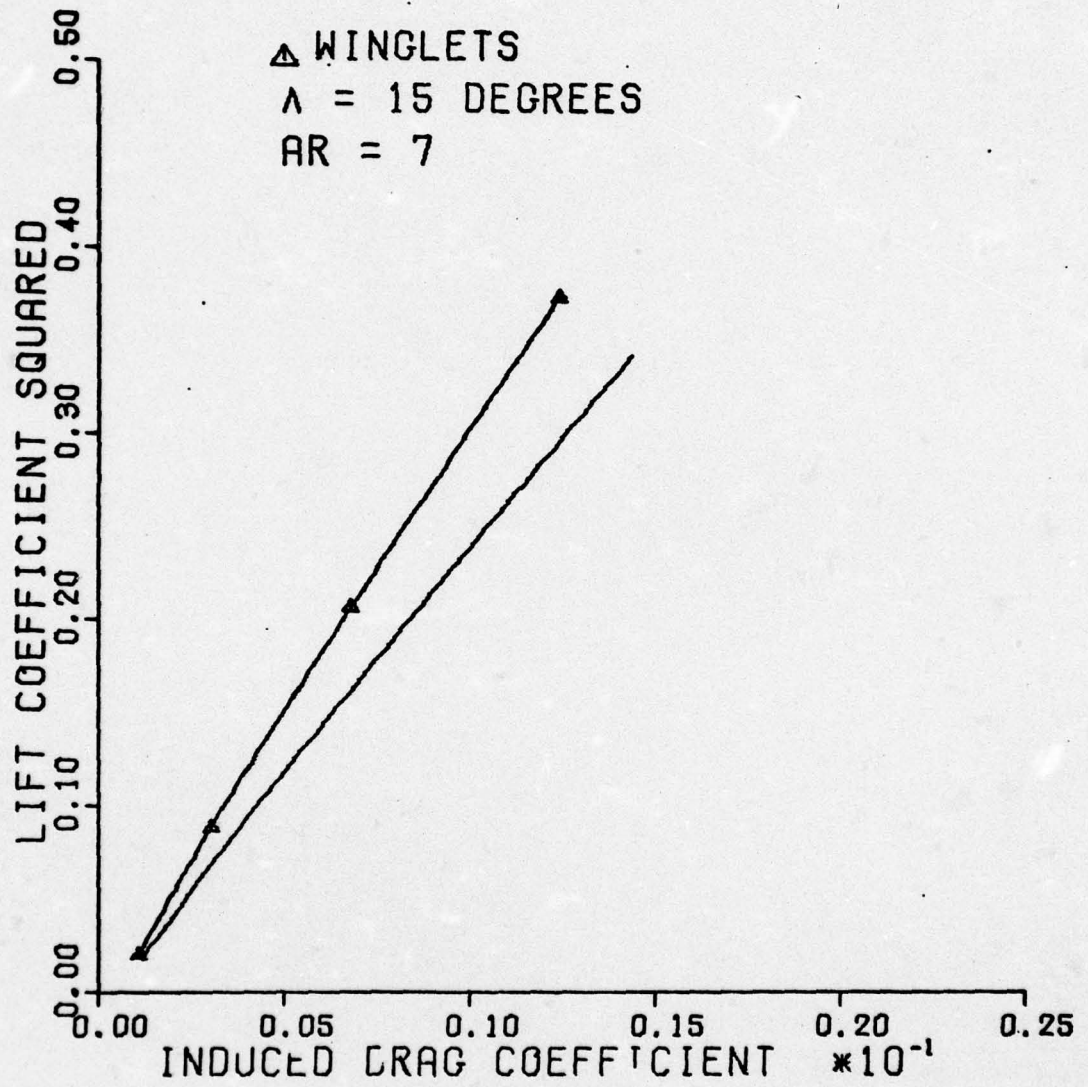


Fig. 15.  $C_L^2$  vs  $C_{Di}$  for Wing #1

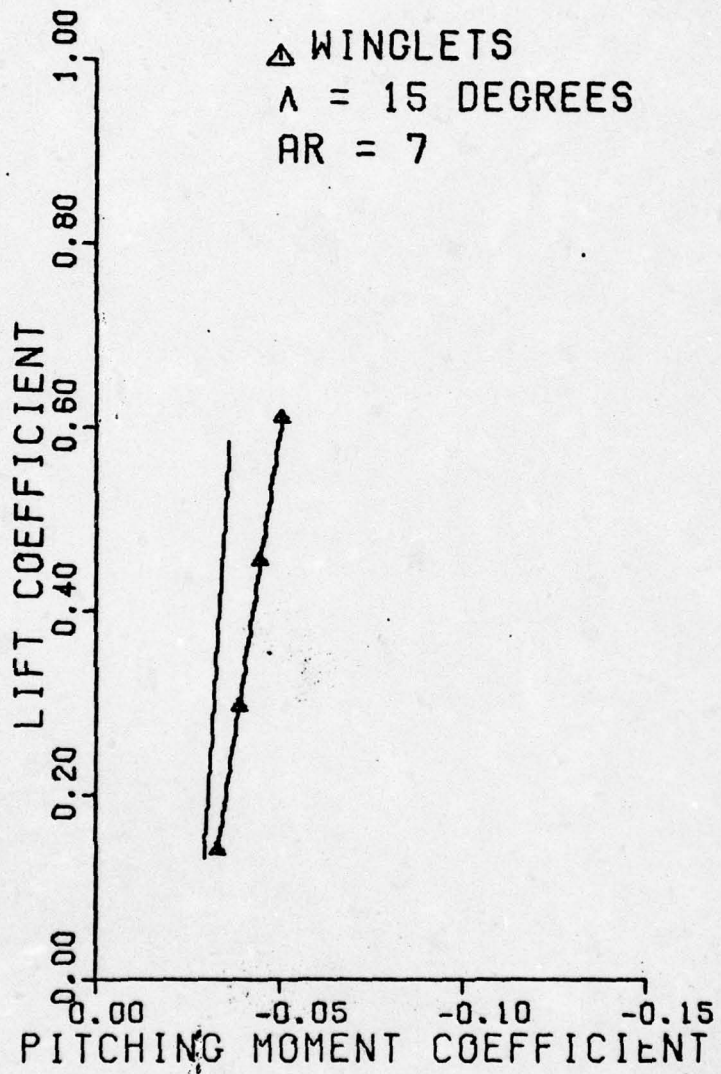


Fig. 16. Wing #1 Pitching Moments

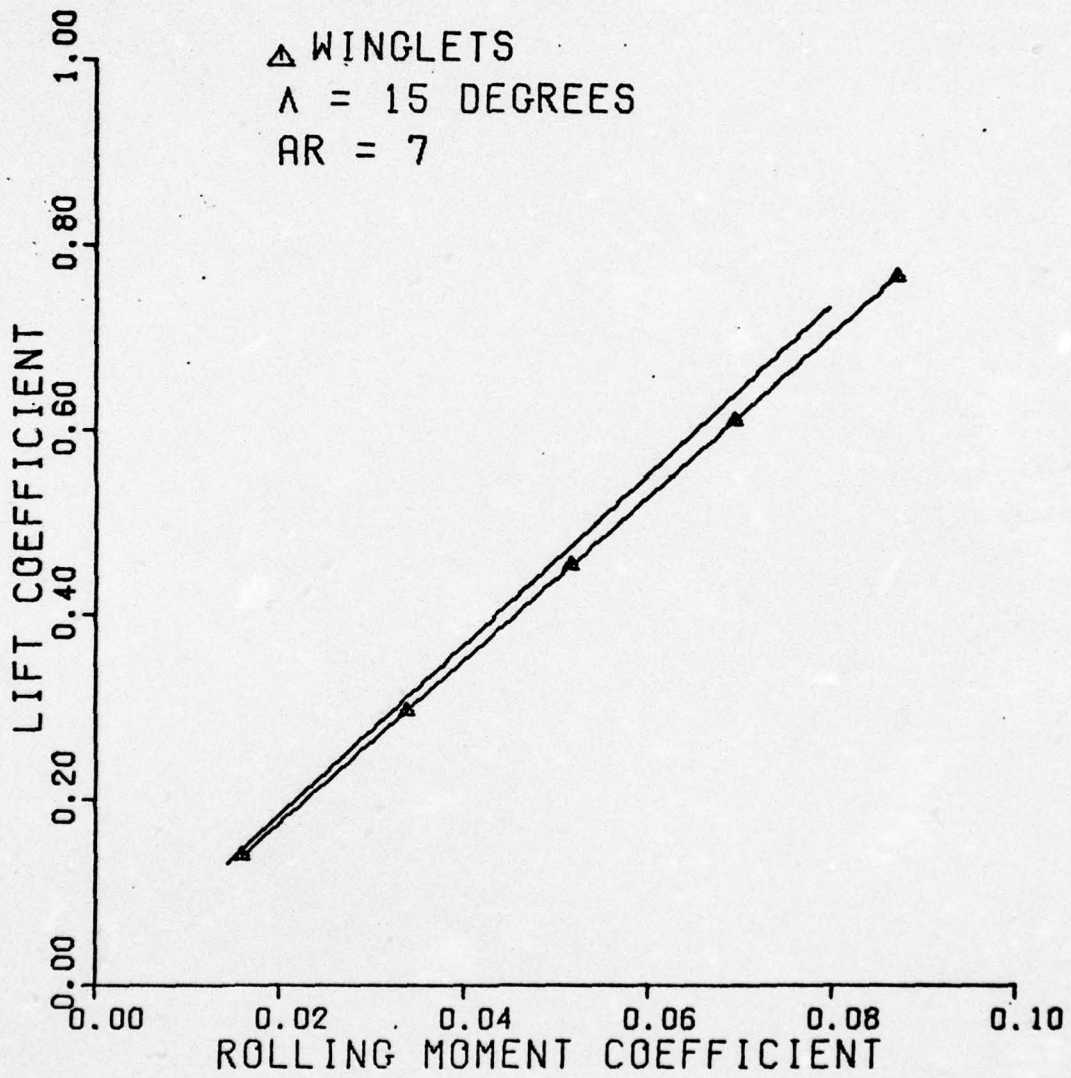


Fig. 17. Wing #1 Root Bending Moments

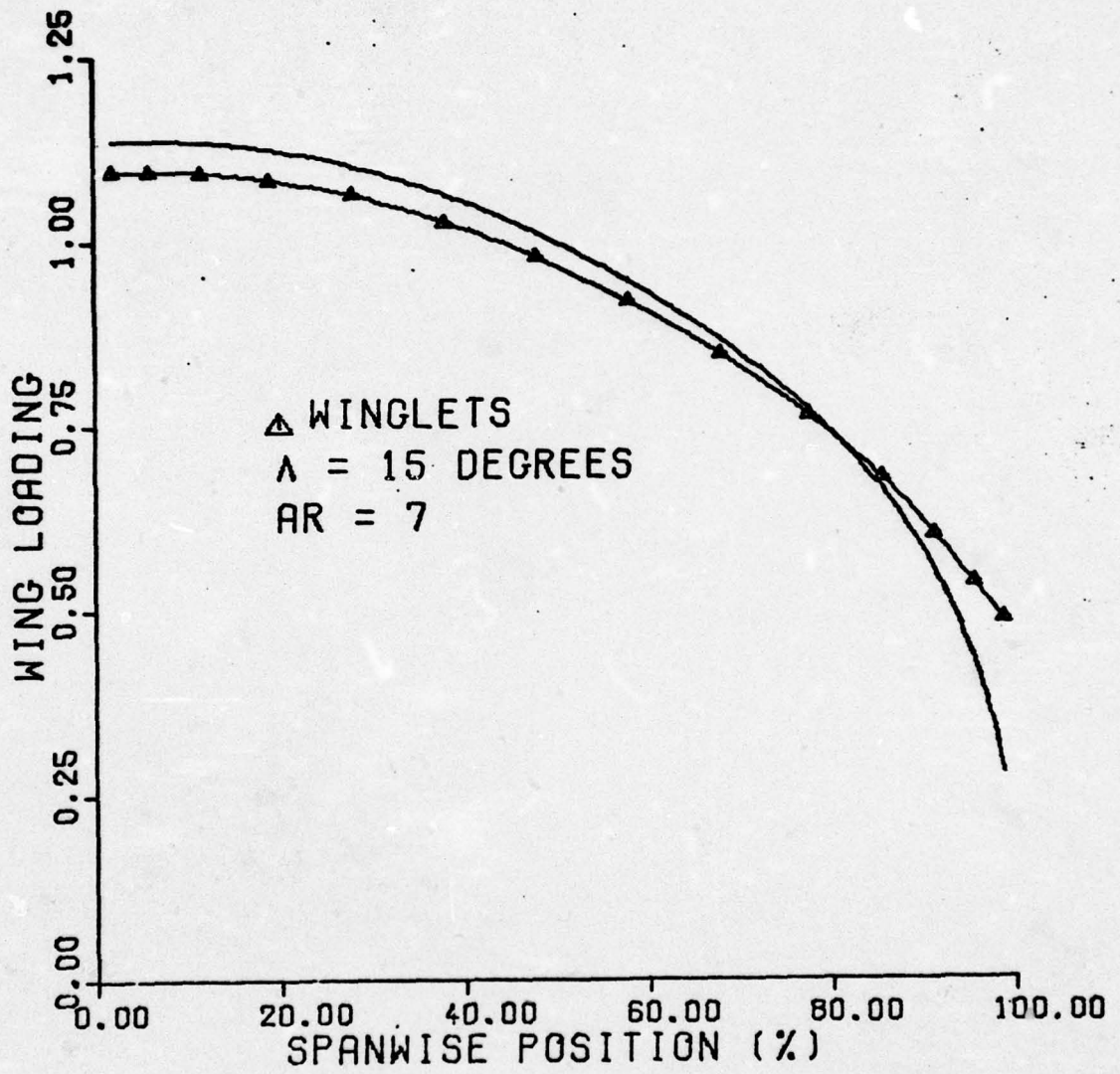


Fig. 18. Spanwise Loading for Wing #1

Figure 15 and the remaining plots of  $C_L^2$  vs  $C_{Di}$  are approximately linear, which suggests that the induced drag can be represented by

$$C_{Di} = \frac{C_L^2}{\pi AR e} \quad (10)$$

where  $e$  represents the induced drag efficiency factor. Values of  $e$  are calculated for each planform and the ratio,  $e'/e$ , where the prime indicates the value with winglets, is shown as a function of aspect ratio, wing sweep angle, and wing dihedral angle in Fig. 19. The factor  $e'/e$  relates directly to the percentage reduction in induced drag

$$\frac{\Delta C_{Di}}{C_{Di}} = 1 - e/e' \quad (11)$$

It should be noted that the above relationship assumes that the aerodynamic improvement due to winglet addition is solely accounted for in the efficiency factor,  $e'$ , and the aspect ratio remains constant.

In Fig. 19, the factor  $e'/e$  is seen to improve as aspect ratio increases. This indicates that the percentage induced drag reduction is greatest on the higher aspect ratio wings. The percentage drag reduction increases almost linearly with increasing wing sweep angle, but increases only slightly with increasing dihedral angle.

#### Longitudinal Results

Figure 20 illustrates the effect of wing sweep angle on induced drag reduction and pitching moment increment. For each sweep angle the change in induced drag reduction is proportional to the square of the lift coefficient as indicated by Eq (10). As wing sweep angle increases, induced drag reduction increases slightly more than linearly, indicating

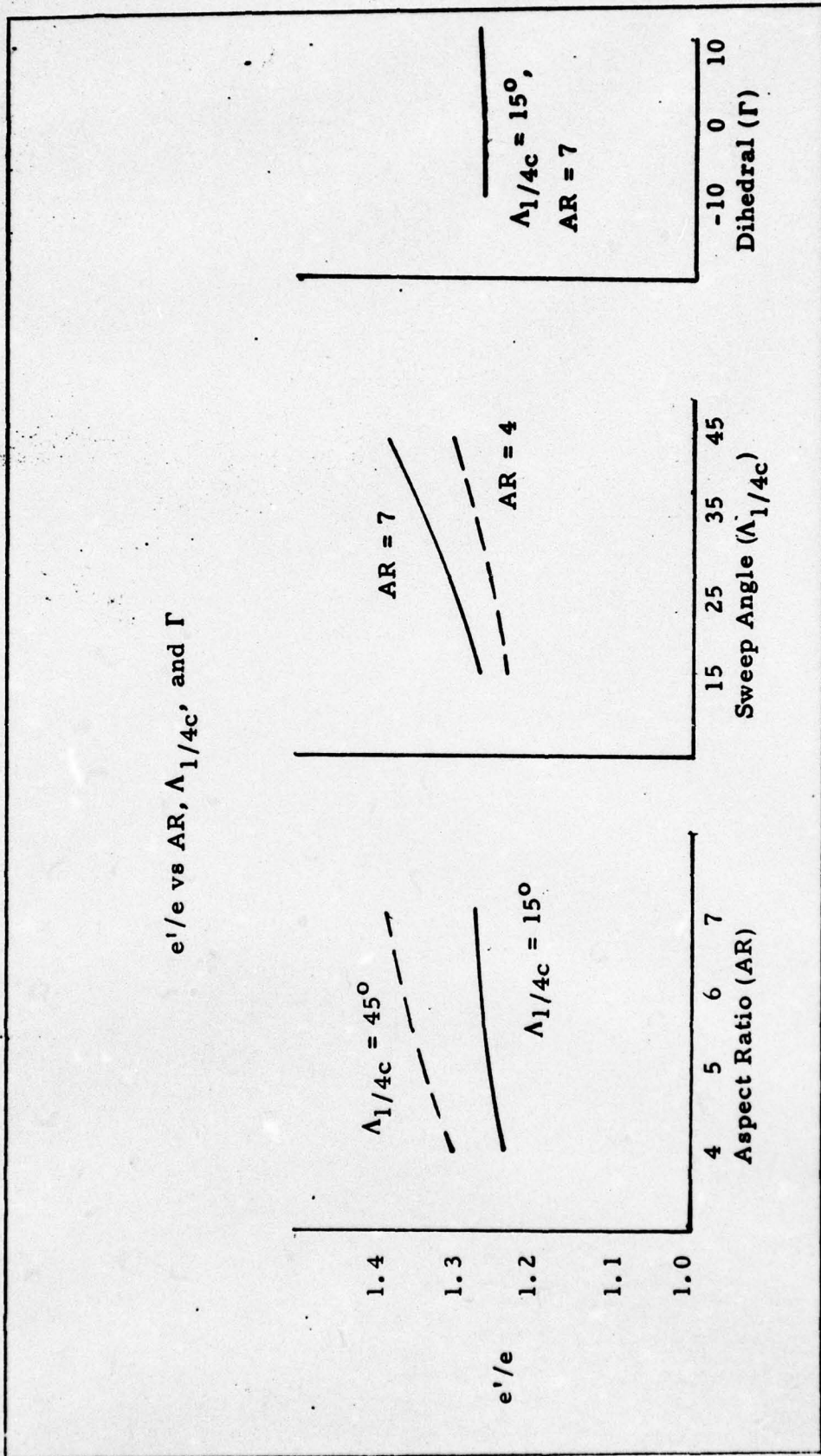


Fig. 19. Increase in Efficiency Factor vs Aspect Ratio, Sweep Angle and Dihedral

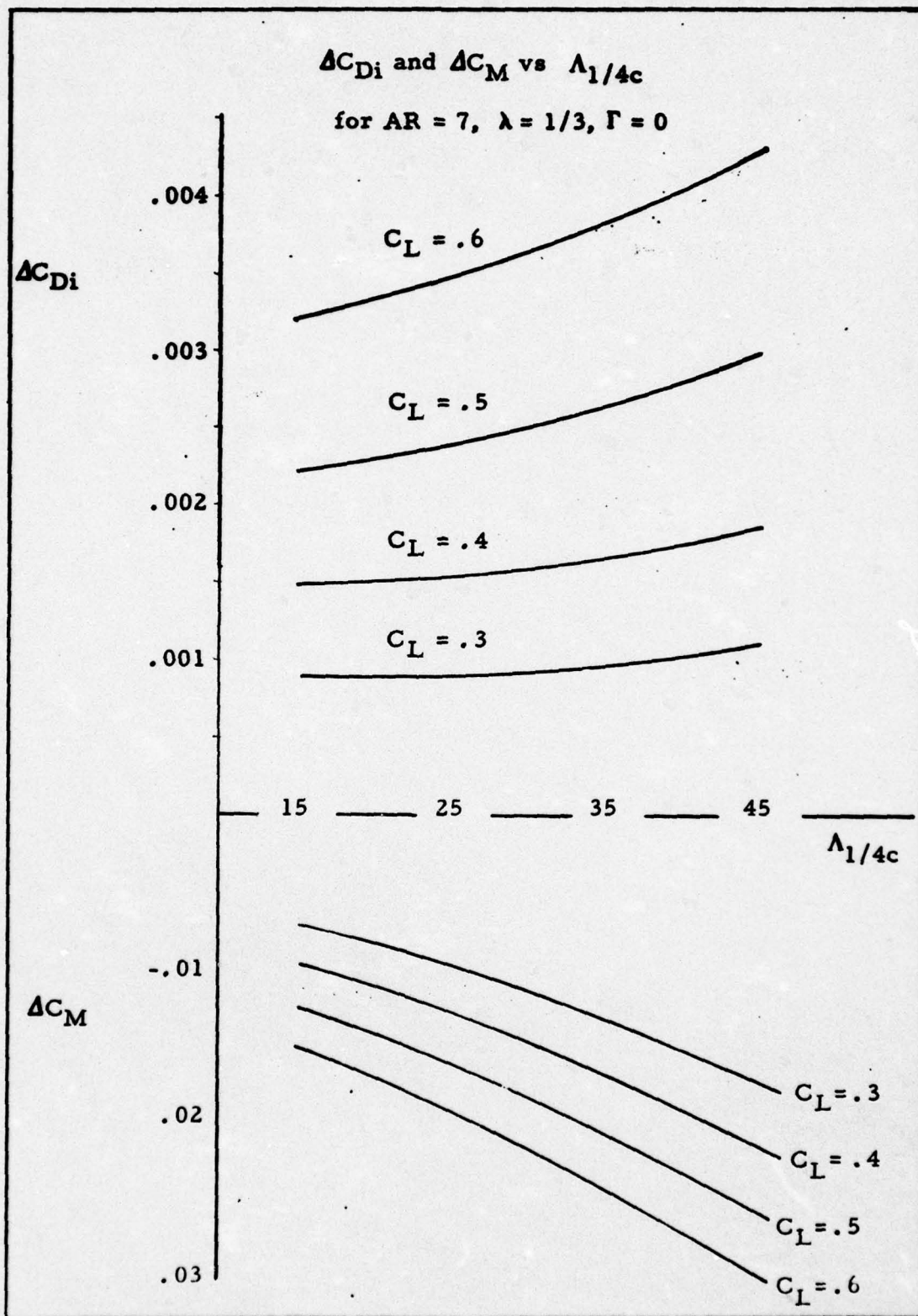


Fig. 20. Induced Drag Reduction and Pitching Moment Increase vs Wing Sweep Angle

that winglet effectiveness is greatest on higher swept wings. The magnitude of induced drag reduction, as well as the percentage, increases with increasing wing sweep angle. As wing sweep angle increases, the incremental change in pitching moment increases. This change is approximately linear with lift coefficient as would be expected from the linear moment curves in Appendix B.

Figure 21 illustrates the induced drag reduction and change in pitching moment coefficient as a function of aspect ratio. Again, the induced drag reduction is proportional to the square of lift coefficient, and  $\Delta C_M$  is linear with lift coefficient. This figure shows that the magnitude of the induced drag reduction decreases as the aspect ratio increases. Thus, while the percentage drag reduction is greater for higher aspect ratio wings, the magnitude of the drag reduction is greater for lower aspect ratio wings.

The results of varying the dihedral angle (Fig. 22) show that induced drag reduction improves slightly with increasing dihedral angle. This improvement is very slight as the angle is increased from  $0^\circ$  to  $10^\circ$  dihedral, much less than the increase from  $-10$  to  $0^\circ$  dihedral. This Figure indicates that winglets are more effective when used on wings with significant dihedral and this is consistent with Boeing's speculation on the increased winglet effectiveness on the KC-135 over the C-141 (Ref 4).

Again, accompanying this increased drag reduction is a negative increment in pitching moment.

While the emphasis should be placed primarily on the trends mentioned above, the actual magnitude of the drag reduction due to

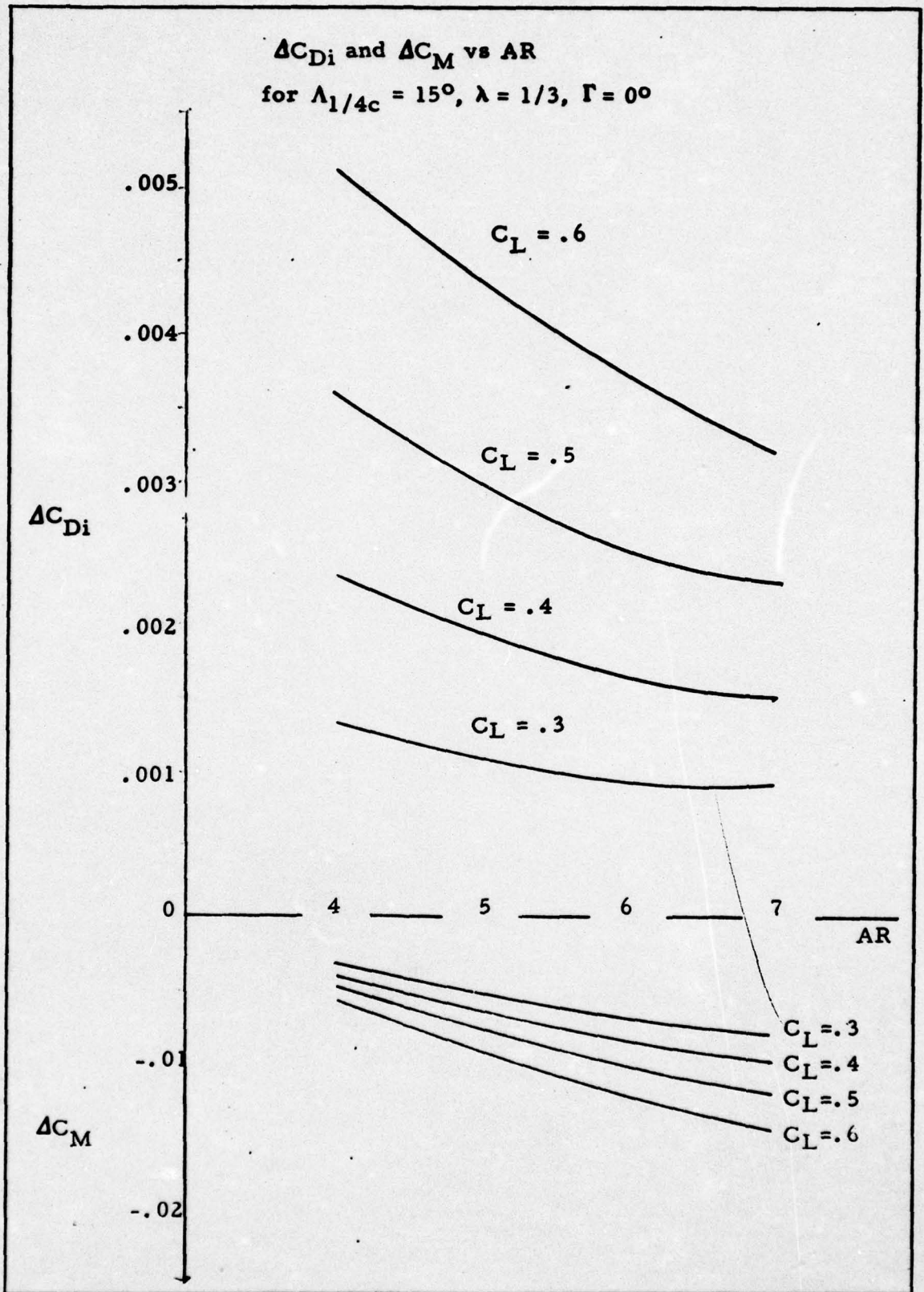


Fig. 21. Induced Drag Reduction and Pitching Moment Increase vs Wing Aspect Ratio

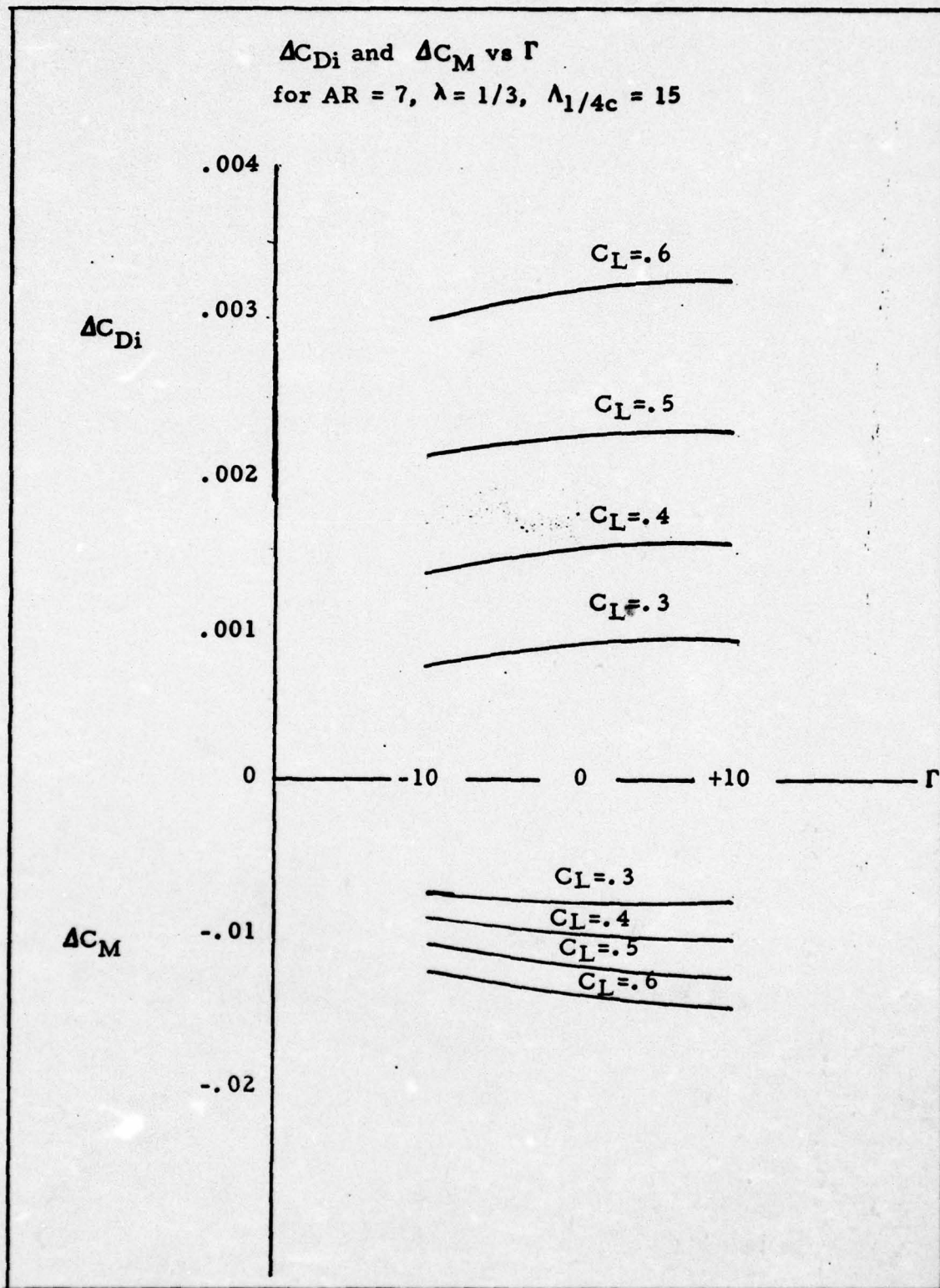


Fig. 22. Induced Drag Reduction and Pitching Moment Increase vs Wing Dihedral Angle

winglets is believed to be quite good. NASA wind tunnel tests on the KC-135 (AR = 7.035,  $\Lambda_{1/4c} = 35$  degrees,  $\lambda = .33$ ,  $\Gamma = 7$  degrees) show that the reduction in drag coefficient at Mach .7,  $C_L = .4$  is  $\Delta C_D = .0015$  (Ref 5:59). Figure 20 shows that for AR = 7,  $\Lambda_{1/4c} = 35$  degrees, and  $\lambda = 1/3$  the change in induced drag coefficient is  $\Delta C_{Di} = .00165$ . Figure 22 suggests that the effect of positive dihedral is to increase this figure slightly. It should be noted that the BAC 311 airfoil sections used in this study is one of the sections used in the KC-135. Although the value of drag reduction calculated in this study appears high, it represents only the change in induced drag. The change in total drag coefficient would be expected to be less due to increased viscous drag. The value calculated in this study represents a valid estimate of the expected induced drag reduction in this case.

#### Lateral Results

The effects of wing sweep, aspect ratio, and dihedral angle on the wing side force coefficient,  $C_Y$ , root bending moment coefficient  $C_R$ , and yawing moment coefficient,  $C_N$ , are shown in Figures 23-25. These coefficients were calculated for the right half of the configuration only. The total values for symmetric configurations are zero. For each wing, the addition of winglets increases the inward side force on the wing, increases the wing root bending moment, and decreases the yawing moment.

In Figure 23,  $\Delta C_Y$  is seen to increase as wing sweep angle increases, indicating greater inward loads are produced on higher swept wings.  $\Delta C_R$  is seen to decrease with increasing wing sweep indicating the outboard shift in loading is not as great on higher swept wings.  $\Delta C_N$  is caused

$\Delta C_Y$ ,  $\Delta C_R$ , and  $\Delta C_N$  vs  $\Lambda_{1/4c}$

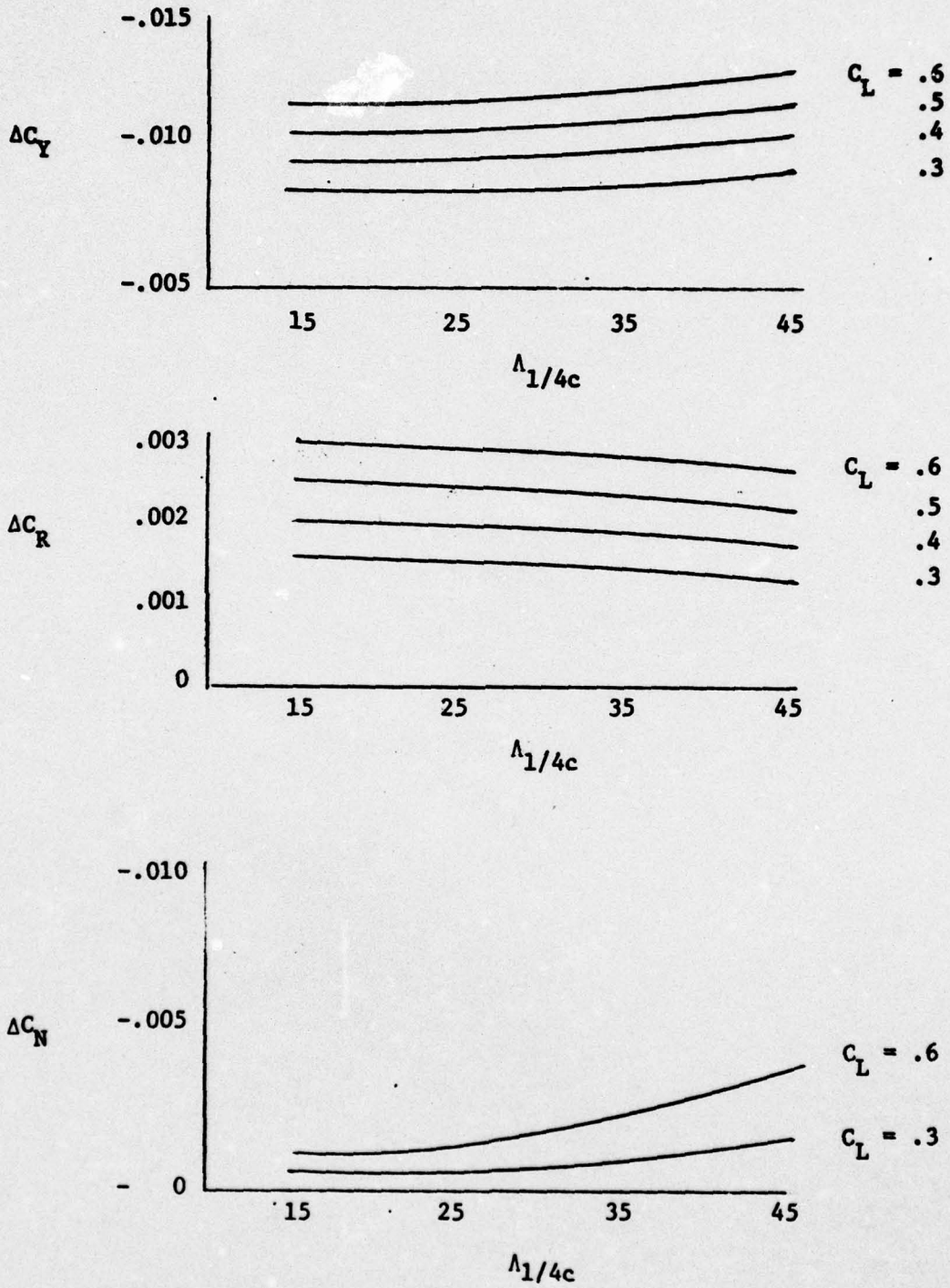


Fig. 23. Winglet Lateral Effects vs.  $\Lambda_{1/4c}$

$\Delta C_Y$ ,  $\Delta C_R$ , and  $\Delta C_N$  vs AR

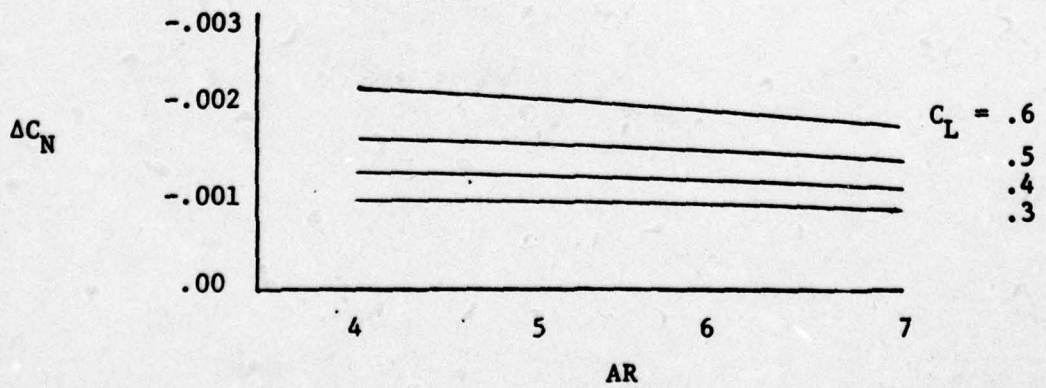
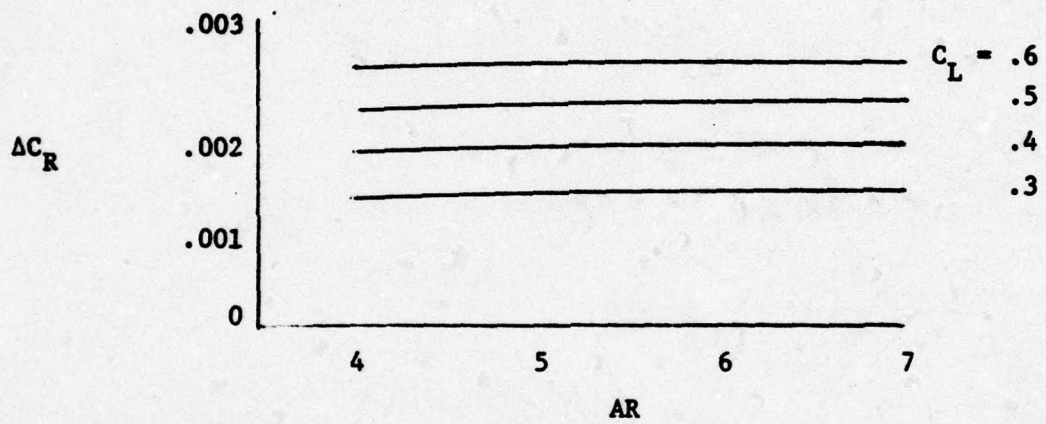
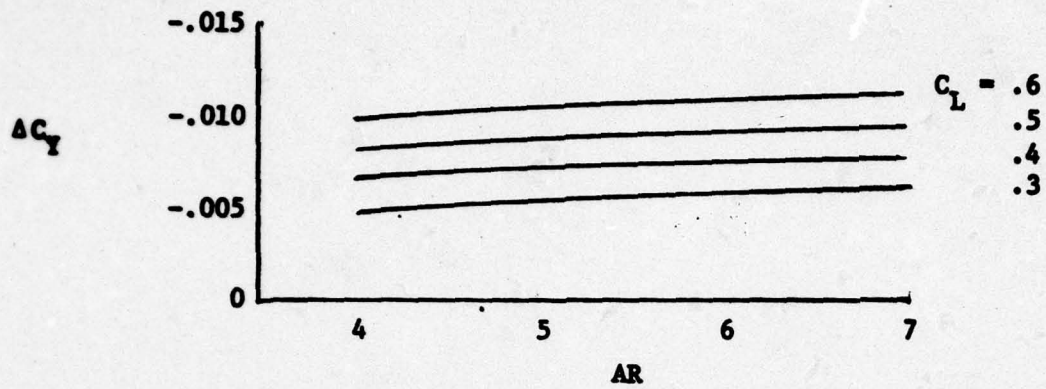


Fig. 24. Winglet Lateral Effects vs. AR

$\Delta C_Y, \Delta C_R, \text{ and } \Delta C_N \text{ vs } \Gamma$

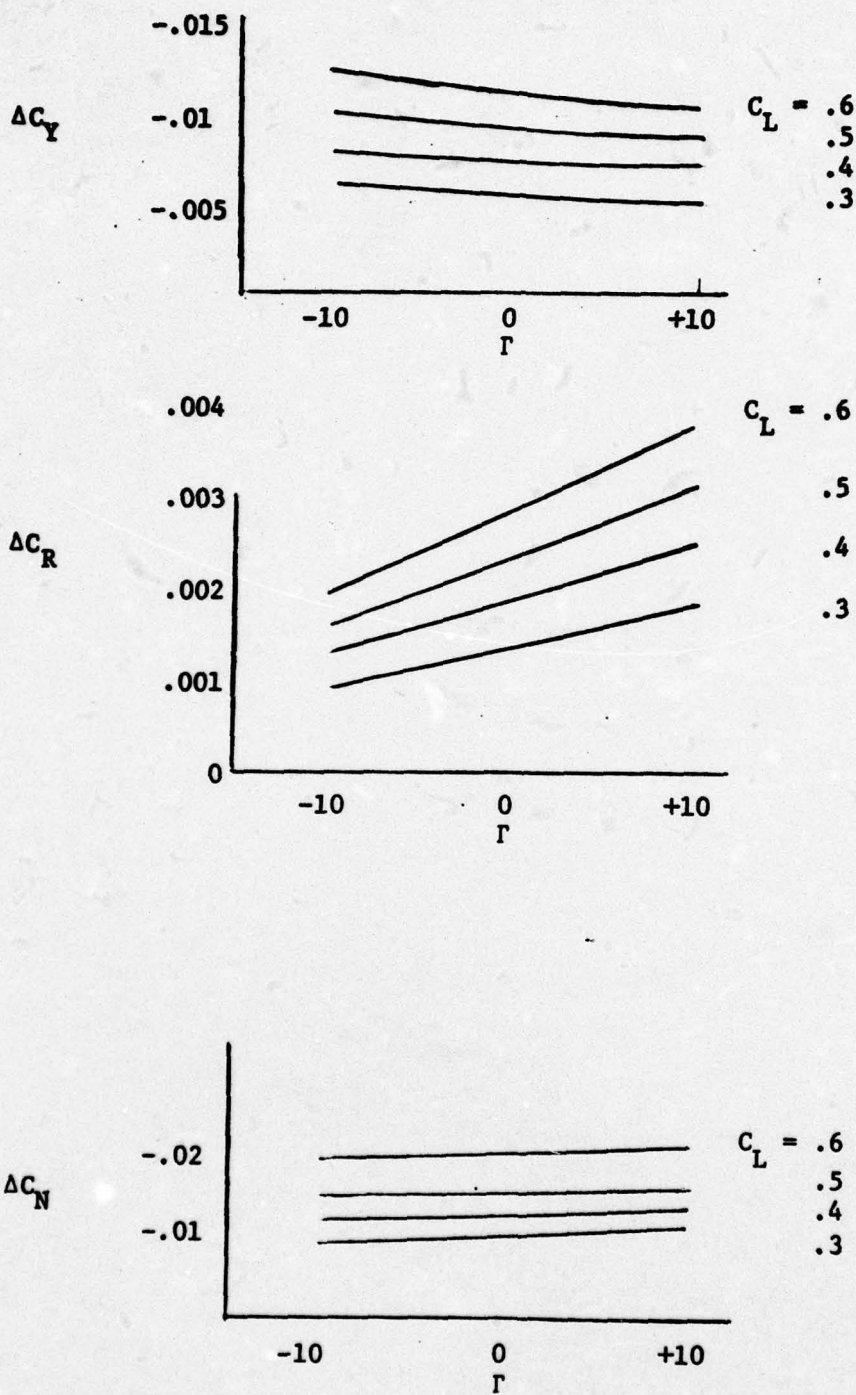


Fig. 25. Winglet Lateral Effects vs.  $\Gamma$

by the drag reduction and increases with increasing wing sweep.  $\Delta C_N$  is also proportional to  $C_L^2$  as is  $\Delta C_{D1}$ .

Figure 24 shows that  $\Delta C_Y$  increases with increasing aspect ratio. Although the inward force coefficient at the winglet is greater at low aspect ratios (greater lift-induced inflow), the ratio of winglet area to wing area increases as aspect ratio increases (wing area decreases). Thus, the effect of the winglet is greater at high aspect ratios.  $\Delta C_R$  increases with increasing aspect ratio for this same reason.  $\Delta C_N$  decreases as aspect ratio increases and  $\Delta C_{D1}$  decreases.

Figure 25 shows that  $\Delta C_Y$  is greatest on the wing with anhedral while  $\Delta C_R$  and  $\Delta C_N$  are greatest for the wing with dihedral. The significant change in  $\Delta C_R$  is due to the effective elevation of the winglet above the reference axis.

#### Winglet Cant Angle

Appendix C contains comparisons of aerodynamic data for both wings with  $\pm 3$  degrees winglet incidence. For both wings the +3 degree cant angle yields the larger increase in  $C_L$ . Examination of the drag polars shows that for both wings the +3 degree cant angle gives the lower induced drag over the greatest range of lift coefficients. Since the goal of winglet addition is the reduction of drag at cruise conditions ( $C_L \approx .4$ ), it appears as though the positive cant angle would be the better choice. NASA wind tunnel results indicate the optimum winglet cant angle is significantly less than that predicted by the theory used here. This difference is due to viscous effects not considered in this model.

### Winglet Penalties

In addition to the desired effect of winglets, the reduction of drag, there are certain penalties that must be accounted for. The addition of winglets adds profile and skin friction drag which were not accounted for in this analysis. The weight of the winglets and structural modifications requires that the wing develop increased lift. Initial Boeing estimates indicate that the addition of winglets to the KC-135 will add approximately 600 pounds to the aircraft basic weight (Ref 4:51). There is also a trim penalty due to the nose down pitching moment increase and a possible structural penalty due to the increased wing root bending moment. These effects will be examined separately.

### Trim Effects

Not only do winglets reduce the induced drag on a wing, they increase the nose down pitching moment which in turn must be balanced by a reduction in lift on the horizontal tail. To evaluate this trim penalty on a typical aircraft, the following conditions were assumed

$$\begin{array}{ll} h = 30,000 \text{ ft} & M = .7 \\ b = 100 \text{ ft} & AR = 7 \\ \bar{c} = 21.43 \text{ ft} & S = 1428.6 \text{ ft}^2 \\ W = 130,000 \text{ lbs} & C_L = .4 \\ \Lambda_{1/4c} = 35 & \bar{q} = 227.8 \text{ lbf/ft}^2 \end{array}$$

This aircraft is approximately equal in size, weight, and characteristics to the Boeing 727. From Figure B-3 it is found that the addition of

winglets reduces the induced drag coefficient by .0018. The static margin is assumed negligible in comparison with the distance between the center of gravity and the tail aerodynamic center,  $x_t$ . By summing moments about the center of gravity, the increased lift coefficient required on the main wing is found to be

$$\Delta C_L = \bar{c} \Delta C_M / x_t \quad (12)$$

For this hypothetical aircraft,  $x_t = 60$  ft. From Figure B-29, the change in pitching moment is .0175. Therefore,

$$\Delta C_L = .36 \Delta C_M \quad (13)$$

and the required lift coefficient would now be  $C_L = .406$ . This in turn lessens the previous induced drag reduction. The effect, however, is very slight.

#### Structural Weight Increase

At the same flight condition examined above, Fig. B-38 shows that the wing root bending moment coefficient is increased from .043 to .045, a 4.7% increase. This increase may require an increase in structural weight, particularly in the outboard regions of the wing.

As a rough approximation of the weight increase required, it is assumed that

$$\frac{\Delta t}{t} = \frac{\Delta C_R}{C_R} \quad (14)$$

or that the structural skin must be thickened by the percentage increase in root bending moment. If it is assumed that the structural box is approximately .4 c in length, then the total area to be thickened is .8 S.

Assuming the original material is 1/4 inch aluminum, then

$$\Delta W = \rho .8 S t \frac{\Delta C_R}{C_R} \quad (15)$$

In this example, the weight increase is 189 pounds.

## V. Conclusions and Recommendations

### Wing Parameter Study

In the preceding chapter, it was pointed out that the induced drag reduction resulting from winglet addition was greatest for wings with high wing sweep, low aspect ratio, and positive dihedral.

The percentage reduction in induced drag was greatest for high aspect ratio, and positive dihedral wings.

Accompanying the reduction in induced drag in each case was a negative increment in pitching moment and an increase in the wing root bending moment. Both of these moment increments negate some of the induced drag reduction, but the effects of each were very slight. Induced drag reductions in the range of 15% to 25% appear possible for the wings considered in this study. A limitation of this result was the inability of the model to predict viscous and aeroelastic effects.

This study has indicated that significant drag reductions are possible on wings other than the transport wings studied to date. The curves shown in the previous chapter may be used as a first approximation to the induced drag reduction possible for a variety of wings.

### Winglet Cant Angle Study

The variation of winglet cant angle in this study indicates that positive cant angles produce the larger inward side forces on the winglets and offer better drag reduction over the greater range of lift coefficients. This increased loading, however, may be undesirable. It should be noted that the results of this theoretical analysis do not agree with the NASA theory and experimental results which included viscous effects not considered here.

### Recommendations

Although the NPLS theory and method of calculating aerodynamic coefficients are very useful and have yielded useful results, the calculations are only theoretical predictions and should be considered as such. Future investigations should couple wind tunnel results with theoretical predictions. Future investigations to experimentally find an optimum winglet cant angle would be very beneficial.

### Bibliography

1. Klineberg, J. M., Kramer, J. J., and Povinelli, F. P. "Improving Aircraft Energy Efficiency", Astronautics and Aeronautics. 14:18-31 (February 1976).
2. Jacobs, Peter F., and Flechner, Stuart G. The Effect of Winglets on the Static Aerodynamic Stability of a Representative Second Generation Jet Transport Wing. NASA TN D-8267, Washington: National Aeronautics and Space Administration, July 1976.
3. Whitcomb, Richard T. A Design Approach and Selected Wind-Tunnel Results at High Subsonic Speed for Wing-Tip Mounted Winglets. NASA TN D-8260, Washington: National Aeronautics and Space Administration, July 1976.
4. Ishimitsu, K. K. Design and Analysis of Winglets for Military Aircraft. Seattle: Boeing Commercial Airplane Company, February 1976.
5. Goldhammer, M. I. A Nonplanar Lifting Systems Method. Long Beach, California: McDonnell Douglas Corporation, January 1976.
6. \_\_\_\_\_. A Lifting Surface Theory for the Analysis of Nonplanar Lifting Systems. AIAA Paper No. 76-16, Washington: American Institute of Astronautics and Aeronautics, January 1976.
7. Riley, D. R. Wind Tunnel Investigation and Analysis of the Effects of End Plates on the Aerodynamic Characteristics of an Unswept Wing. NASA TN 2440, Washington: National Aeronautics and Space Administration, August 1951.
8. Roskam, Jan. Flight Dynamics of Rigid and Elastic Airplanes. Lawrence, Kansas: Roskam Aviation and Engineering Corporation, 1972.
9. Karamchetti, Krishnamurty. Principles of Ideal-Fluid Aerodynamics. New York: John Wiley and Sons, 1966.

## Appendix A

### Nonplanar Lifting Systems Theory

A new nonplanar lifting surface theory was developed by Mr. M. I. Goldhammer of Douglas Aircraft Company. This method represents nonplanar lifting systems by distributed vorticity. It has been used to compute the induced drag benefit of winglets and the agreement with NASA experimental data is excellent (Ref 5).

The Nonplanar Lifting Systems (NPLS) Method is a nonlinear, nonplanar, lifting surface theory; wing thickness effects are neglected. This theory makes no small perturbation assumptions as do previous lifting surface theories.

The basic problem is to determine aerodynamic forces and moments on an arbitrary three dimensional lifting system. The system is assumed to be placed in a uniform, inviscid, incompressible, irrotational flow. This method is restricted to the analyses of wing-like bodies only. Fuselages, nacelles, and other non-lifting bodies are excluded.

The primary assumption in this theory is that thickness effects are small and can be neglected. Experience has shown that thin wing theories give good solutions in terms of sectional and total aerodynamic forces and moments. It is also assumed that the trailing vortex does not bend aft of the trailing edge. Finally, it is assumed that the entire flow field is subcritical.

With these assumptions, the problem can be treated using potential flow techniques and the solution is governed by Laplace's equation

$$\Delta^2 \phi = 0 \quad (A-1)$$

This equation must be solved subject to boundary conditions which specify that the flow be tangent at all points on the surfaces and that there be no disturbance infinitely far from the body.

$$[(U_{\infty} + u) \vec{i} + v \vec{j} + (W_{\infty} + w) \vec{k}] \cdot \vec{n} = 0$$

or

$$\Delta(\phi_{\infty} + \phi) = 0$$

(A-2)

on the body and,

$$\phi \rightarrow 0$$

(A-3)

infinitely far from the body.

In Eq (A-1)  $\phi$  represents the potential function. In Eq (2), (u, v, w) are the perturbation velocity components.  $\phi$  represents the perturbation velocity potential.  $U_{\infty}$ ,  $W_{\infty}$ , and  $\phi_{\infty}$  are the corresponding free stream quantities and  $\vec{n}$  is the unit normal vector on the surface.

The solution of Eq (A-1) subject to the boundary conditions, Eqs (A-2 and A-3), is obtained by application of Green's Theorem to determine  $\phi$  (Ref 5).

$$\phi(x, y, z) = \frac{1}{4\pi} \oint_S \left[ \phi \frac{\partial}{\partial n} - \frac{\partial \phi}{\partial n} \right] \frac{ds}{\sqrt{(x-\xi)^2 + (y-\eta)^2 + (z-\zeta)^2}}$$

(A-4)

In Eq (A-4) the region S is the surface of the body and  $(\xi, \eta, \zeta)$  are dummy (x, y, z) variables on the surface.

To integrate the resulting induced velocity equations, (Ref 6:3), three simplifying assumptions are made. By allowing each finite element to be planar the integration can be accomplished in a local coordinate

system. Second, it is assumed that  $\gamma$ , the vortex strength, does not vary spanwise. This requires a finer finite element mesh where large changes in spanwise loading occur. Third, finite elements are rectangular. An Elementary Vortex Distribution technique assigns a functional form to the chordwise vorticity distribution over each finite element. Thus, the vorticity,  $\gamma$ , in the induced flow equations can be replaced by an unknown vortex strength,  $\gamma'$ , times a function of only geometric parameters. The integrands of these equations now contain only geometric parameters since the vortex strength,  $\gamma'$ , can be taken outside the integrals. The induced flow can be expressed as

$$\vec{q} = \gamma' (A_u \vec{i} + A_v \vec{j} + A_w \vec{k}) + U \quad (A-5)$$

where A's are influence functions. The finite element solution can now be formulated.

Velocities induced by all finite elements are summed at each boundary condition point. The vortex strength,  $\gamma'$ , is then adjusted until the normal velocity at each point is zero.

#### Elementary Vortex Distribution

The Elementary Vortex Distribution technique assigns a functional form to the vorticity distribution on each element. Thin airfoil theory (Ref 9) shows that the vorticity distribution on a flat plate airfoil is of the form

$$\gamma(\xi) = \frac{1}{\sqrt{\xi/c (1-\xi/c)}} \quad (A-6)$$

At the leading edge ( $\xi \rightarrow 0$ ) the function behaves as  $1/\sqrt{\xi}$ .  $1/\sqrt{\xi}$ , then, appears to be a good choice for the leading edge element.

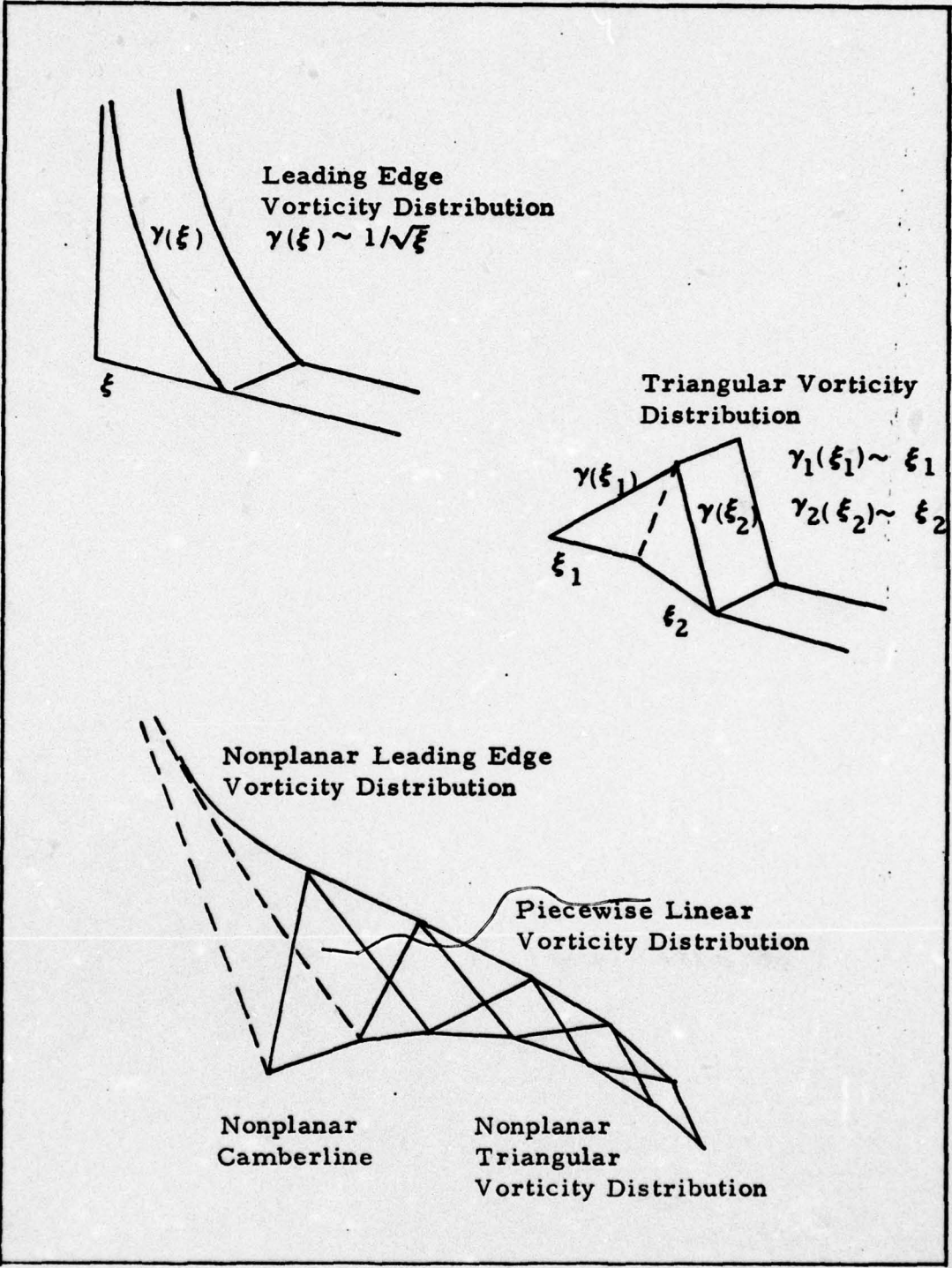


Fig. A-1. Representation of Wing Loading

The actual form used in the present method is

$$\gamma(\xi) = \frac{2}{3} \gamma' [(\xi/\delta)^{1/2} - (\xi/\delta)], \quad 0 \leq \xi \leq \delta \quad (\text{A-7})$$

The factor of 2/3 allows  $\gamma'$  to represent the mean value of  $\gamma$  over the interval. The leading edge EVD is shown in Fig. A-1.

Aft of the leading edge element,  $\gamma$  is represented by a trapezoidal vorticity distribution which results from the superposition of triangular distributions.

$$\gamma(s) = \begin{cases} \gamma'/\delta_1 (\xi_1 + \delta_1) - \delta_1 \leq \xi_1 \leq 0 \\ -\gamma'/\delta_2 (\xi_2 - \delta_2) \quad 0 \leq \xi_2 \leq \delta_2 \end{cases} \quad (\text{A-8})$$

This distribution is also illustrated in Fig. A-1.

It should be noted that this distribution does satisfy the Kutta condition that flow leave the trailing edge tangential to the camberline and there be no loading at the trailing edge.

#### Calculation of Forces and Moments

After the values of the influence functions have been obtained, it is necessary to calculate surface pressures, forces, and moments. The basic relation used to compute the pressure jump across the lifting surface is the Kutta-Joukowski Law. It states that the force per unit length on a vortex in a flow field is proportional to the fluid density times the vortex strength times the velocity. Aerodynamic forces and moments are computed by integrating the pressure jump coefficients over the lifting surfaces. Although the flow field was initially assumed to be incompressible, the program allows for corrections based on the Prandtl - Glauert transformation to include compressibility effects.

Appendix B

Aerodynamic Data for Wing Parameter Study

This Appendix contains plots of the aerodynamic coefficients calculated for the wing parameter study using the NPLS Computer Program.

The following figures show comparisons of aerodynamic data for the wing alone with that for the wing-winglet combination. All wings were constructed using a Boeing BAC 311 airfoil and had a taper ratio of 1/3. The winglets used were described on page and were mounted at 0 degrees cant angle and 70 degrees dihedral angle.

The aerodynamic data presented was calculated for the following wings:

Wing #	$\Lambda_{1/4c} =$	AR =	$\Gamma =$
2	25	7	0
3	35	7	0
4	45	7	0
5	15	6	0
6	15	5	0
7	15	4	0
8	45	4	0
9	15	7	+10
10	15	7	-10

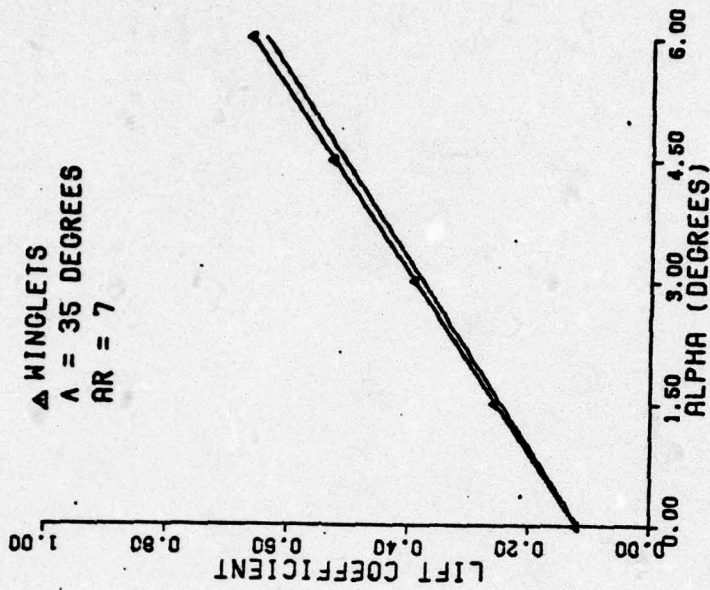


Fig. B-2. Wing #3 Lift Curves

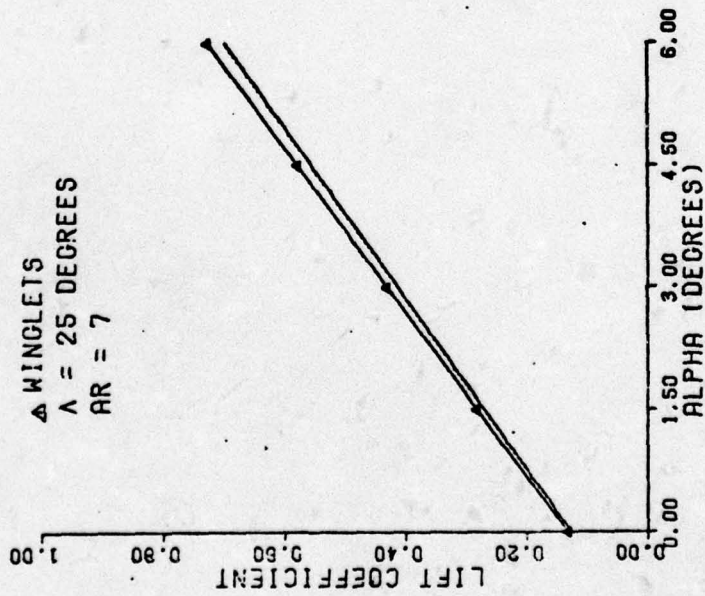


Fig. B-1. Wing #2 Lift Curves

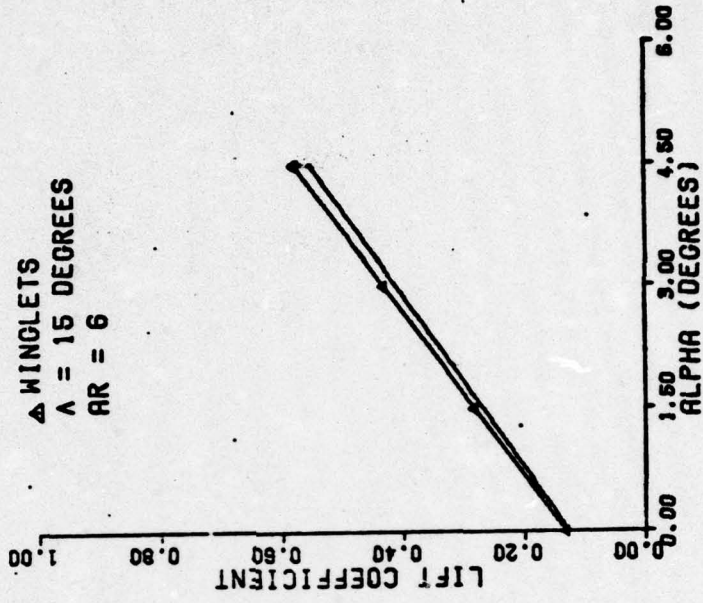


Fig. B-4. Wing #5 Lift Curves

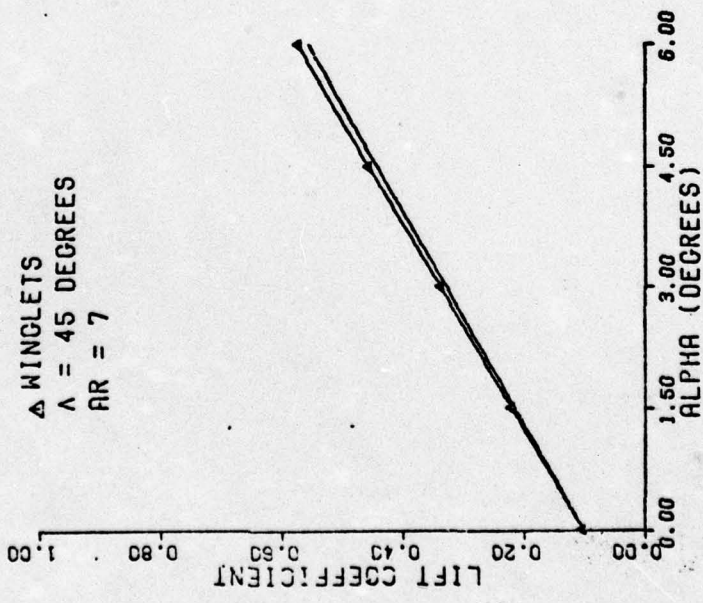


Fig. B-3. Wing #4 Lift Curves

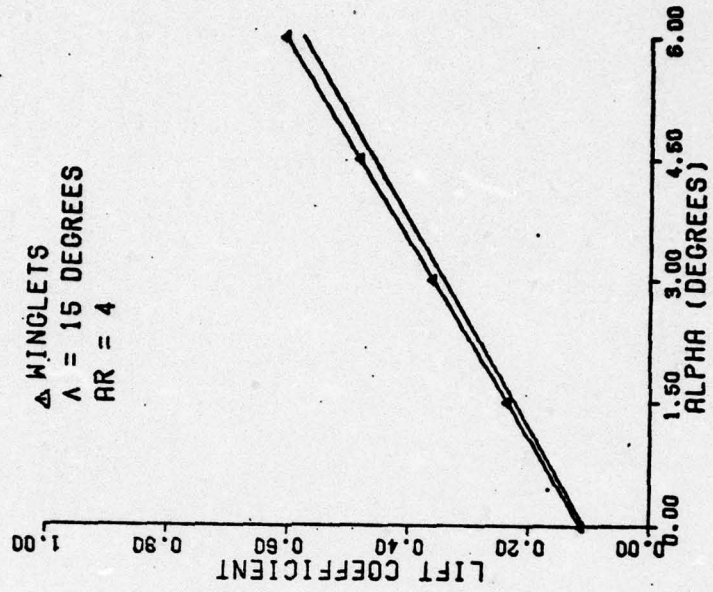


Fig. B-6. Wing #7 Lift Curves

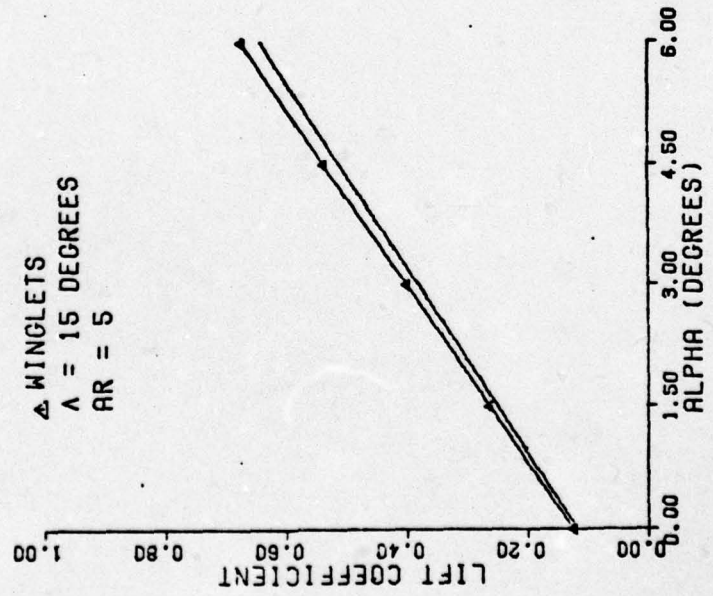


Fig. B-5. Wing #6 Lift Curves

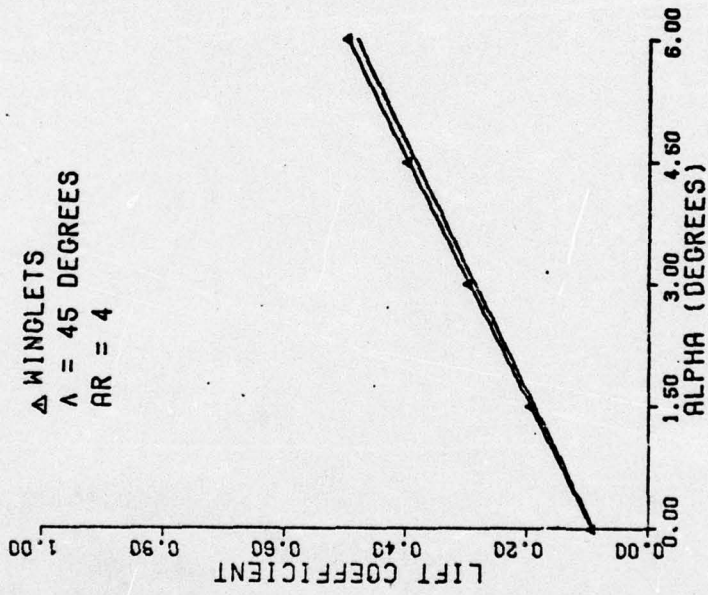


Fig.-B-7. Wing #8 Lift Curves

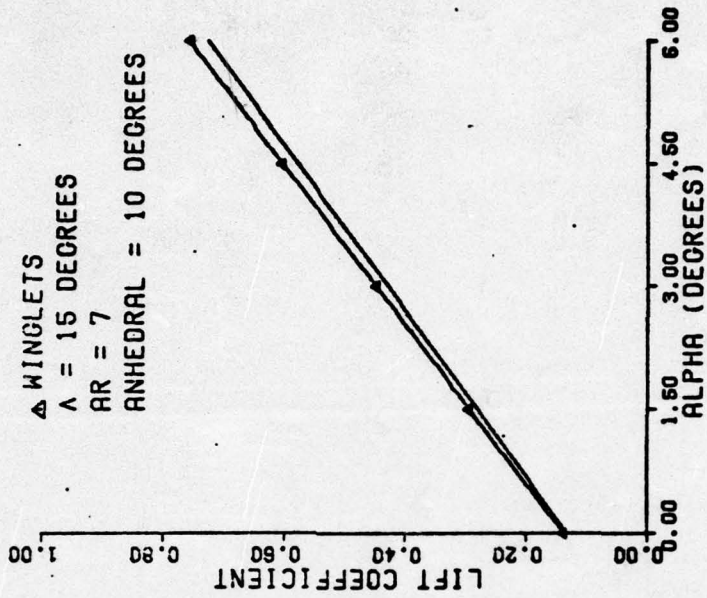


Fig. B-9. Wing #10 Lift Curves

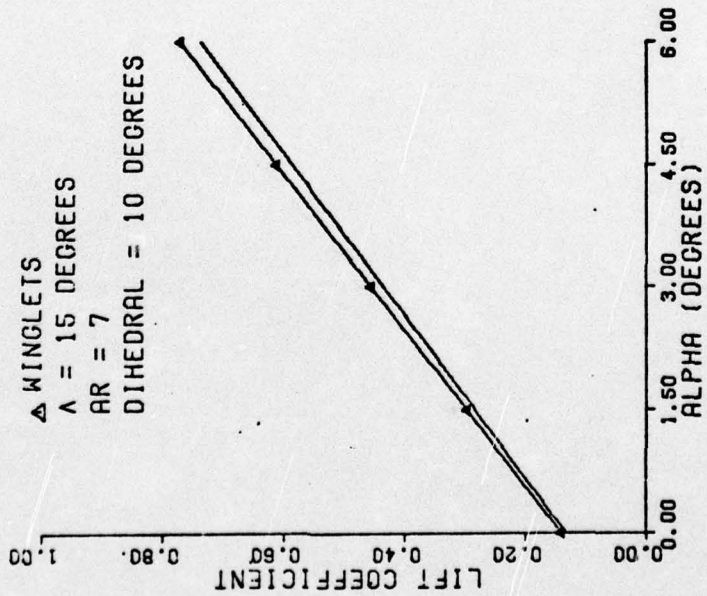


Fig. B-8. Wing #9 Lift Curves

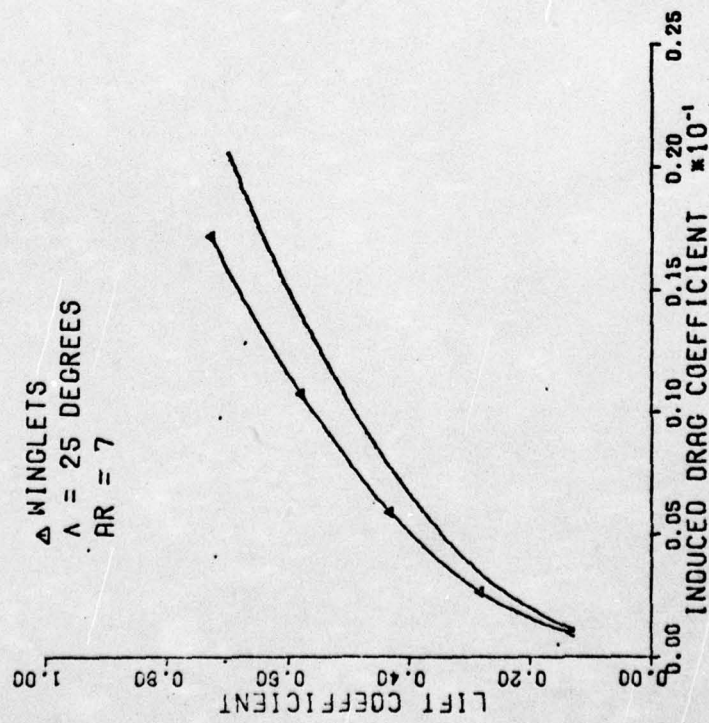


Fig. B-10. Wing #2 Drag Polars

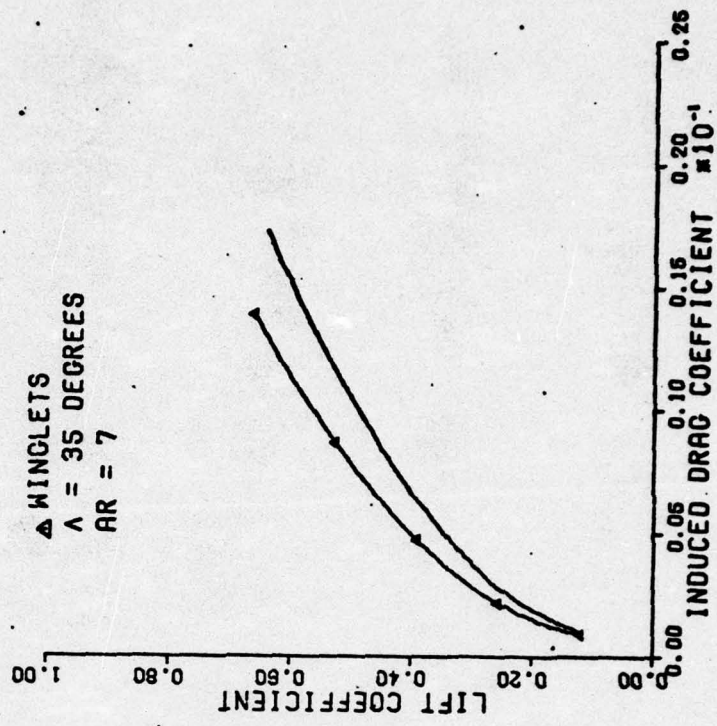


Fig. B-11. Wing #3 Drag Polars

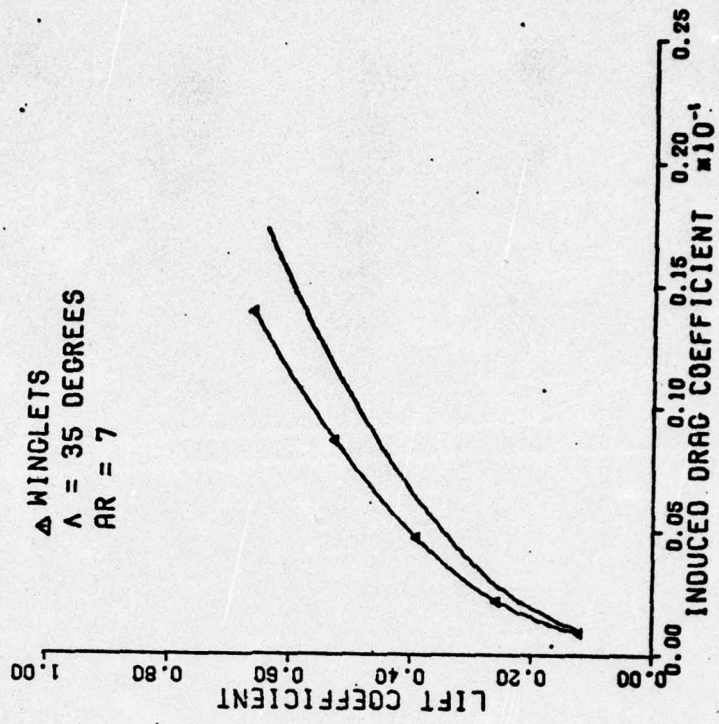


Fig. B-11. Wing #3 Drag Polars

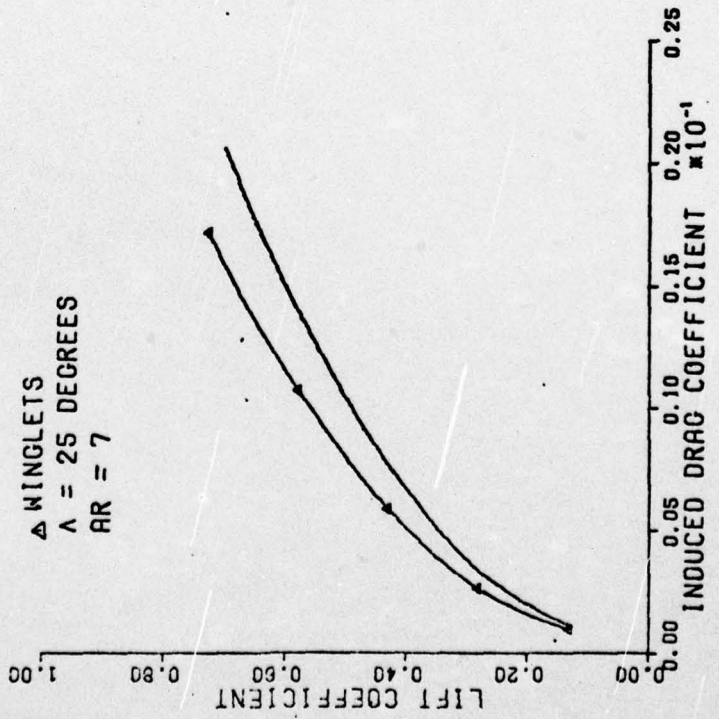


Fig. B-10. Wing #2 Drag Polars

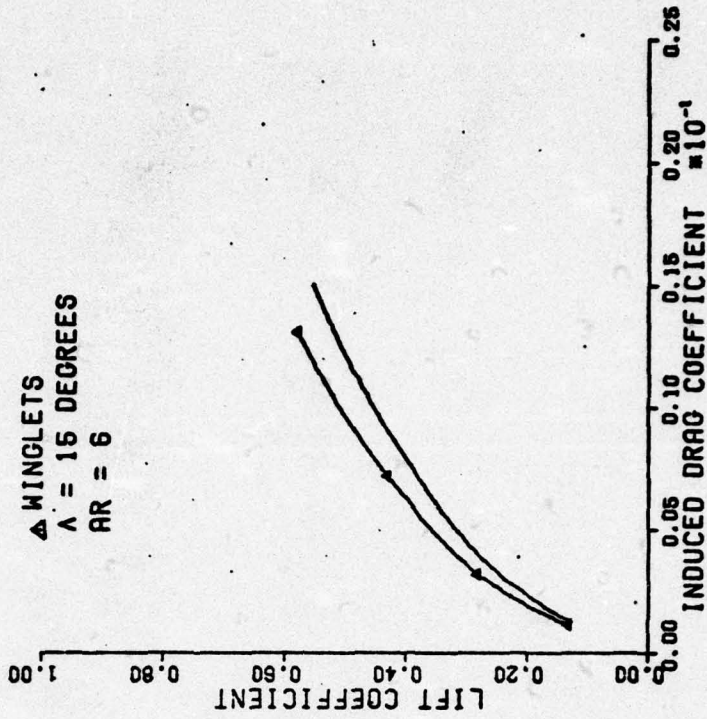


Fig. B-13. Wing #5 Drag Polars

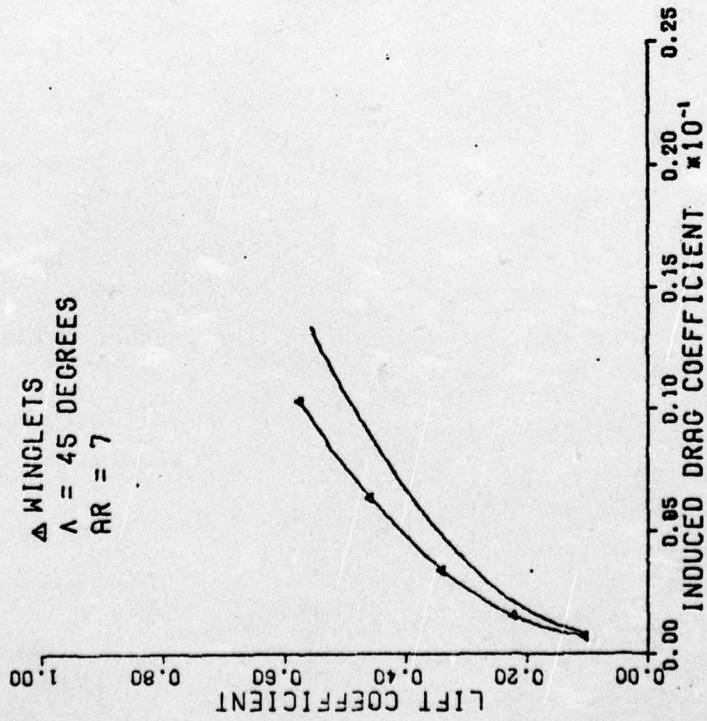


Fig. B-12. Wing #4 Drag Polars

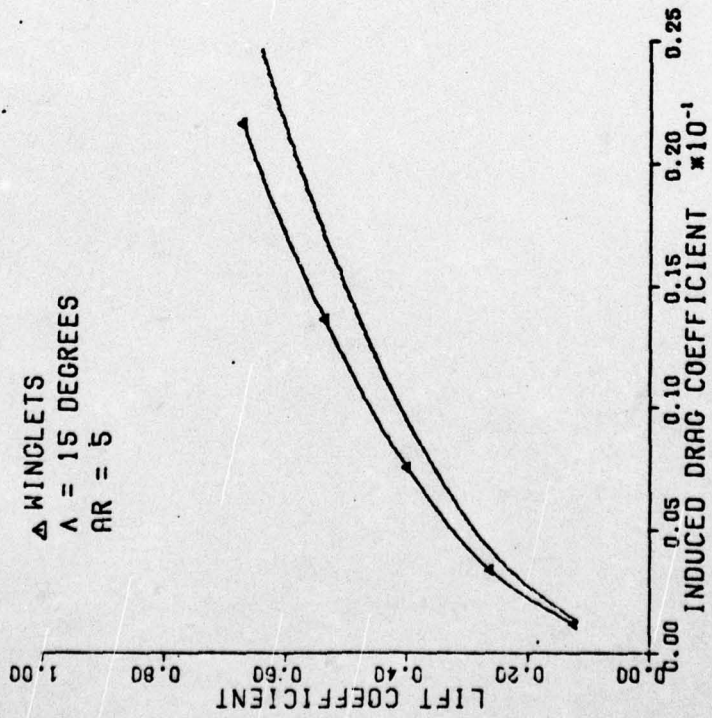


Fig. B-14. Wing #6 Drag Polars

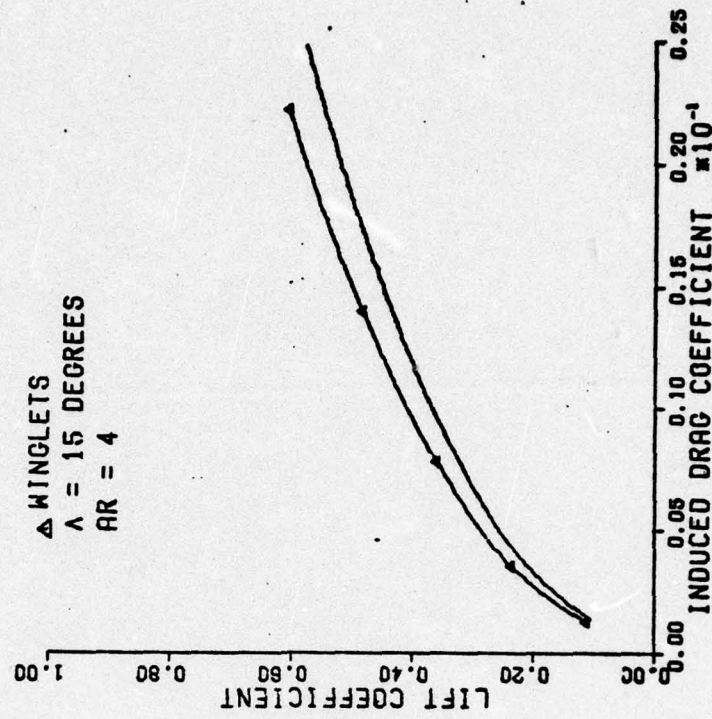


Fig. B-15. Wing #7 Drag Polars

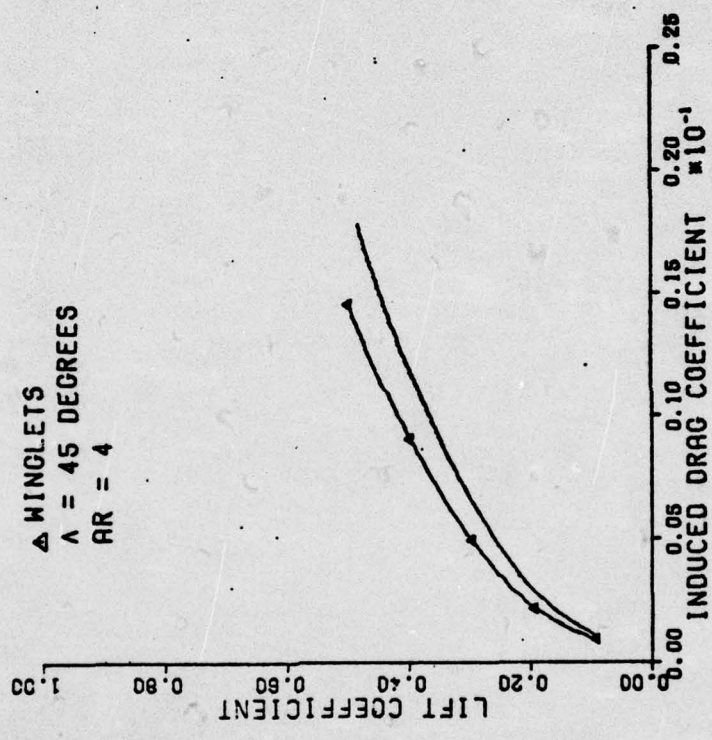


Fig. D-16. Wing #8 Drag Polars

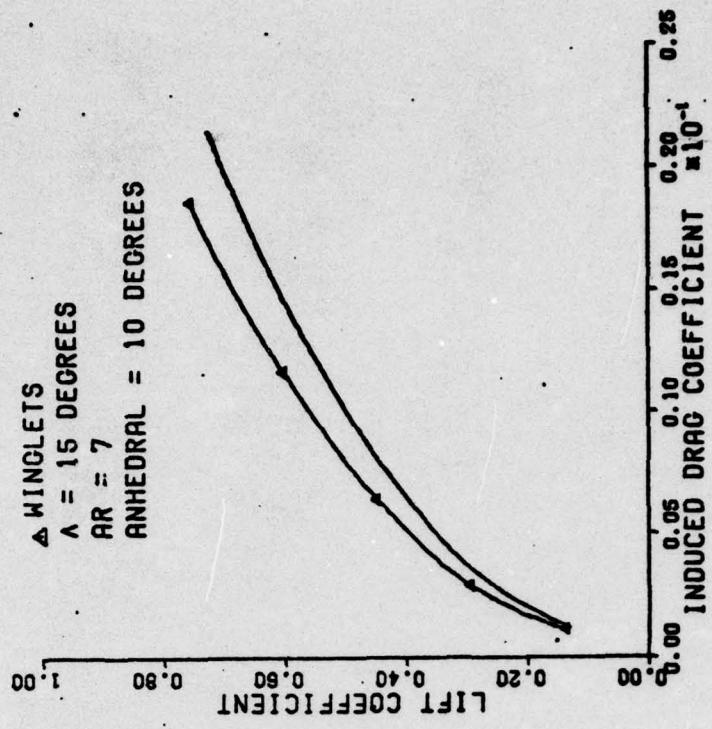


Fig. B-16. Wing #10 Drag Polars

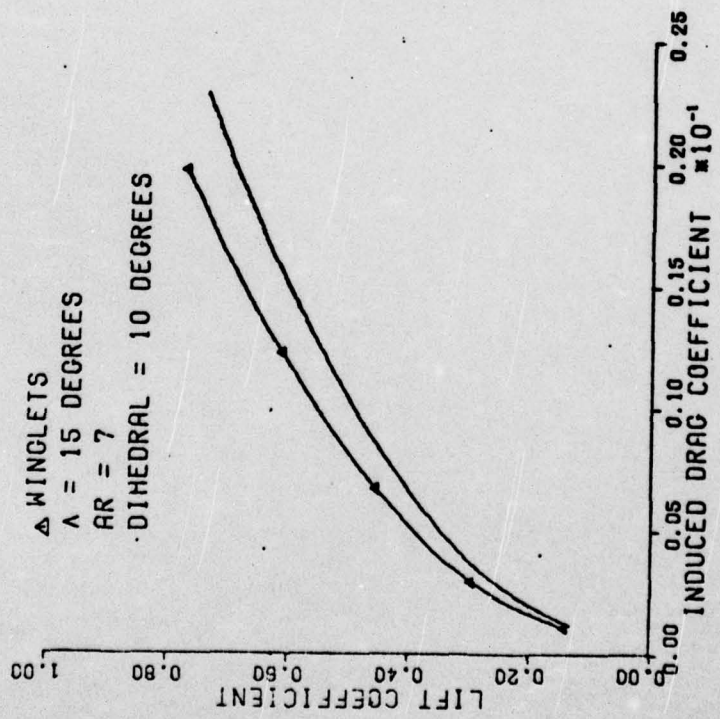


Fig. B-17. Wing #9 Drag Polars

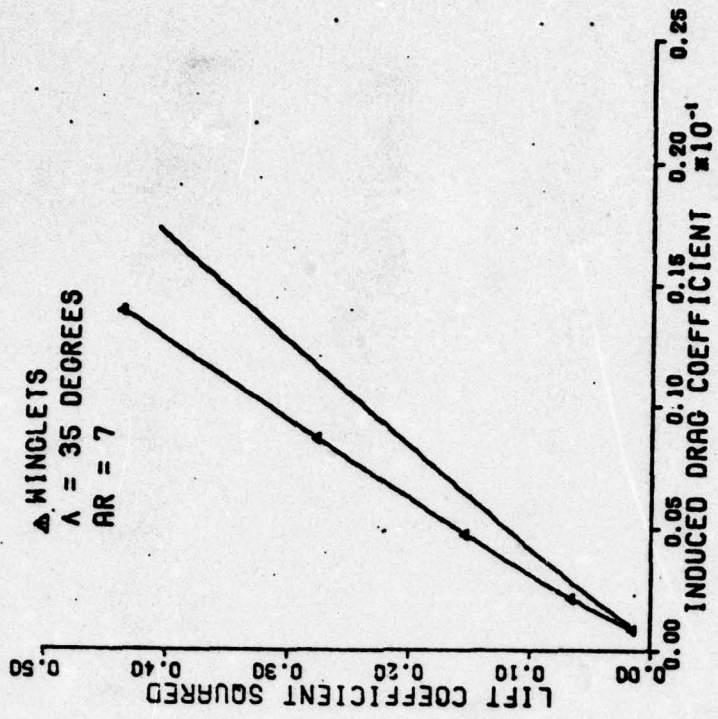


Fig. B-20.  $C_L^2$  vs  $C_{Di}$  for Wing #3

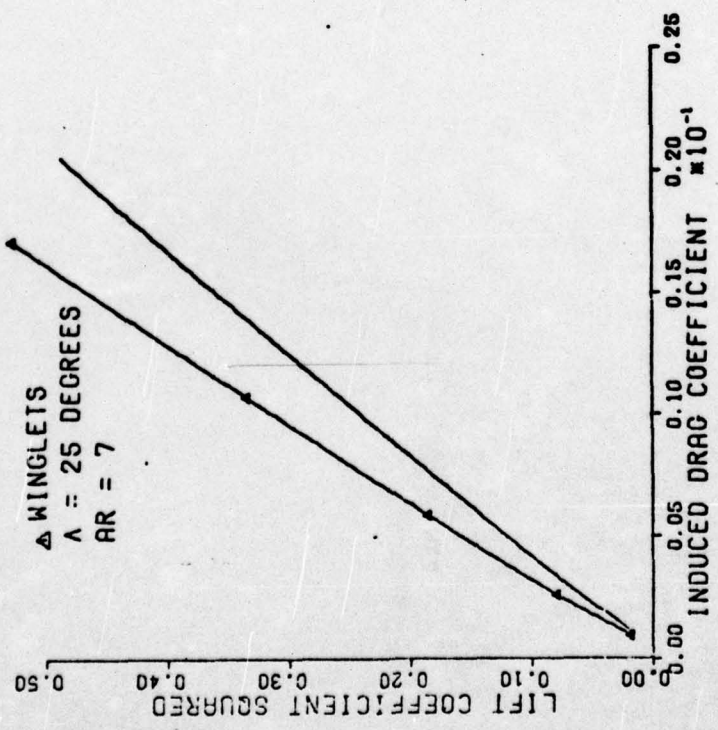


Fig. B-19.  $C_L^2$  vs  $C_{Di}$  for Wing #2

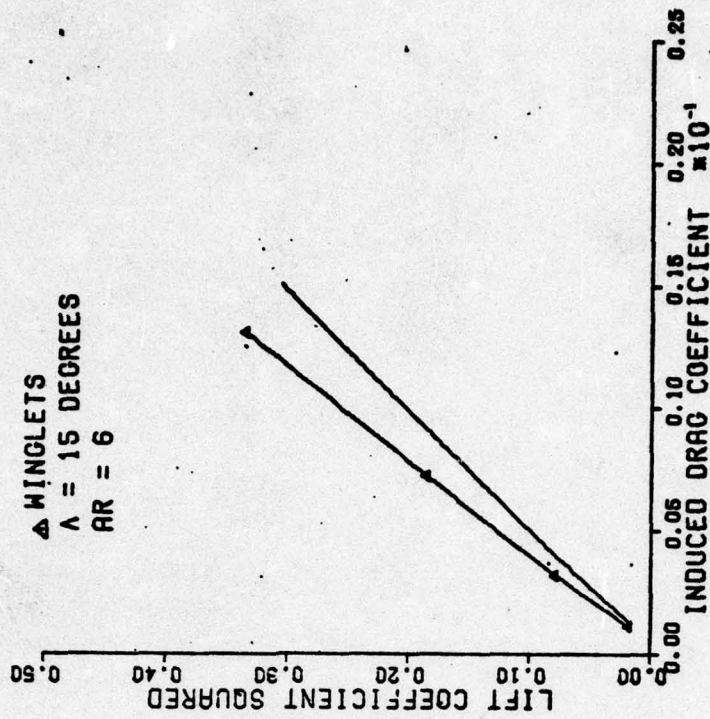


Fig. B-22.  $C_L^2$  vs  $C_{Di}$  for Wing #5

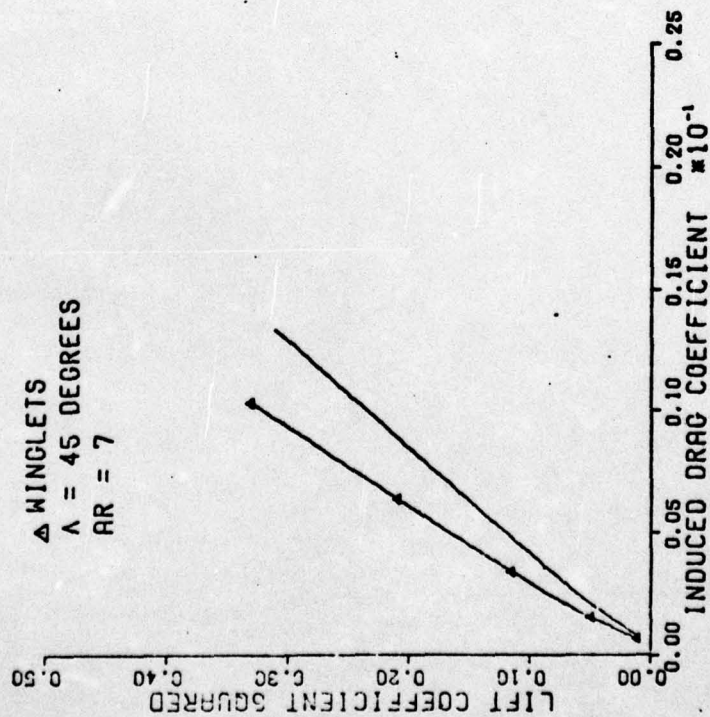


Fig. B-21.  $C_L^2$  vs  $C_{Di}$  for Wing #4

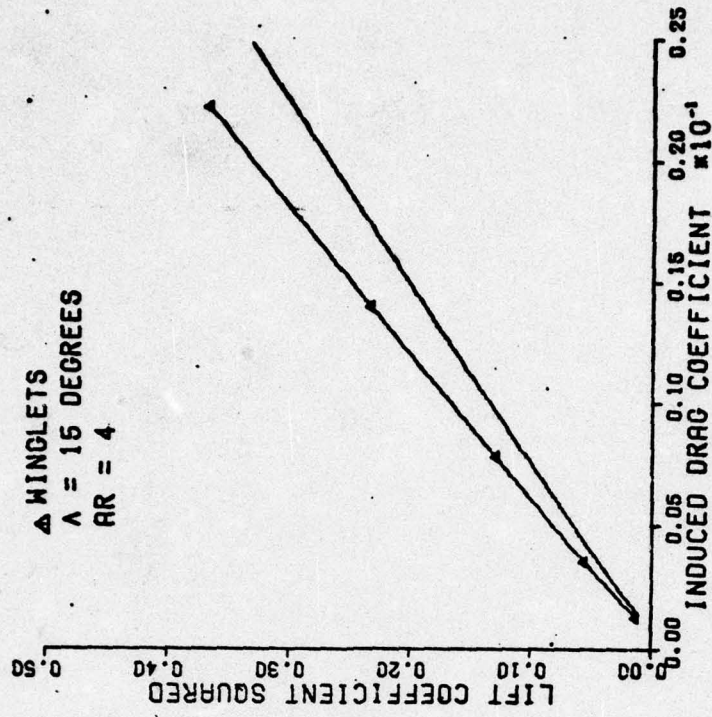


Fig. B-24.  $C_L^2$  vs  $C_{Di}$  for Wing #7

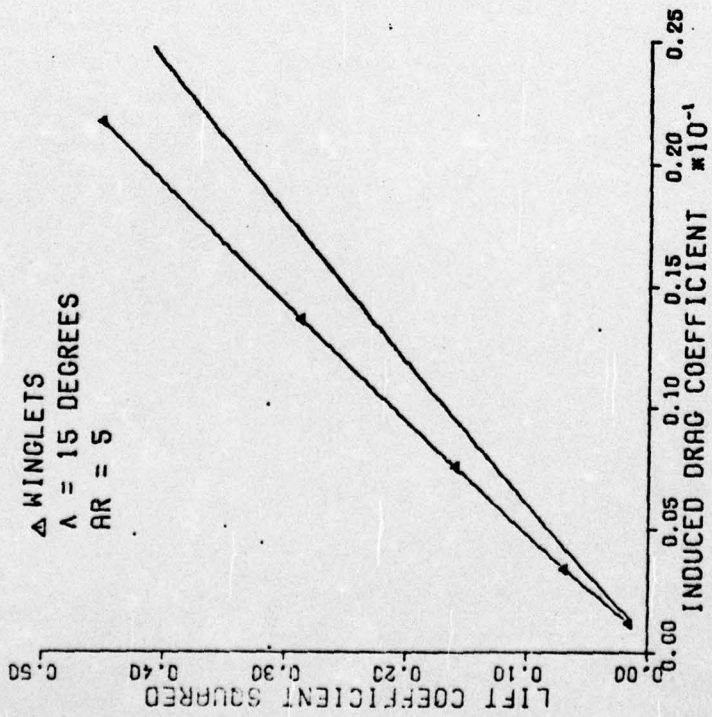


Fig. B-23.  $C_L^2$  vs  $C_{Di}$  for Wing #6

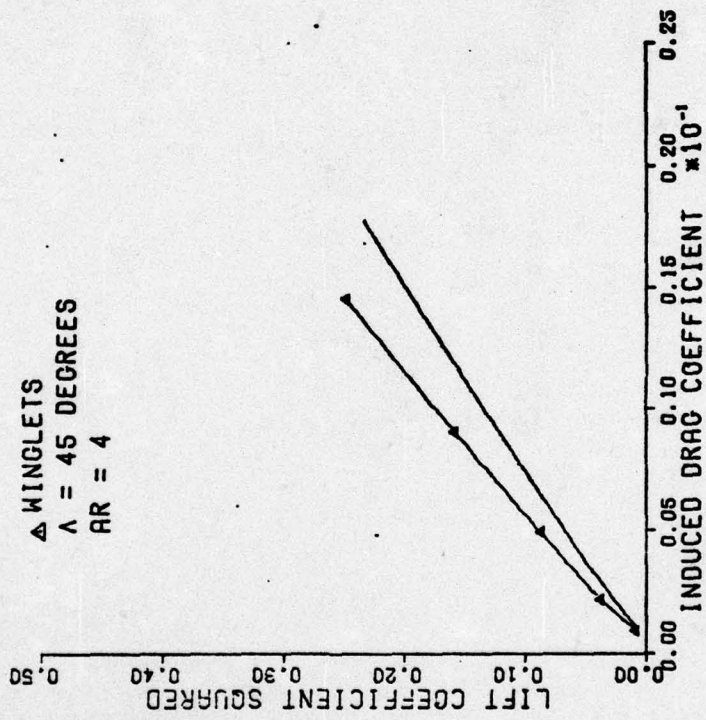


Fig. B-25.  $C_L^2$  vs  $C_{Di}$  for Wing #8

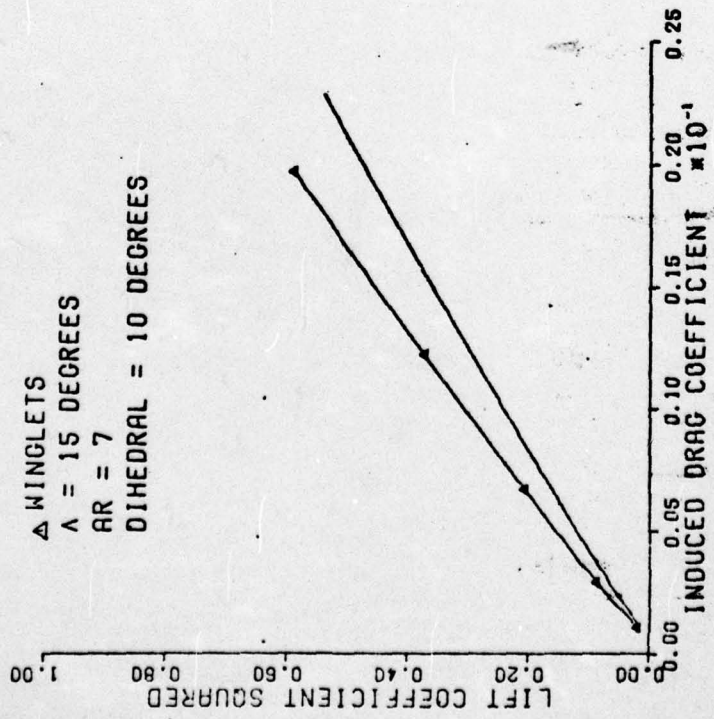


Fig. B-26.  $C_L^2$  vs  $C_{Di}$  for Wing #9

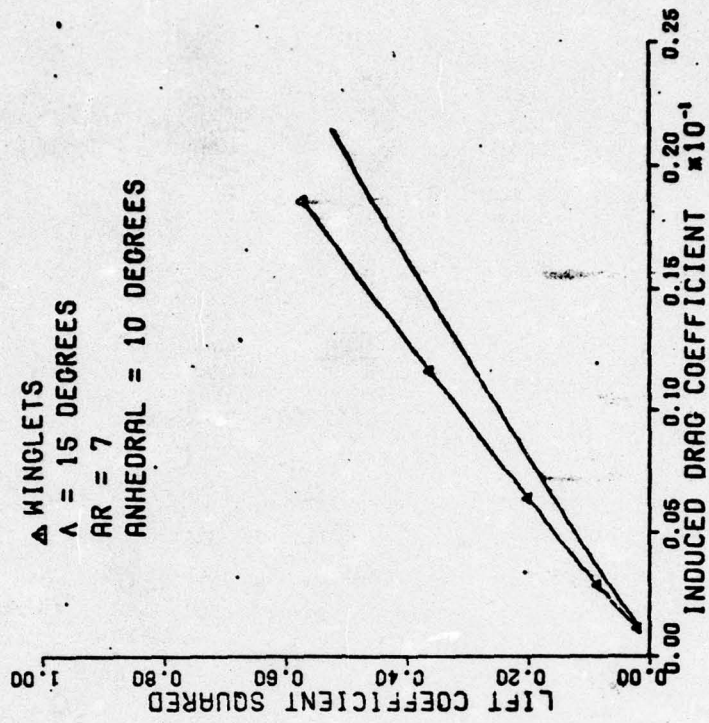


Fig. B-27.  $C_L^2$  vs  $C_{Di}$  for Wing #10

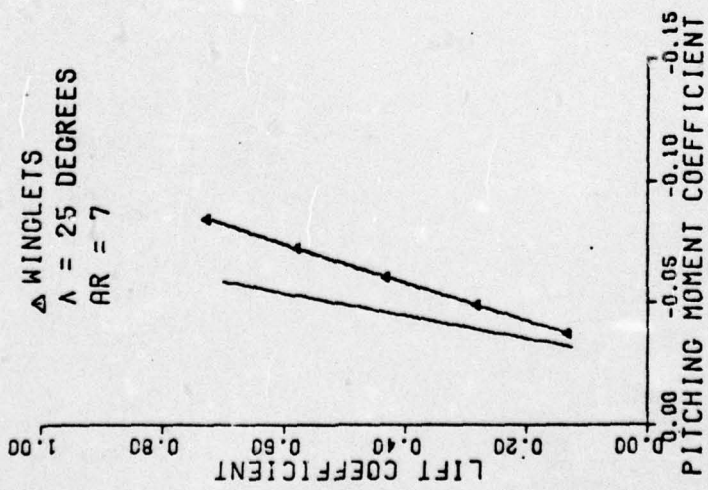


Fig. B-28. Wing #2 Pitching Moments

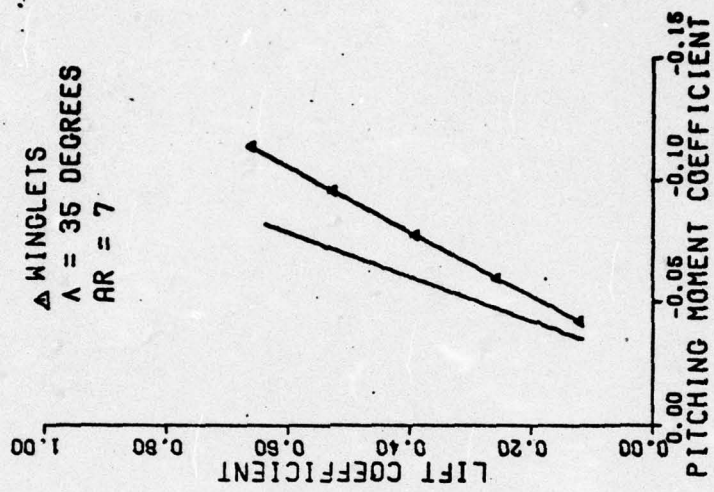


Fig. B-29. Wing #3 Pitching Moments

AD-A034 944

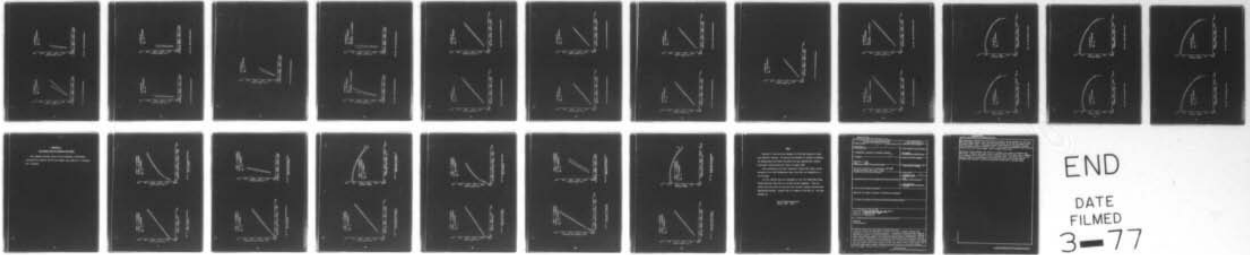
AIR FORCE INST OF TECH WRIGHT-PATTERSON AFB OHIO SCH--ETC F/6 1/3  
A PARAMETRIC ANALYSIS OF WINGLET EFFECTS.(U)

DEC 76 M D CARY  
GA/MC/76D-5

UNCLASSIFIED

NL

2 OF 2  
AD  
A034944



END  
DATE  
FILMED  
3-77

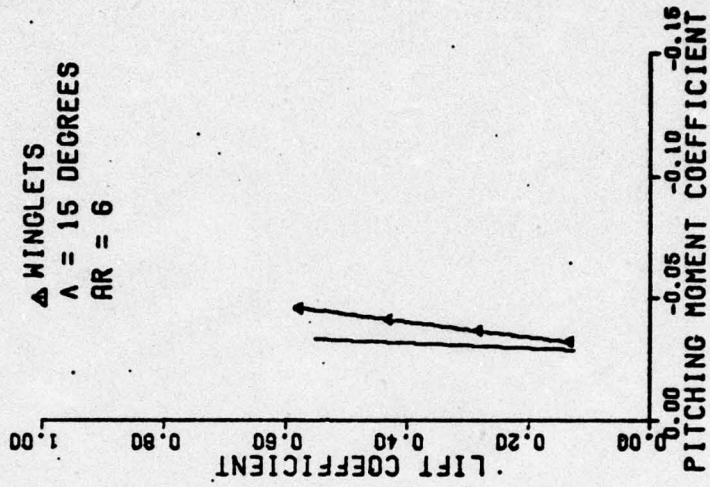


Fig. B-31. Wing #5 Pitching Moments

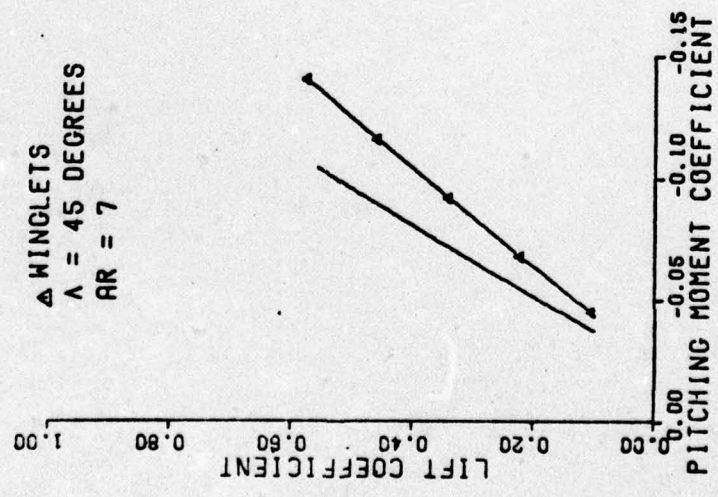


Fig. B-30. Wing #4 Pitching Moments

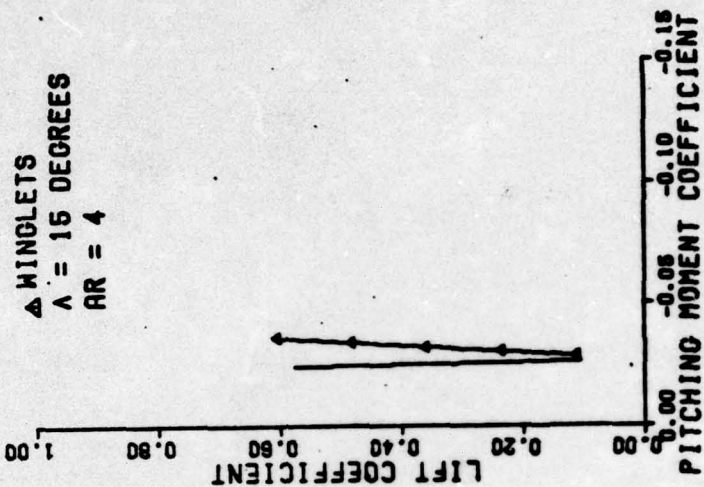


Fig. B-31. Wing #7 Pitching Moments

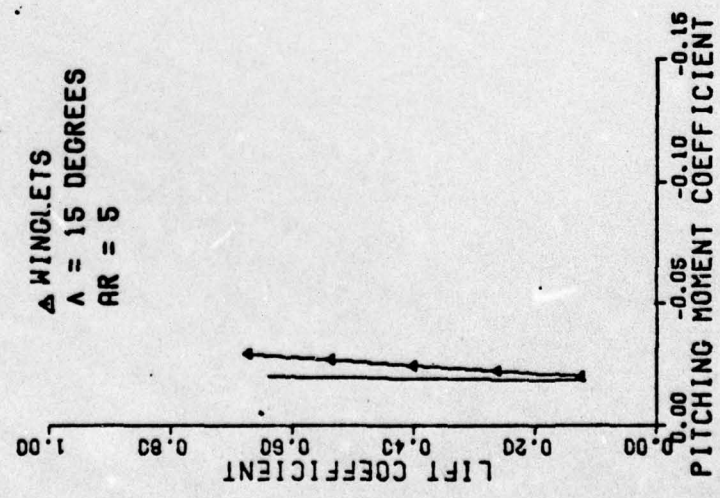


Fig. B-32. Wing #6 Pitching Moments

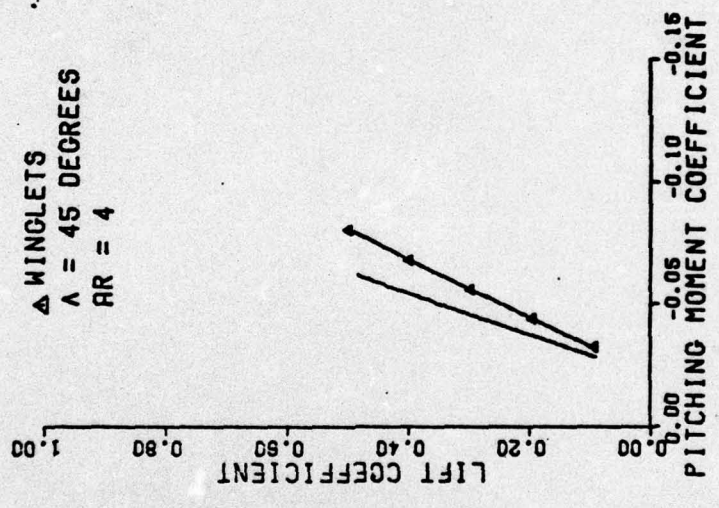


Fig. B-34. Wing 48 Pitching Moments

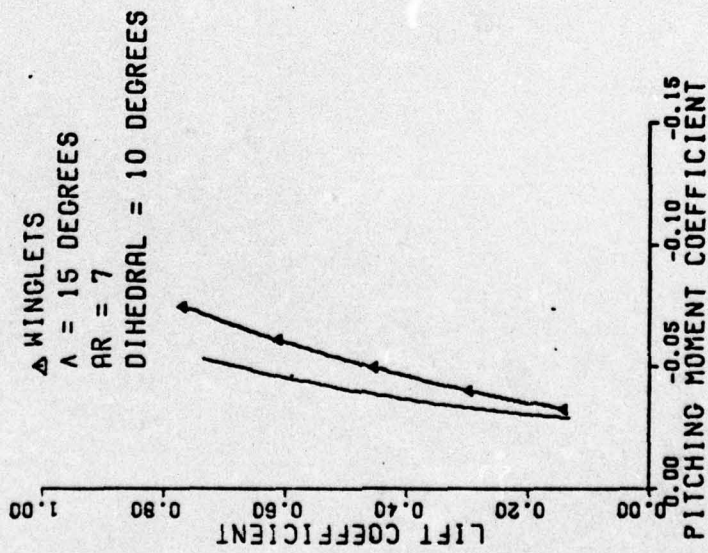


Fig. B-35. Wing #9 Pitching Moments

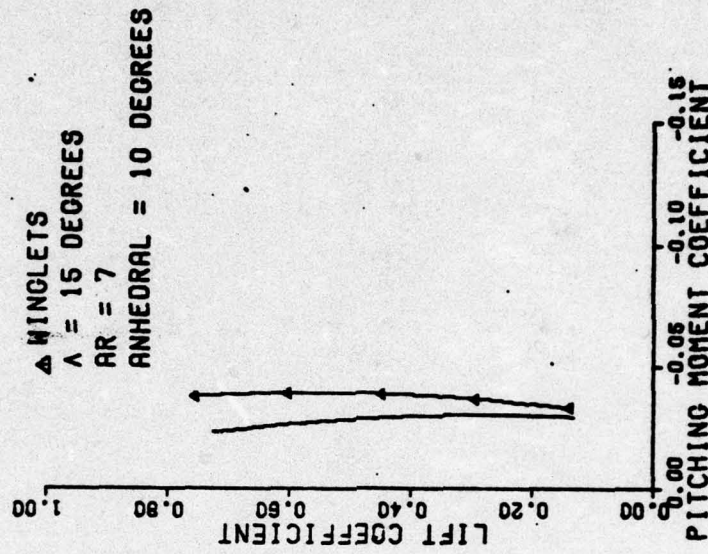


Fig. B-36. Wing #10 Pitching Moments

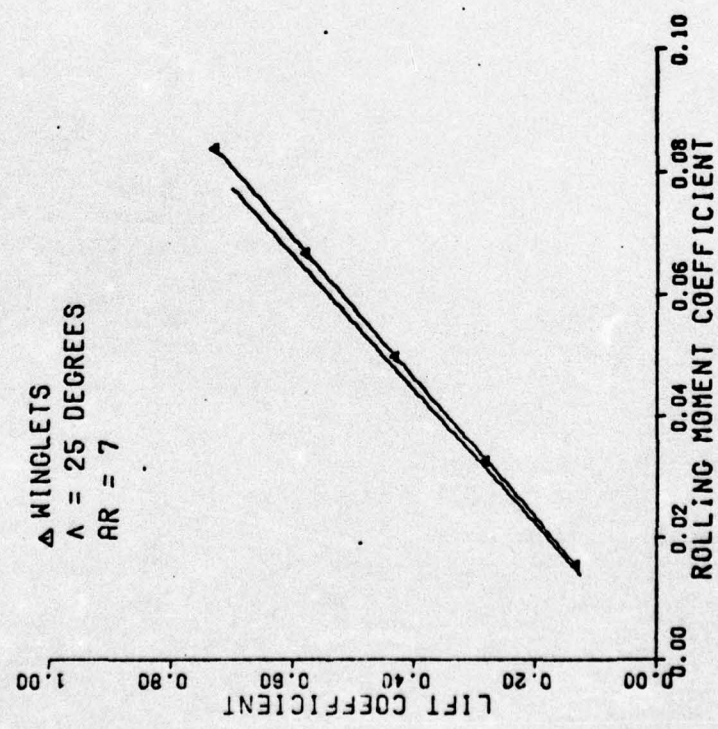


Fig. B-37. Wing #2 Root Bending Moments

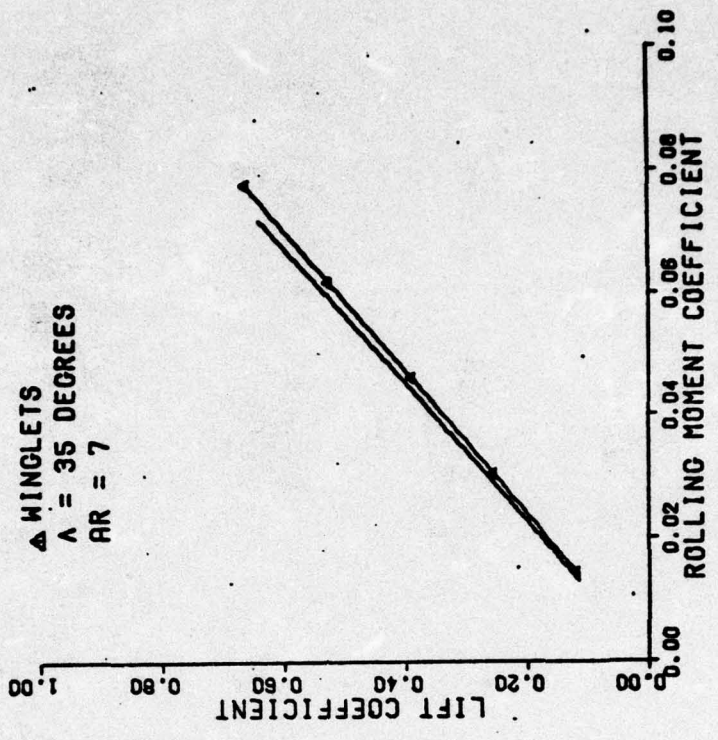


Fig. B-38. Wing #3 Root Bending Moments

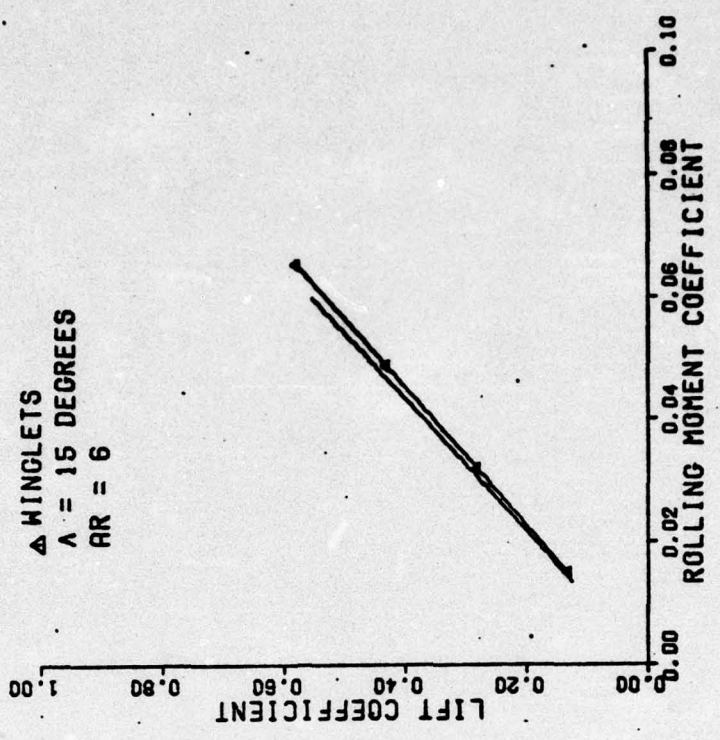


Fig. B-40. Wing #5 Root Bending Moments

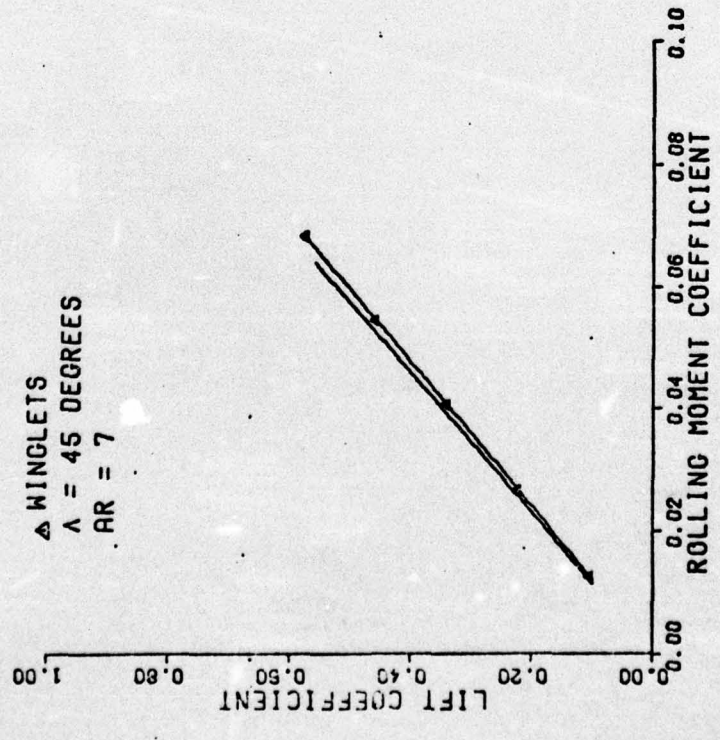


Fig. B-39. Wing #4 Root Bending Moments

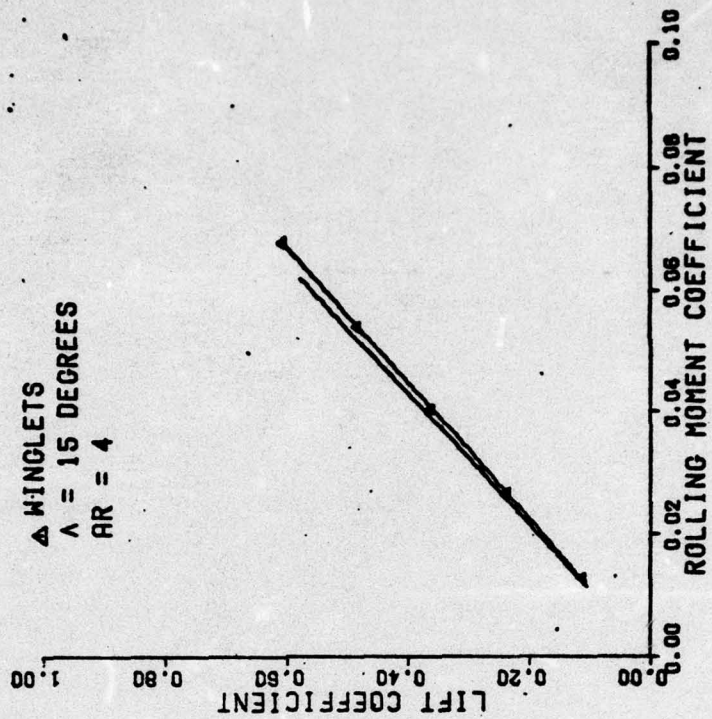


Fig. B-42. Wing #7 Root Bending Moments

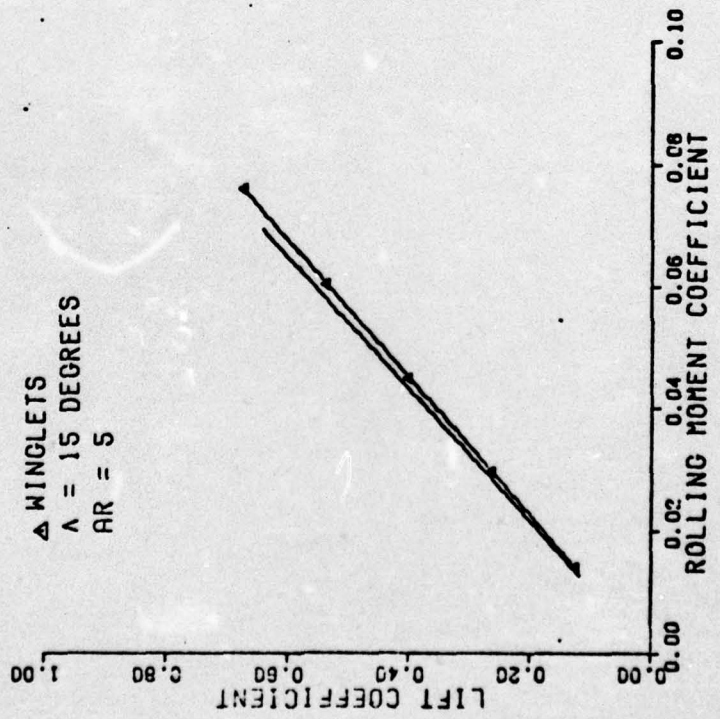


Fig. B-41. Wing #6 Root Bending Moments

▲ WINGLETS  
A = 45 DEGREES  
AR = 4

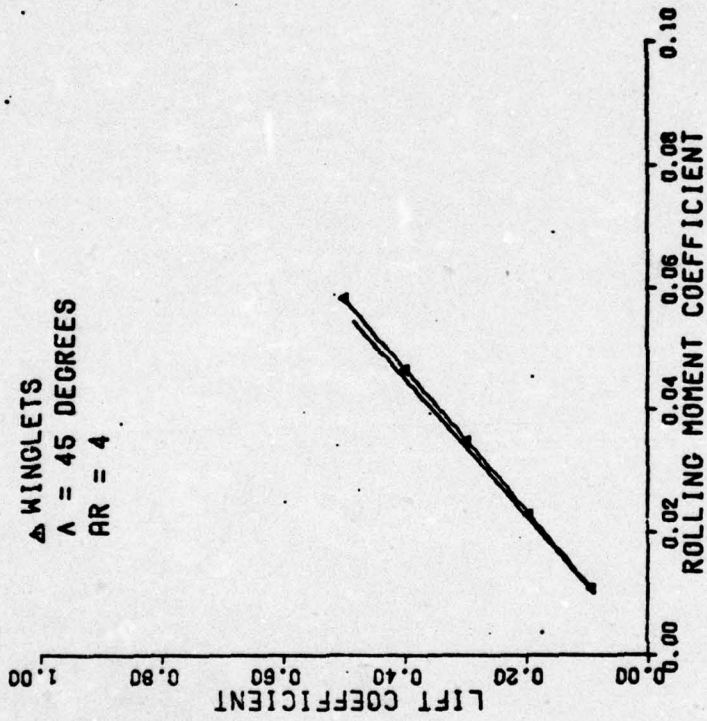


Fig. B-43. Wing #8 Root Bending Moments

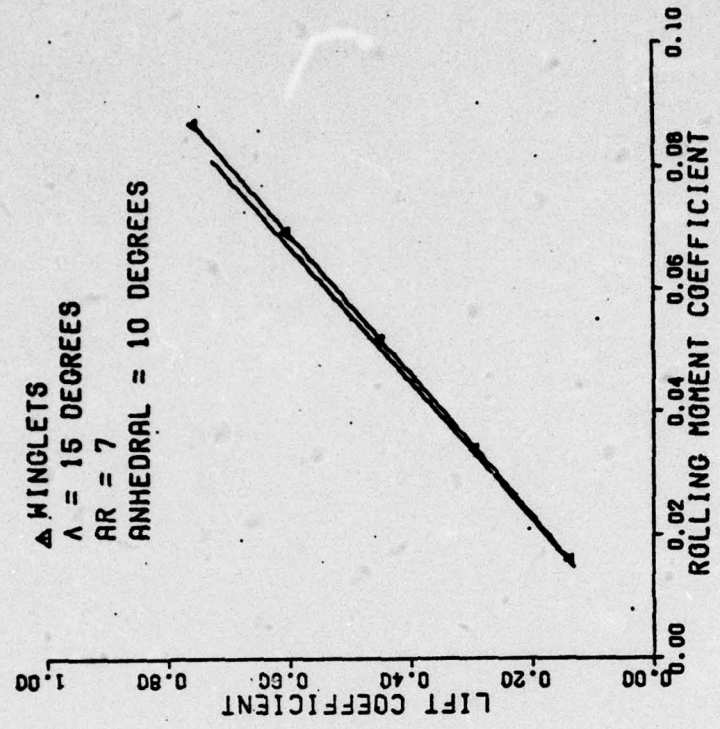


Fig. B-45. Wing #10 Root Bending Moments

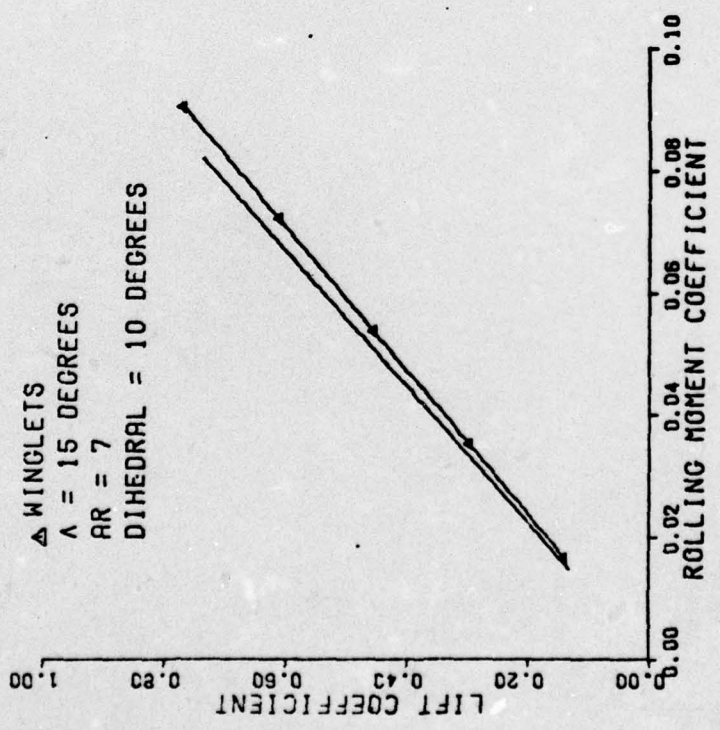


Fig. B-44. Wing #9 Root Bending Moments

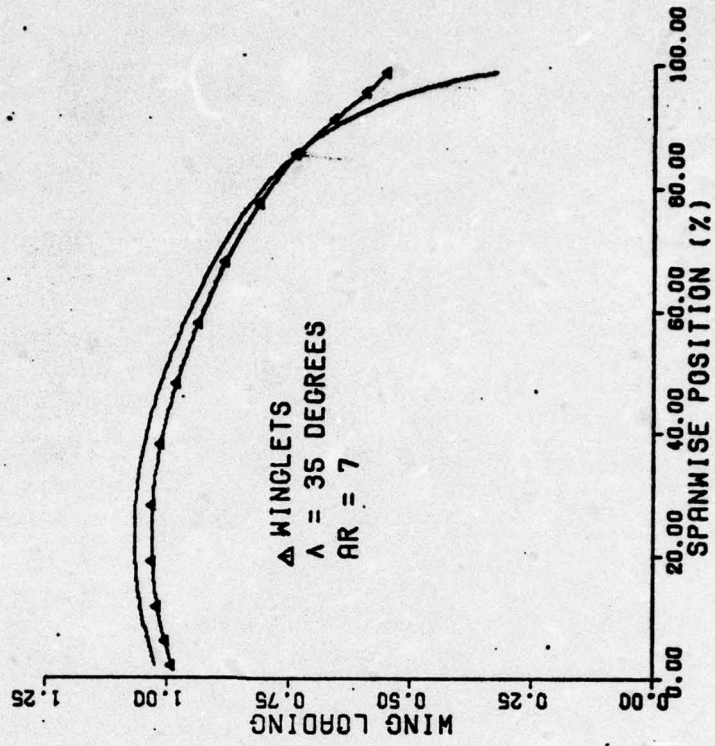


Fig. B-47: Wing #3 Spanwise Loading

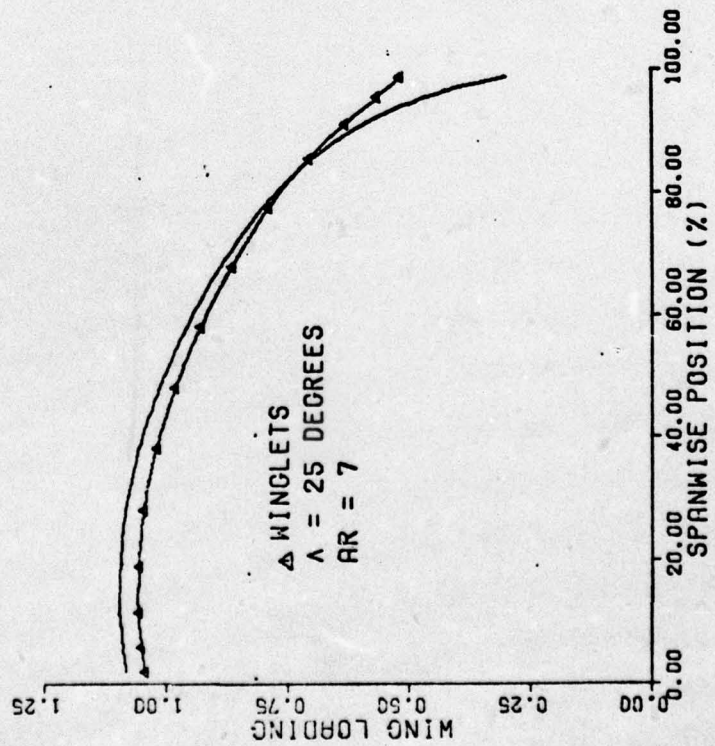


Fig. B-46: Wing #2 Spanwise Loading

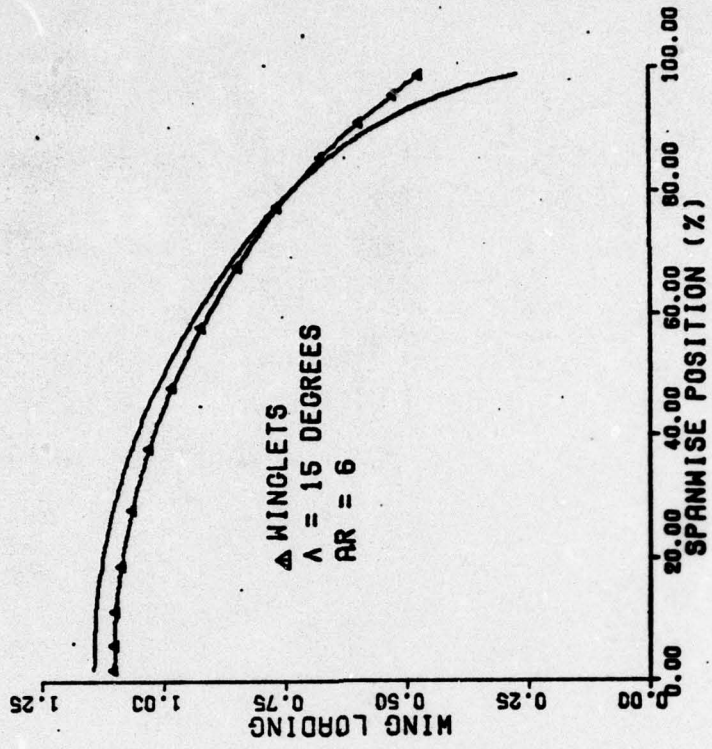


Fig. B-49. Wing #5 Spanwise Loading

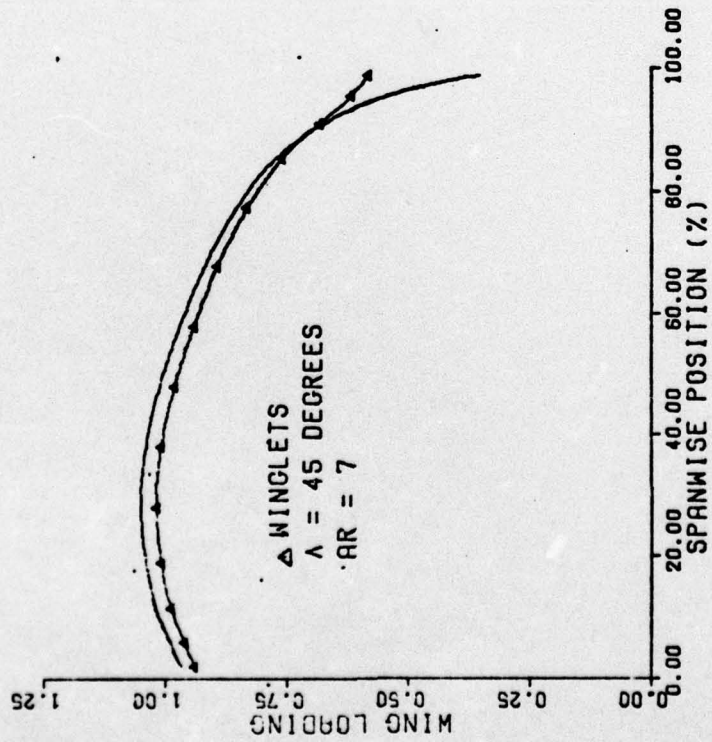


Fig. B-48. Wing #4 Spanwise Loading

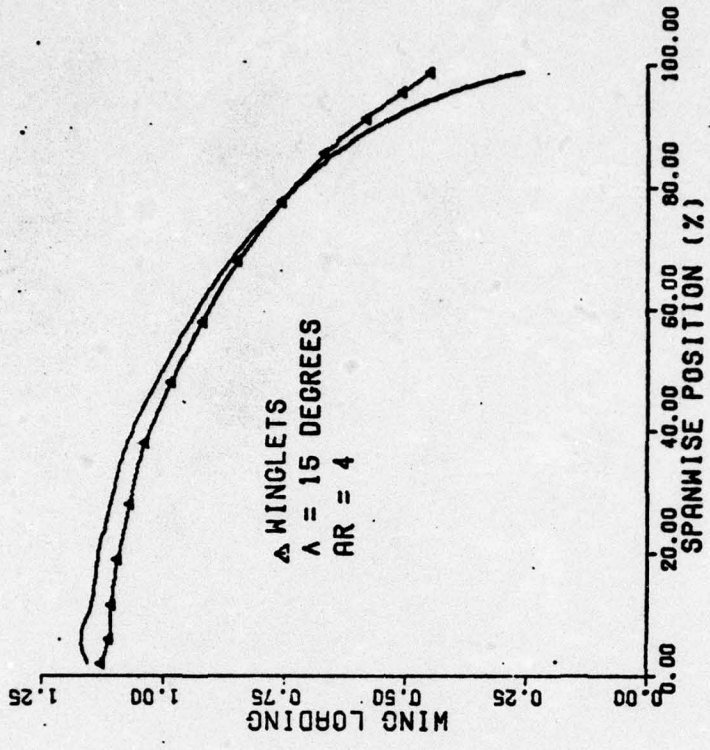


Fig. B-51. Wing #7 Spanwise Loading

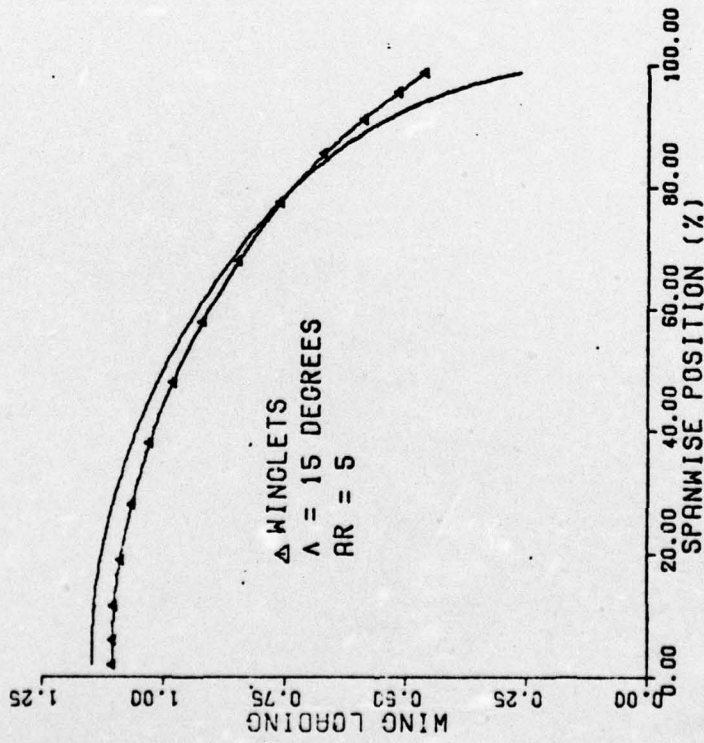


Fig. B-50. Wing #6 Spanwise Loading

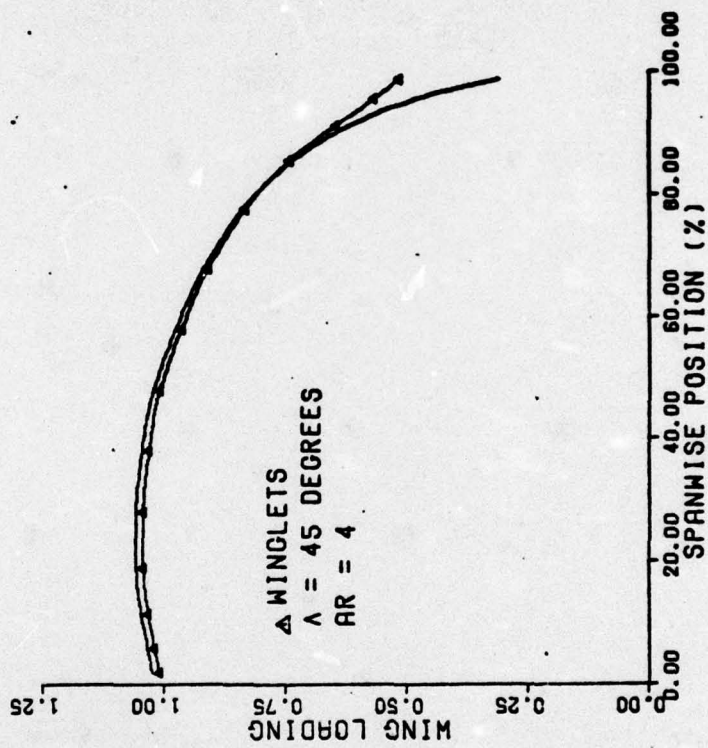


Fig. B-52. Wing #8 Spanwise Loading

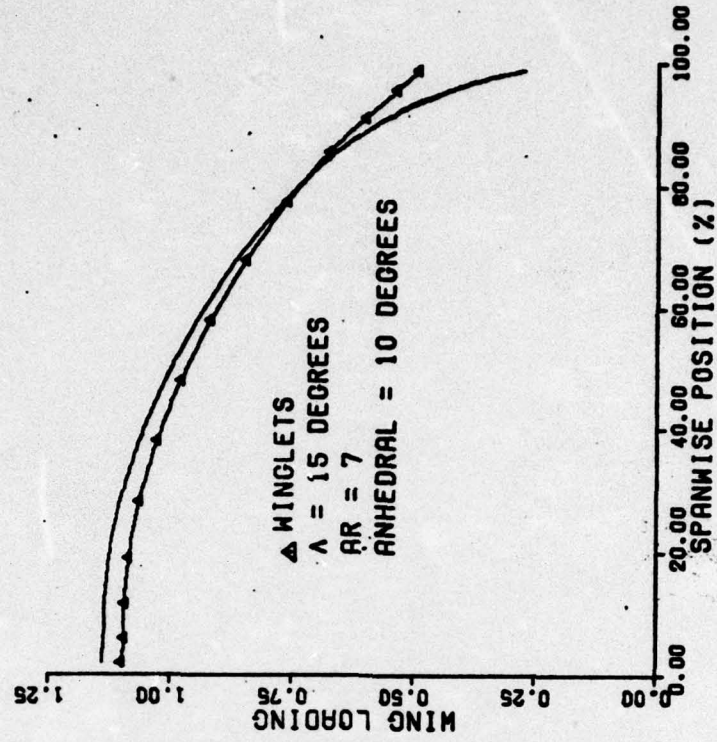


Fig. B-54. Wing #10 Spanwise Loading

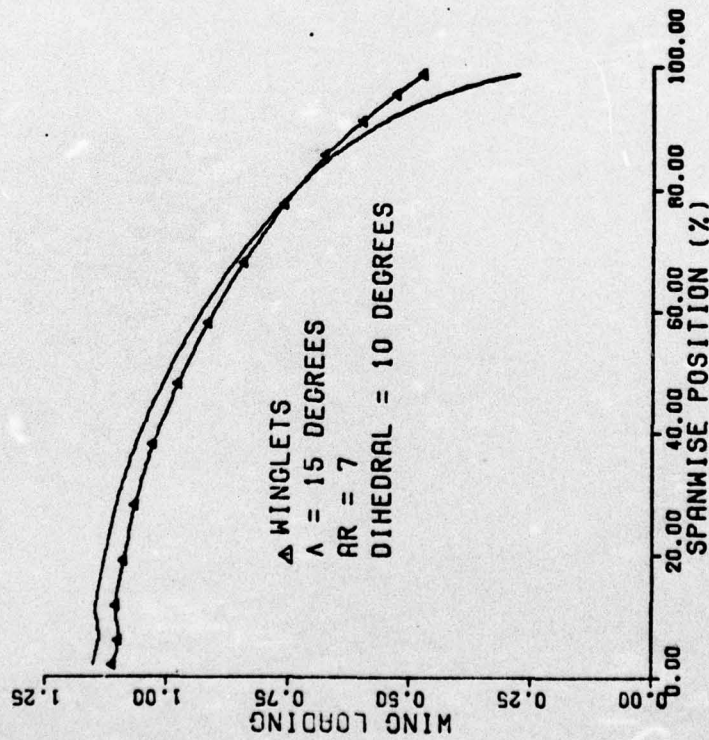


Fig. B-53. Wing #9 Spanwise Loading

Appendix C

Aerodynamic Data for Winglet Cant Angle

This Appendix contains plots of the aerodynamic coefficients calculated for wings #1 and #3 with winglet cant angles of + 3 degrees and -3 degrees.

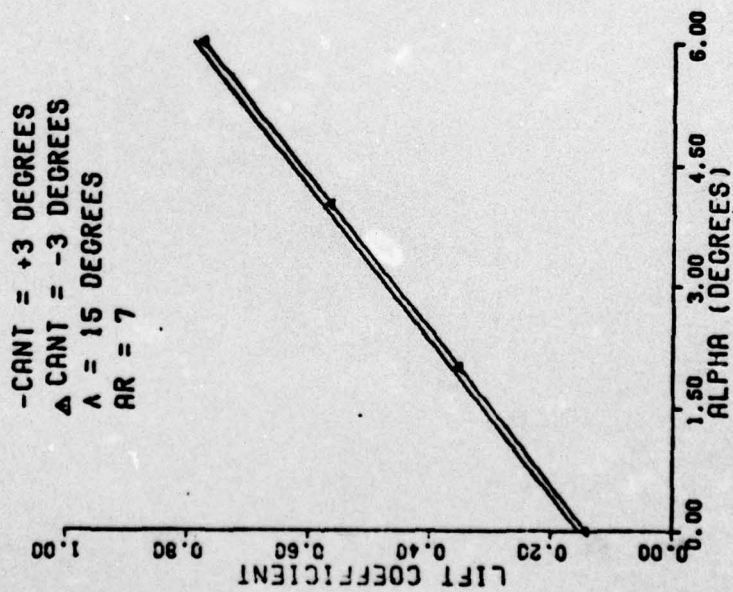


Fig. C-1. Wing #1 Lift Curve With Winglet  
Cant = 3 Degree

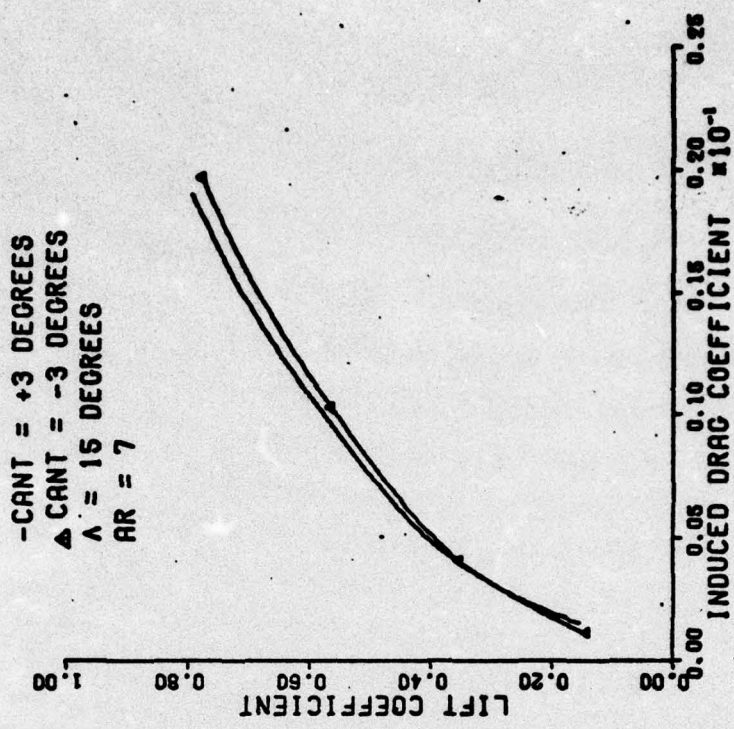


Fig. C-2. Wing #1 Drag Polars With Winglet  
Cant = 3 Degree

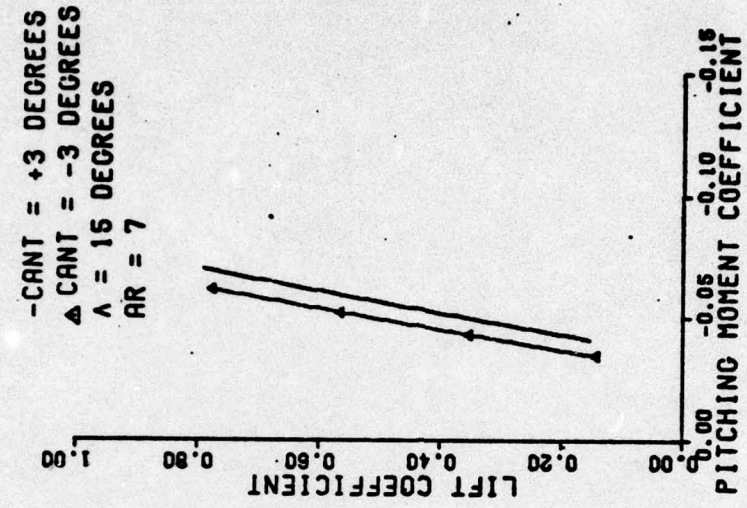


Fig. C-4. Wing #1 Pitching Moments With Winglet Cant = ± 3 Degree

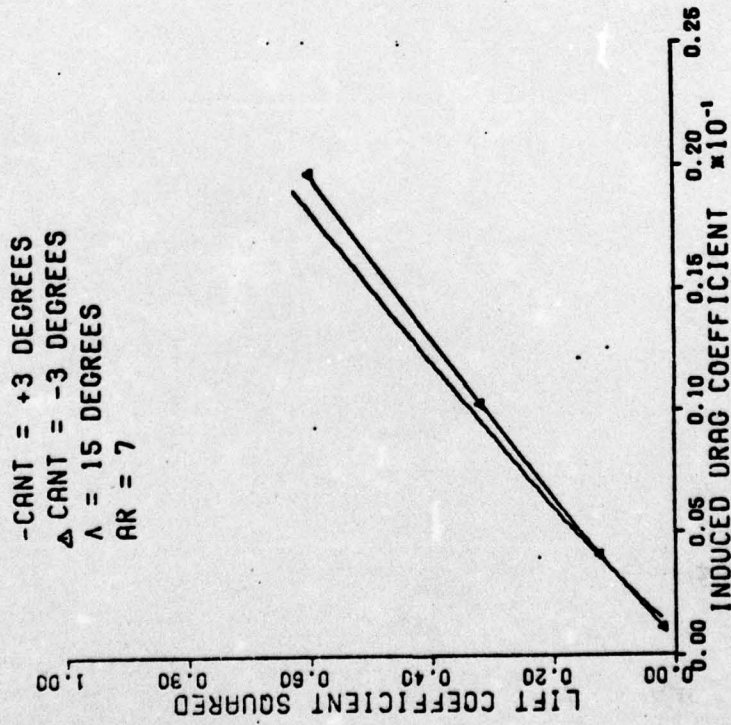


Fig. C-3.  $C_L^2$  vs  $C_{Di}$  for Wing #1 With Winglet Cant = ± 3 Degree

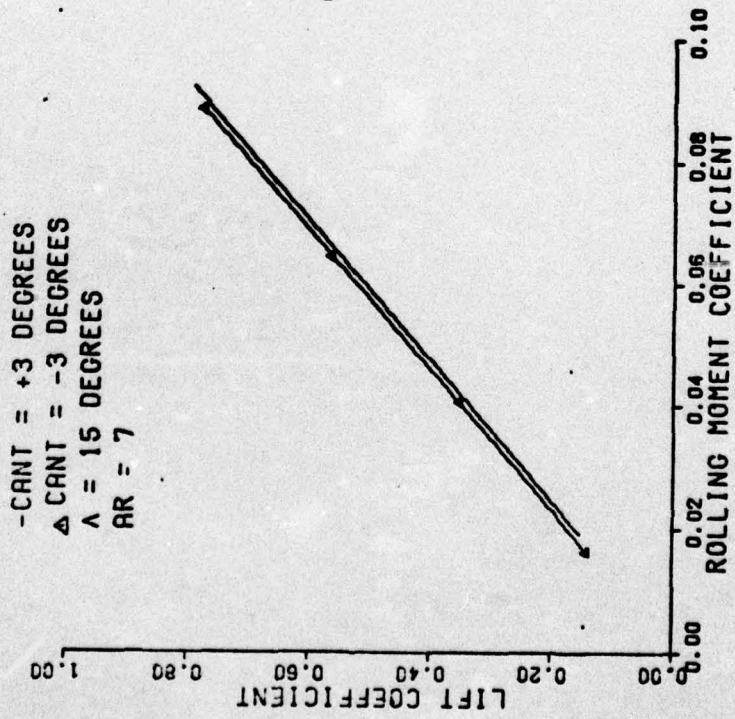


Fig. C-5. Wing #1 Root Bending Moments With Winglet Cant = ± 3 Degrees

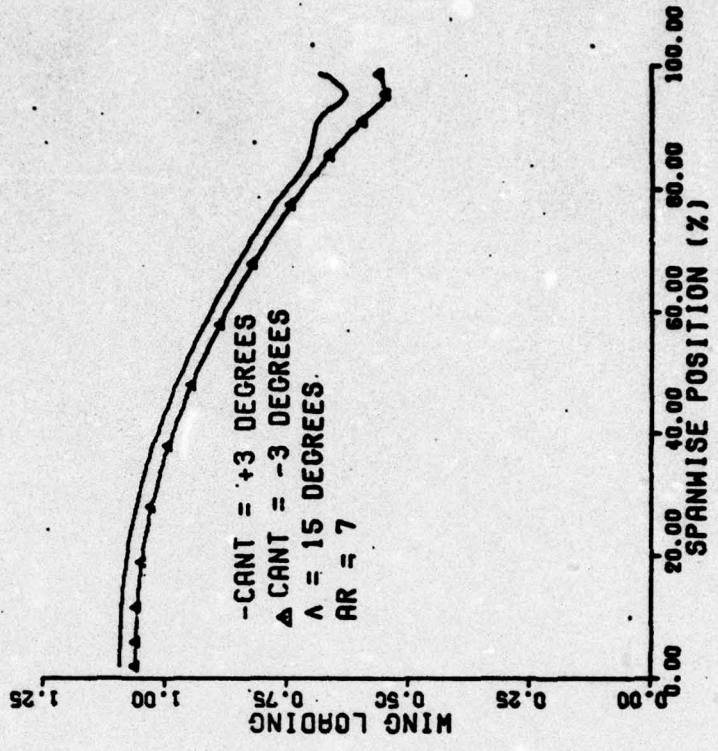


Fig. C-6. Wing #1 Spanwise Loading With Winglet Cant = ± 3 Degrees

-CANT = +3 DEGREES  
 ▲ CANT = -3 DEGREES  
 Λ = 35 DEGREES  
 AR = 7

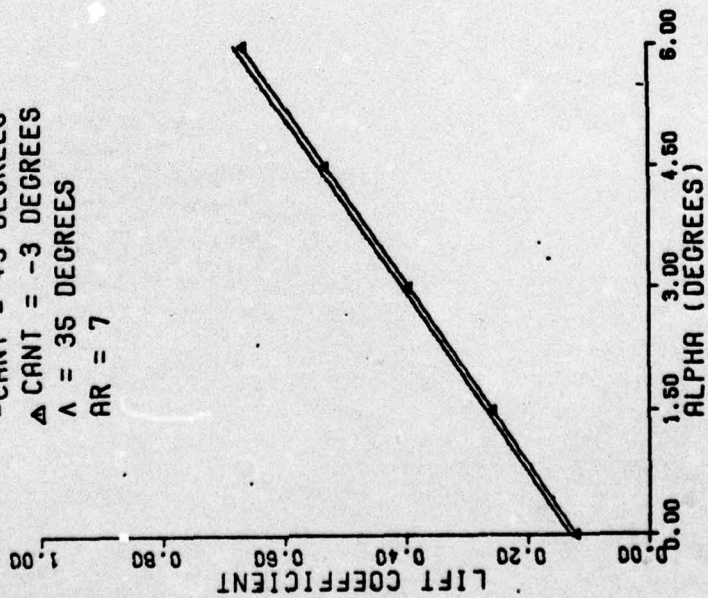


Fig. C-7. Wing #3 Lift Curves With Winglet Cant = ± 3 Degrees

-CANT = +3 DEGREES  
 ▲ CANT = -3 DEGREES  
 Λ = 35 DEGREES  
 AR = 7

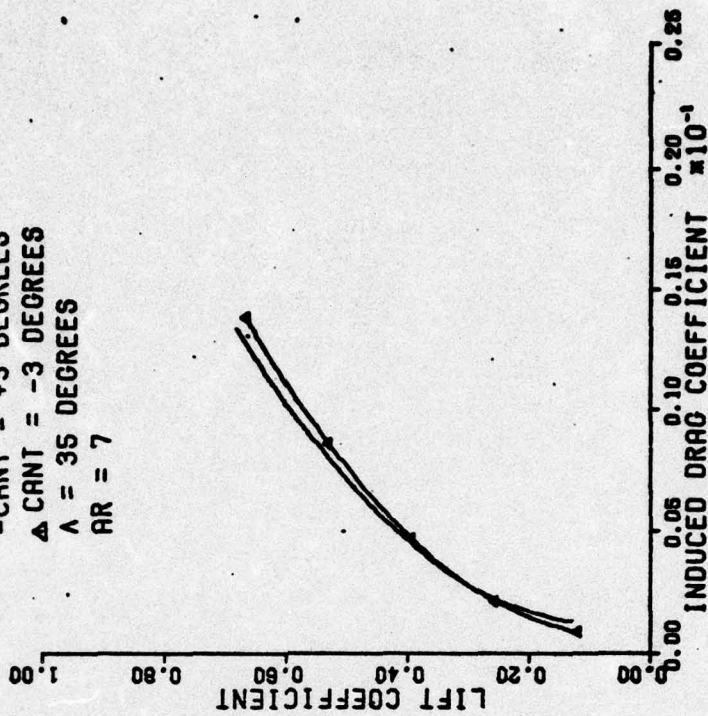
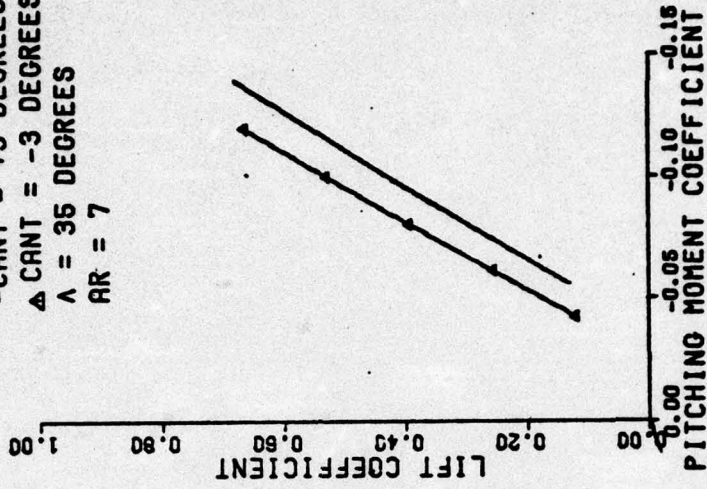


Fig. C-8. Wing #3 Drag Polars With Winglet Cant = ± 3 Degrees

-CANT = +3 DEGREES  
 ▲ CANT = -3 DEGREES  
 A = 35 DEGREES  
 AR = 7



-CANT = +3 DEGREES  
 ▲ CANT = -3 DEGREES  
 A = 35 DEGREES  
 AR = 7

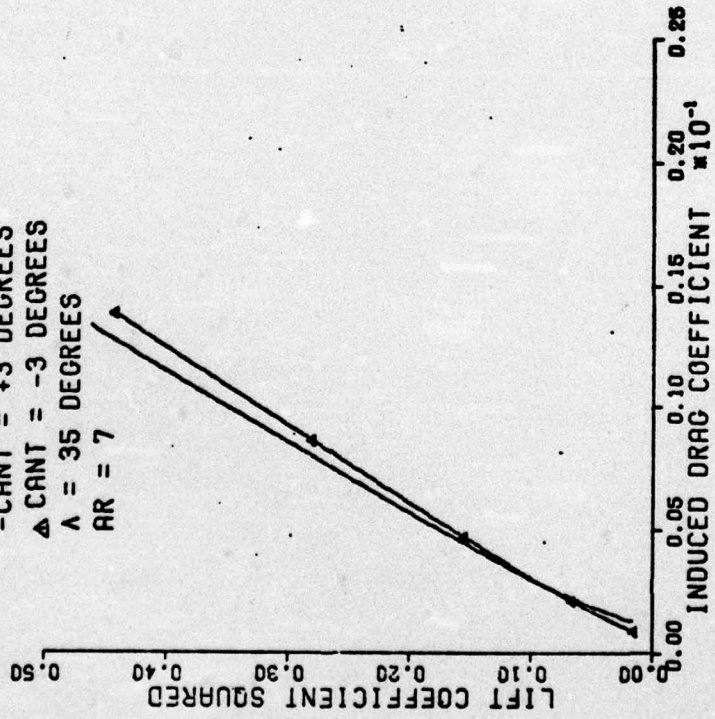


Fig. C-10. Wing #3 Pitching Moments With Winglet Cant =  $\pm 3$  Degrees

Fig. C-9.  $C_L^2$  vs  $C_{Di}$  for Wing #3 With Winglet Cant =  $\pm 3$  Degrees

-CANT = +3 DEGREES  
 Δ CANT = -3 DEGREES  
 Λ = 35 DEGREES  
 AR = 7

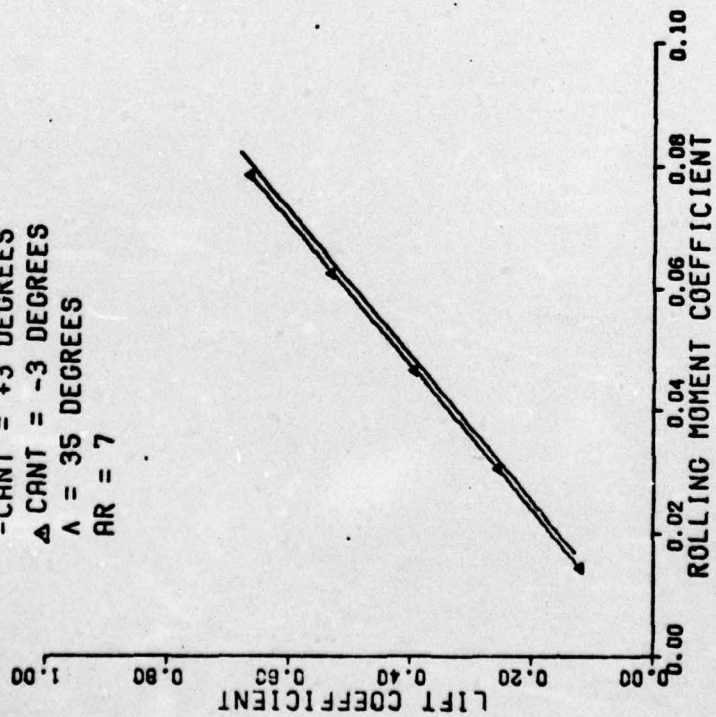


Fig. C-11. Wing #3 Root Bending Moments  
 With Winglet Cant = ± 3 Degrees

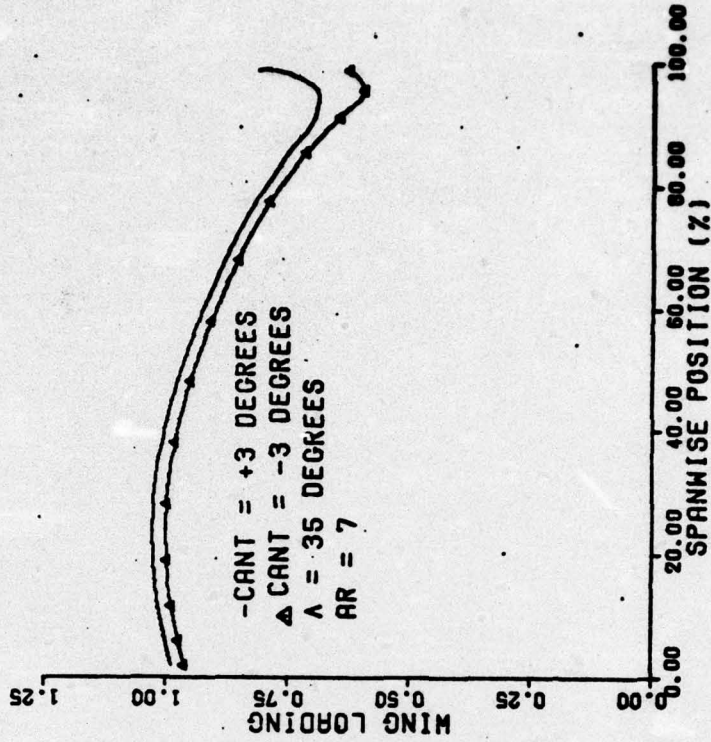


Fig. C-12. Wing #3 Spanwise Loading With  
 Winglet Cant = ± 3 Degrees

Vita

Mitchell D. Cary was born December 23, 1946 and raised on a farm near Hamilton, Indiana. He received his Bachelor of Science in Mechanical Engineering from Purdue University and was commissioned a Second Lieutenant, United States Air Force, in August 1968.

After graduation from pilot training at Laredo AFB, Texas, he was assigned to the 509th Bombardment Wing, Pease AFB, New Hampshire as a KC-135 pilot.

In 1973, Captain Cary was reassigned to the 17th Bombardment Wing, Wright-Patterson AFB, Ohio as a B-52H aircraft commander. There he served until his entry in June 1975 into the AFIT Graduate Astronautical Engineering program. Captain Cary is a member of Tau Beta Pi. His home address is:

3113 Village Green Drive  
Dayton, Ohio 45432

UNCLASSIFIED

SECURITY CLASSIFICATION OF THIS PAGE (When Data Entered)

REPORT DOCUMENTATION PAGE		READ INSTRUCTIONS BEFORE COMPLETING FORM
1. REPORT NUMBER <b>GA/MC/76D-5</b>	2. GOVT ACCESSION NO.	3. RECIPIENT'S CATALOG NUMBER
4. TITLE (and Subtitle) <b>A PARAMETRIC ANALYSIS OF WINGLET EFFECTS</b>		5. TYPE OF REPORT & PERIOD COVERED <b>MS Thesis</b>
7. AUTHOR(s) <b>Mitchell D. Cary Capt USAF</b>		6. PERFORMING ORG. REPORT NUMBER
9. PERFORMING ORGANIZATION NAME AND ADDRESS <b>Air Force Institute of Technology (AFIT-EN) Wright-Patterson AFB, Ohio 45433</b>		8. CONTRACT OR GRANT NUMBER(s)
11. CONTROLLING OFFICE NAME AND ADDRESS		10. PROGRAM ELEMENT, PROJECT, TASK AREA & WORK UNIT NUMBERS
14. MONITORING AGENCY NAME & ADDRESS (if different from Controlling Office)		12. REPORT DATE <b>December 1976</b>
		13. NUMBER OF PAGES <b>102</b>
		15. SECURITY CLASS. (of this report) <b>Unclassified</b>
		15a. DECLASSIFICATION/DOWNGRADING SCHEDULE
16. DISTRIBUTION STATEMENT (of this Report) <b>Approved for public release; distribution unlimited.</b>		
17. DISTRIBUTION STATEMENT (of the abstract entered in Block 20, if different from Report)		
18. SUPPLEMENTARY NOTES <b>Approved for public release; IAW AFR 190-17 Jerral F. Guess, Captain, USAF Director of Information</b>		
19. KEY WORDS (Continue on reverse side if necessary and identify by block number) <b>Winglets Drag Reduction</b>		
20. ABSTRACT (Continue on reverse side if necessary and identify by block number) <b>A two part study was undertaken. In the first part, winglet effects were examined on a variety of wing planforms. A nonplanar lifting surface computer program was used to calculate aerodynamic coefficients including lift, induced drag, wing pitching moment, and wing root bending moment coefficients. Typical cruise flight conditions were examined and the coefficients calculated for the wing alone were compared to those obtained for the wing with winglets installed. The calculations were then repeated as the wing aspect ratio, sweep angle, and dihedral angle were varied. Winglet size and orientation remained constant.</b>		

**UNCLASSIFIED**

SECURITY CLASSIFICATION OF THIS PAGE(When Data Entered)

The percentage induced drag reduction was found to be the greatest on the wing with the highest aspect ratio and wing sweep angle (27.5% for an aspect ratio 7, 45 degree swept wing). Percentage induced drag reduction increased slightly with increasing positive dihedral angle. The greatest incremental drag reduction occurred with the lowest aspect ratio, highest swept wing.

The second study examined the effects of winglet cant angle on induced drag reduction. Winglet cant angle on two separate wings was varied from -3 degrees to +3 degrees in an attempt to find an optimum value. The model used in this analysis ignored viscous effects and indicated that positive cant angles (leading edge inboard) yielded the greatest reductions in induced drag.

SECURITY CLASSIFICATION OF THIS PAGE(When Data Entered)